

## **CryoEM structures of the human CLC-2 voltage gated chloride channel reveal a ball and chain gating mechanism**

Mengyuan Xu<sup>1</sup>, Torben Neelands<sup>1</sup>, Alexander S. Powers<sup>2,3,4,5</sup>, Yan Liu<sup>6</sup>, Steven D. Miller<sup>2</sup>, Grigore Pintilie<sup>7</sup>, J. Du Bois<sup>2</sup>, Ron O. Dror<sup>1,3,4,5</sup>, Wah Chiu<sup>6,7</sup>, Merritt Maduke<sup>1</sup>

<sup>1</sup>Department of Molecular and Cellular Physiology, Stanford University, Stanford, CA 94305

<sup>2</sup>Department of Chemistry, Stanford University, Stanford, CA 94305

<sup>3</sup>Department of Computer Science, Stanford University, Stanford, CA 94305

<sup>4</sup>Department of Structural Biology, Stanford University, Stanford, CA 94305

<sup>5</sup>Institute for Computational and Mathematical Engineering, Stanford University, Stanford, CA 94305

<sup>6</sup>Division of CryoEM and Bioimaging, SSRL, SLAC National Accelerator Laboratory, Stanford University, Menlo Park 94025

<sup>7</sup>Department of Bioengineering and Department of Microbiology and Immunology, Stanford University, Stanford, 94305

### **Correspondence:**

Dr. Merritt Maduke

279 Campus Drive West

Stanford, CA 94035

Tel: 650-723-9075

Email: [maduke@stanford.edu](mailto:maduke@stanford.edu)

**Keywords:** chloride channel, cryo-electron microscopy, electrophysiology

## ABSTRACT:

CLC-2 is a voltage-gated chloride channel that contributes to electrical excitability and ion homeostasis in many different mammalian tissues and cell types. Among the nine mammalian CLC homologs, CLC-2 is uniquely activated by hyperpolarization, rather than depolarization, of the plasma membrane. The molecular basis for the divergence in polarity of voltage gating mechanisms among closely related CLC homologs has been a long-standing mystery, in part because few CLC channel structures are available, and those that exist exhibit high conformational similarity. Here, we report cryoEM structures of human CLC-2 at 2.46 – 2.76 Å, in the presence and absence of the potent and selective inhibitor AK-42. AK-42 binds within the extracellular entryway of the Cl<sup>-</sup>-permeation pathway, occupying a pocket previously proposed through computational docking studies. In the apo structure, we observed two distinct apo conformations of CLC-2 involving rotation of one of the cytoplasmic C-terminal domains (CTDs). In the absence of CTD rotation, an intracellular N-terminal 15-residue hairpin peptide nestles against the TM domain to physically occlude the Cl<sup>-</sup>-permeation pathway from the intracellular side. This peptide is highly conserved among species variants of CLC-2 but is not present in any other CLC homologs. Previous studies suggested that the N-terminal domain of CLC-2 influences channel properties via a “ball-and-chain” gating mechanism, but conflicting data cast doubt on such a mechanism, and thus the structure of the N-terminal domain and its interaction with the channel has been uncertain. Through electrophysiological studies of an N-terminal deletion mutant lacking the 15-residue hairpin peptide, we show that loss of this short sequence increases the magnitude and decreases the rectification of CLC-2 currents expressed in mammalian cells. Furthermore, we show that with repetitive hyperpolarization WT CLC-2 currents increase in resemblance to the hairpin-deleted CLC-2 currents. These functional results combined with our structural data support a model in which the N-terminal hairpin of CLC-2 stabilizes a closed state of the channel by blocking the cytoplasmic Cl<sup>-</sup>-permeation pathway.

## 1 INTRODUCTION

2 Ion transport across the cell membrane establishes and exploits ion gradients to store energy and  
3 regulate electrical signaling. Ion transport is catalyzed by two classes of membrane proteins: ion channels  
4 and active transporters. The CLC “Chloride Channel” family encompasses both major ion-transport  
5 mechanisms: half of the CLC homologs are electrodiffusive chloride ( $\text{Cl}^-$ ) channels, and half are  
6 secondary active transporters that stoichiometrically exchange  $\text{Cl}^-$  for protons ( $\text{H}^+$ ) (Jentsch and Pusch,  
7 2018). The occurrence of two mechanisms in one family suggests they operate by variations on a  
8 common theme (Miller, 2006), and experimental results revealed that CLC channels are “broken”  
9 transporters (Lisal and Maduke, 2008).

10 In both CLC channels and transporters, a conserved glutamate residue referred to as the “gating  
11 glutamate” ( $E_{\text{gate}}$ ) plays a central mechanistic role. High resolution CLC transporter structures show that  
12 this residue can adopt four different conformations (Dutzler et al., 2002; Dutzler et al., 2003; Feng et al.,  
13 2010; Chavan et al., 2020; Schrecker et al., 2020) (**Figure 1A**), which contribute to the  $\text{Cl}^-/\text{H}^+$  exchange  
14 mechanism (Accardi and Miller, 2004; Feng et al., 2012; Chavan et al., 2020; Leisle et al., 2020). Due to  
15 the small number of CLC channel structures relative to transporters, characterization of the central role  
16 for the  $E_{\text{gate}}$  residue in CLC channels has primarily relied on extensive functional studies of channel gating  
17 rather than observed  $E_{\text{gate}}$  side chain conformations (Jentsch and Pusch, 2018). The first CLC channel  
18 structure reported was of bovine CLC-K (Park et al., 2017), a kidney-expressed homolog that is the lone  
19 CLC homolog lacking the  $E_{\text{gate}}$  (Kieferle et al., 1994). The only other CLC channel structures reported  
20 prior to 2023 are of the human CLC-1: one of these cryoEM structures shows  $E_{\text{gate}}$  in the “out” position  
21 (Park and MacKinnon, 2018) while the other lacked density for  $E_{\text{gate}}$  (Wang et al., 2019). The  $E_{\text{gate}}$  “out”  
22 position was originally posited to be exclusive to the CLC channel homologs, as its positioning off to the  
23 side widens the  $\text{Cl}^-$ -permeation pathway and, in CLC-1, results in a continuous pathway (Park and  
24 MacKinnon, 2018). Such a continuous pathway precludes exchange coupling (Jardetzky, 1966; Miller,  
25 2021). The open  $\text{Cl}^-$ -permeation pathway in the CLC-1 structure is consistent with the known functional  
26 properties of CLC-1 in the absence of an applied transmembrane voltage. CLC-1 is a voltage-gated

27 channel that is predominantly in the open state at zero mV (Altamura et al., 2020) (**Figure 1B**). At  
28 negative transmembrane voltages that favor CLC-1 closing, the  $E_{\text{gate}}$  sidechain presumably moves to  
29 either the “middle” or “down” positions, or both, to occlude the channel pore.

30 CLC-2, like CLC-1, is a voltage-gated channel, but with opposite voltage dependence, opening  
31 instead of closing in response to hyperpolarization (Thiemann et al., 1992; Wang et al., 2017). CLC-2  
32 chloride channels are expressed in every mammalian organ, where they play diverse physiological  
33 functions (Thiemann et al., 1992; Lein et al., 2007; Duan, 2013; Stolting et al., 2014b; Jentsch and Pusch,  
34 2018). Perturbation of CLC-2 function is associated with human disease including leukodystrophies  
35 (Jentsch and Pusch, 2018), blindness (Xu et al., 2023), primary aldosteronism (Fernandes-Rosa et al.,  
36 2018; Scholl et al., 2018), and atrial fibrillation (Hansen et al., 2020). Despite their importance in human  
37 physiology, our understanding of CLC-2 molecular and physiological mechanisms is incomplete. A  
38 mystery concerning CLC-2 is why electrophysiological recordings of natively expressed channels reveal  
39 tremendous variation in voltage-dependent gating. CLC-2 currents are typically inwardly rectifying and  
40 activated by hyperpolarization, but the kinetics and degree of rectification are highly variable (Bosl et al.,  
41 2001; Jentsch and Pusch, 2018). In some cases, this variability is understood – for example interactions  
42 between CLC-2 and the astrocytic GlialCAM protein yields voltage-independent currents (Jeworutzki et  
43 al., 2012; Maduke and Reimer, 2012). Yet many questions about CLC-2 gating remain.

44 Like CLC-1, CLC-2 gating depends critically on  $E_{\text{gate}}$  (Niemeyer et al., 2003; Cederholm et al.,  
45 2010). At zero mV, CLC-2 is predominantly in the closed state (Stolting et al., 2013; Stolting et al., 2014b;  
46 Jentsch and Pusch, 2018), presumably with  $E_{\text{gate}}$  blocking the pore. Such pore localization for  $E_{\text{gate}}$  was  
47 modeled in a recent CLC-2 cryoEM structure (Ma et al., 2023); however, experimental density for the  
48 sidechain was lacking, and therefore the precise structure of this gate remains uncertain (**Figure 1B**).  
49 Structures with improved resolution will be crucial to understanding CLC-2 gating, which involves  
50 interactions between  $E_{\text{gate}}$ ,  $\text{Cl}^-$  and  $\text{H}^+$ , with differential effects of external vs internal ions (Pusch et al.,  
51 1999; Niemeyer et al., 2003; Sanchez-Rodriguez et al., 2010; Sanchez-Rodriguez et al., 2012; De Jesus-  
52 Perez et al., 2016). In addition to the  $E_{\text{gate}}$  mechanism, a “ball-and-chain” gating mechanism, in which the

53 tethered N-terminus blocks the pore, has been proposed for CLC-2 (Grunder et al., 1992). However, this  
54 idea has been controversial (Varela et al., 2002) and the mechanism by which mutations in the N-terminal  
55 domain influence gating remains unknown. Because a structural foundation for understanding CLC-2  
56 gating has been lacking, we determined cryoEM structures of CLC-2, in the presence and absence of  
57 the selective inhibitor AK-42 (Koster et al., 2020). The structures and complementary electrophysiology  
58 data presented here provide atomic insight into an N-terminal hairpin gating mechanism for CLC-2  
59 channels.

60

61

## 62 **RESULTS**

### 63 **Overview of cryoEM structure determination**

64 Human CLC-2 (hCLC-2) protein was purified from cultured HEK293 GnT1<sup>-</sup> cells and further  
65 examined by cryoEM single particle analysis. Selected two-dimensional class averages showed a clear  
66 transmembrane domain embedded in a detergent micelle and features indicating an intracellular domain.  
67 Further refinement revealed a well-resolved transmembrane (TM) domain density at 2.46 Å, "CLC2-TM"  
68 (**Figure 2; Figure 2 - figure supplements 1-3**). Density for the C-terminal intracellular domain (CTD) is  
69 less well resolved. Such relatively weak density for the CTD relative to the TM domain was also observed  
70 in the cryoEM analysis of human CLC-1 (Park and MacKinnon, 2018; Wang et al., 2019), which is hCLC-  
71 2's closest homolog. The CTD of CLC-0, a CLC-1 ortholog from *Torpedo marmorata* (Steinmeyer et al.,  
72 1991) displays large movements in spectroscopic studies (Bykova et al., 2006; Alioth et al., 2007). Thus,  
73 conformational flexibility in the CTD appears to be a shared feature within this branch of the CLC family.  
74 To further characterize CTD map density, 3D classification was performed. Amongst ten 3D classes  
75 identified, two showed significantly improved density for the CTD. With non-uniform refinement and  
76 further local refinement, we determined two conformations of CLC-2 structures at 2.75 and 2.76 Å,  
77 respectively (**Figure 2 - figure supplement 3**).

78

79 **Structure of the transmembrane domain**

80 The TM region of CLC-2 displays a typical CLC family homodimeric structure, with each subunit  
81 containing an independent Cl<sup>-</sup> pathway (**Figure 2A, B**). In the cryoEM map, clear density for the E<sub>gate</sub>  
82 residue (E205 in CLC-2) reveals it occupying the “down” position, at the S<sub>cen</sub> Cl<sup>-</sup> binding site (**Figure 2C**).  
83 This downward E<sub>gate</sub> positioning has previously been observed only in the x-ray crystallographic structure  
84 of the *C. merolae* CLC transporter homolog (cmCLC) (Feng et al., 2010), but not in any CLC channel  
85 homolog (**Figure 2 – figure supplement 4A,B**). In the recent CLC-2 structure by Ma et al., E<sub>gate</sub> lacked  
86 density and was modeled in two different conformations (Ma et al., 2023) (**Figure 2 – figure supplement**  
87 **4C**). Our cryoEM map also reveals a density feature at the S<sub>ext</sub> site, indicating a bound Cl<sup>-</sup> ion (**Figure**  
88 **2C**). The ion is stabilized by surrounding backbone nitrogen atoms, a characteristic feature of CLCs.

89 In the down position, E<sub>gate</sub> physically occupies the S<sub>cen</sub> Cl<sup>-</sup> binding site, thus suggesting the  
90 structure represents a closed conformational state, as expected at zero mV (**Figure 1B**). To further  
91 evaluate the conformational state, we used Caver (Chovancova et al., 2012) to detect pathways through  
92 the protein. A continuous pathway through the protein could only be detected with a very small probe  
93 radius of 0.5 Å. In this case, the route detected follows the canonical Cl<sup>-</sup> transport pathway from the  
94 extracellular side to S<sub>cen</sub>, but then circumnavigates E<sub>gate</sub> to reach the intracellular pathway (**Figure 3A,**  
95 **movie 1**). The pinch point of ~0.7 Å near the E<sub>gate</sub> residue is too narrow for a Cl<sup>-</sup> ion and thus indicates a  
96 closed conformational state. The CLC-2 pathway is constricted compared to that in CLC-1, where the  
97 location of E<sub>gate</sub> in the “out” position permits a wider Cl<sup>-</sup> diffusion pathway (**Figure 3B, movie 2**). Close-  
98 up views of the canonical Cl<sup>-</sup> pathway in CLC-2 and CLC-1 are shown in **Figure 3 – figure supplement**  
99 **1**.

100 At the CLC inner-gate region, near conserved residues Tyr<sub>C</sub> (Y553) and Ser<sub>C</sub> (S162), the  
101 canonical (primary) Cl<sup>-</sup> permeation pathway is similar for CLC-2 and CLC-1 and wider than that seen in  
102 the CLC transporters (**Figure 3 – figure supplement 2A, B, movie 3**). CLC-2 also displays a bifurcated  
103 pore, with a secondary pathway to the intracellular side, distinct from the primary pathway common to  
104 CLC family members. The secondary pathway is shared with CLC-1 but not seen in other CLC homologs

105 of known structure. While the functional role of this distinctive secondary pore is not yet known, it is  
106 intriguing to note it is located near the region thought to act as a conduit for H<sup>+</sup> in the CLC transporters  
107 (**Figure 3 – figure supplement 2C**).

108

### 109 **Two conformations of the intracellular domain**

110 All eukaryotic CLCs contain a pair of “cystathionine β-synthase” (CBS) domains in their  
111 intracellular C-terminal domain (Jentsch and Pusch, 2018). CBS domains are found in a wide variety of  
112 functionally unrelated protein families, in all kingdoms of life, where they serve to regulate the activity of  
113 the attached protein (Ereno-Orbea et al., 2013; Anashkin et al., 2017). In the CLCs, mutations in or near  
114 the CBS domains alter channel gating and are associated with human disease, including myotonia,  
115 Dent’s disease, Bartter syndrome, osteopetrosis, leukoencephalopathy, retinal degeneration, lysosomal  
116 storage disease, and neurodevelopmental disorders (Estevez et al., 2004; Giorgio et al., 2017; Jentsch  
117 and Pusch, 2018; Guo et al., 2019; Nicoli et al., 2019; Altamura et al., 2020; Ganesello et al., 2020;  
118 Duncan et al., 2021; Zifarelli, 2022; Palmer et al., 2023; Xu et al., 2023). Structurally, the CLC CBS  
119 domains interact across subunits, forming dimers of dimers and thus increasing the overall interaction  
120 area of the homodimer (Feng et al., 2010; Park et al., 2017; Park and MacKinnon, 2018; Wang et al.,  
121 2019; Schrecker et al., 2020). Structural rearrangement of the C-terminal domains is thought to occur  
122 during channel gating (Yamada et al., 2016; Jentsch and Pusch, 2018) and has been observed  
123 spectroscopically (Bykova et al., 2006; Ma et al., 2011), but no rearrangements have yet been observed  
124 at high resolution.

125 During the 3D classification data processing with a C1 reconstruction (no symmetry imposed),  
126 two distinct conformations were separated from the same CLC-2 dataset (**Figure 2 - figure supplement**  
127 **2**). Structural comparison of these two classes reveals that they are very similar in the transmembrane  
128 domain, with RMSD of 0.58 Å and 0.42 Å for the two subunits. The main structural differences occur at  
129 the intracellular domain, with one class exhibiting a symmetric arrangement and the other, asymmetric.  
130 These two conformations are named as CLC2-CTDsym and CLC2-CTDasym, respectively (**Figure 4**,

131 **Figure 4 - figure supplements 1,2).** In both classes, the CBS domains can be fit to the density, but the  
132 remaining residues 645-743 in the CLC-2 C-terminal domain are not observed and thus no Q scores  
133 (Pintilie et al., 2020) are computed (**Figure 4 – figure supplement 1**). In the asymmetric arrangement  
134 (CLC2-CTDasym), one of the CTDs rotates toward the TM region approximately 35° relative to the  
135 conformation in the symmetric structure (**Figure 4B**). Structural comparison focused on individual CTDs  
136 within the two classes reveals low RMSD values (~1 Å), which indicates that the CTD undergoes a rigid  
137 body movement to accomplish the conformational change (**Figure 4C, movie 4**). Molecular dynamics  
138 (MD) simulations confirm conformational dynamics consistent with a domain rotation (**Figure 4 – figure**  
139 **supplement 3**). In both structures, the orientation of the CTD relative to the membrane is substantially  
140 different from that observed in other CLC structures (**Figure 4 - figure supplement 4**).

141

#### 142 **The hairpin structure corresponds to the N-terminal region**

143 Another new feature of the determined CLC-2 structure is a hairpin density blocking the main Cl<sup>-</sup>  
144 pathway on the intracellular side (**Figure 4A**). This feature is not continuous with any other protein density  
145 in the map. In theory, such density could arise from a protein sequence on CLC-2 (from the unstructured  
146 N- or C-terminal regions) or from a separate protein carried along in the purification. Given the history of  
147 studies on CLC-2 gating, we first considered the CLC-2 N-terminal region.

148 Shortly after the initial cloning of CLC-2 (Thiemann et al., 1992), experiments on CLC-2 expressed  
149 in *Xenopus* oocytes demonstrated that deletion of an 18-residue segment of the N-terminus yielded a  
150 constitutively open channel, lacking the characteristic voltage-dependent gating of CLC-2, and that  
151 transplantation of this segment to the C-terminal domain restored gating (Grunder et al., 1992). Further,  
152 mutation of certain residues in the transmembrane domain (at a putative “receptor” site for the N-terminal  
153 blockade) also yielded an open-channel phenotype (Jordt and Jentsch, 1997). Based on these results, it  
154 was argued that CLC-2 has a “ball-and-chain” type gating mechanism reminiscent of that occurring in the  
155 *Shaker* potassium channel (Zagotta et al., 1990). However, experiments performed using the inside-out  
156 patch clamp configuration (Pusch et al., 1999) or using whole-cell recording with CLC-2 expressed in



157 mammalian cells (Varela et al., 2002) failed to recapitulate the gating phenotype and called into question  
158 a ball-and-chain mechanism. Thus, while mutations in the N-terminus of CLC-2 influence gating, the  
159 precise mechanism-of-action has been uncertain.

160 Our cryoEM map allowed continuous modeling of the CLC-2 sequence starting from the first TM  
161 helix (residue 88). The lack of sufficient density for modeling residues 1-87 suggests that the N terminal  
162 cytoplasmic region of CLC-2 is intrinsically disordered. However, our observation of a resolvable hairpin  
163 density at the intracellular pore, together with the previous hypothesis of N-terminal ball-and-chain gating  
164 for CLC-2, prompted us to consider whether the hairpin density corresponds to N-terminal residues. We  
165 tested several candidate fragments from the CLC-2 N-terminal region and found that the hairpin density  
166 fits perfectly with residues corresponding to 14-28 (**Figure 5A**). Inspection of the Q-score validation plot  
167 for these residues shows they have higher values than the Q-score expected for the corresponding  
168 resolution (**Figure 5B**), which indicates reliable model building at this resolution (Pintilie et al., 2020).  
169 These residues are conserved throughout the mammalian CLC-2 homologs and partially conserved in  
170 *Drosophila* CLC-2 (**Figure 5 - figure supplement 1**).

171 Interestingly, the presence of the N-terminal hairpin is associated with conformational changes in  
172 the CTD and TM domains. In CLC2-CTD<sub>sym</sub>, N-terminal density was observed on both subunits. In  
173 CLC2-CTD<sub>asym</sub>, only the subunit whose CTD adopts the “symmetric” orientation (seen in CLC2-  
174 CTD<sub>sym</sub>) contains the hairpin density; in the subunit with the rotated CTD, no hairpin density is observed  
175 (**Figure 4, Figure 5A**). Along with the absence of hairpin density, the subunit with the rotated CTD  
176 exhibits a difference in the linker connecting transmembrane helices J and K, which is poorly resolved  
177 and insufficient for model building. In contrast, the subunits with the hairpin density contain reliable  
178 density in the JK-linker region, allowing confident modeling of an alpha helix (“JK-helix”, **Figure 5A**). This  
179 observation suggests that the JK-helix stabilizes the N-terminal hairpin peptide. Indeed, residues on the  
180 JK-helix interact directly with residues at the peptide’s hairpin turn (**Figure 5C**). Interactions with other  
181 regions in the TM domain (near helices C, D, J, and R) appear to further stabilize the hairpin in its binding  
182 site. MD simulations help separately validate the assignment and stability of the hairpin: in MD simulations

183 initiated from the structure, we found that the N-terminus remained tightly associated with the channel in  
184 all simulations (**Figure 5 – figure supplement 2**).

185

### 186 **Functional support for pore block by the N-terminal hairpin structure**

187 The hairpin structure appears to directly block the pore (**Figure 5 – figure supplement 3**). To  
188 evaluate the potential functional effect of pore block by the N-terminal hairpin, we performed whole-cell  
189 patch clamp recording on CLC-2, both WT and a deletion mutant lacking the hairpin residues (“Delta-N”),  
190 expressed in CHO cells. Delta-N CLC-2 exhibits currents that display less rectification and faster  
191 activation kinetics than WT CLC-2 (**Figure 6A-B, Figure 6 – figure supplement 1**). This gating  
192 phenotype is intermediate between the non-rectifying phenotype of N-deletion constructs from whole-cell  
193 recordings in oocytes (Jordt and Jentsch, 1997) and the highly rectifying phenotype from whole-cell  
194 recordings in HEK 293 cells (Varela et al., 2002). The Discussion section addresses the variability  
195 observed in CLC-2 current recordings. As was reported for N-deletion currents in oocytes, our Delta-N  
196 currents are substantially larger than WT currents, ~6-fold on average when identical transfection  
197 conditions are used (**Figure 6C**). This difference cannot be explained by a difference in plasma-  
198 membrane expression, as surface biotinylation experiments revealed that expression levels of the two  
199 constructs are within 30% of one another (**Figure 6D, E**).

200 Strikingly, WT but not Delta-N CLC-2 currents “run up” during recording sessions. In patch-clamp  
201 recording experiments, the term “run-up” describes a progressive increase in current that occurs after  
202 the initial measurement. To quantify CLC-2 run-up, we developed the following protocol: (1) on acquisition  
203 of whole-cell recording mode, an initial voltage-family of currents was recorded, as in **Figure 6A**; (2) from  
204 a holding potential of 0 mV, a single 1-s test pulse to -100 mV was repeated every 5 seconds to monitor  
205 time-dependent changes in current amplitude over 5 minutes, after which a second voltage-family of  
206 currents was recorded; (3) 300 nM AK-42 was added to selectively block all CLC-2 current (Koster et al.,  
207 2020), and the steady state inhibition current was used for leak subtraction. In contrast to chloride-  
208 channel inhibitors historically used in electrophysiological experiments (Sepela and Sack, 2018), AK-42

209 is potent and highly selective for CLC-2 over other anion channels (Koster et al., 2020). Representative  
210 current traces and summary data for this set of experiments are shown in **Figure 6F, G**; individual I-V  
211 traces are shown in **Figure 6 – figure supplement 1**. The increase in WT but not Delta-N CLC-2 currents  
212 over time is consistent with an “unblocking” of the pore by release of the N-terminal hairpin peptide.

213 The increase in WT currents is accompanied by an apparent decrease in channel rectification,  
214 towards the level displayed by Delta-N CLC-2. WT CLC-2 currents recorded in heterologous and native  
215 expression systems are generally highly inwardly rectifying. Analogous to a rectifier in an electrical circuit,  
216 WT CLC-2 acts as a directional current valve, allowing much larger absolute currents to flow at negative  
217 membrane potentials compared to positive ones. At the beginning of each recording, our WT CLC-2  
218 currents display such inward rectification, but this characteristic appears to diminish during five minutes  
219 of repeated voltage pulsing to -100 mV, as substantial currents at positive voltages appear. For the  
220 experiment shown in **Figure 6F**, the steady-state current at +80 mV increases from 161 pA to 902 pA,  
221 almost six-fold, compared to a 2.4-fold increase at -100 mV. This observation is surprising because WT  
222 CLC-2 has been characterized as passing little to no current at positive voltages (Park et al., 1998;  
223 Arreola et al., 2002). We initially considered that the increase in current at +80 mV could be due to the  
224 patch-clamp seal becoming leaky over time or that a background channel is being activated; however,  
225 such ‘leak’ currents would not be expected to be blocked by the small molecule inhibitor AK-42, which is  
226 highly selective for CLC-2 over all other CLCs and anion channels (Koster et al., 2020). AK-42 block of  
227 the augmented +80 mV currents seen at the end of each WT CLC-2 recording supports the idea that the  
228 hairpin peptide may contribute to the inward rectification of CLC-2 (**Figure 6F, Figure 6 – figure**  
229 **supplement 2**).

230

### 231 **AK-42 bound structure**

232 AK-42’s selectivity empowered our biophysical studies of CLC-2 and will also be invaluable for  
233 studies of CLC-2’s physiological function. We determined the structure of CLC-2 in complex with AK-42  
234 (**Figure 7**). While the TM domain could be resolved to 2.7 Å, the CTD exhibited poor density compared

235 to the apo sample and did not allow us to confidently model the CTD when masking the whole protein for  
236 refinement. To improve the density quality, we masked the CTD only for refinement; this masking  
237 provided an acceptable density map at 4 Å and allowed us to confidently dock the CTD from apo structure  
238 (**Figure 7 – figure supplements 1-4**).

239 Like the apo CLC-2 structure, the TM domain of CLC2-TM-AK42 is well-resolved with clear  
240 densities for AK-42 and for CLC-2 sidechains, including the E<sub>gate</sub> sidechain (**Figure 7 – figure**  
241 **supplements 5,6**). The overall density for CLC2-TM-AK42 is very similar to that observed in apo CLC-  
242 2, but with an extra density that fits very well to the AK-42 molecule (**Figure 7B, Movie 5**). Residues in  
243 the AK-42 binding pocket exhibit little conformational change between the apo and AK-42 bound CLC-2  
244 structures. The exception is residue M460, which moves ~3 Å to avoid a clash with AK-42's phenyl ring  
245 (**Figure 7 - figure supplement 7**). Located at the extracellular side of Cl<sup>-</sup> pathway, the bound AK-42  
246 appears to directly block Cl<sup>-</sup> permeation (**Figure 7C**). This AK-42 binding pocket is the same as observed  
247 in the docking prediction we previously made using a CLC-2 homology model (Koster et al., 2020). In  
248 that docking study, the top docking poses varied in detail, and therefore the specific interactions were not  
249 certain, but the general position of the binding site is confirmed by our cryoEM structure. Two  
250 conformations were found to fit the density well with the carboxyl group on opposite sides. They were  
251 tested using the Quantum Mechanical Restraints (QMR) method (Liebschner et al., 2023); one had  
252 significantly lower energy (~17 kcal/mol) and strain on the ligand (10.2 kcal/mol), considering the ligand  
253 and nearby residues only. For the lower energy conformation, the Q-scores of AK-42 in the map are 0.74  
254 and 0.76 in the two subunits, respectively. Both are higher than the expected Q-score at this resolution  
255 (0.64), which indicates a good fit of AK-42 to the cryoEM density (Pintilie et al., 2020). A similar AK-42  
256 binding pose was observed in another recently published structure of CLC-2 (Ma et al., 2023).

257 In the binding site, AK-42's phenyl ring nestles into a hydrophobic pocket lined by F306, F463,  
258 F459, M460 and L524 (**Figure 7B**). The carboxyl group of AK-42 forms hydrogen bonds with the side  
259 chain of S392 and backbone of K394 (**Figure 7B**). These polar interactions are consistent with  
260 mutagenesis data. At 30 nM AK-42, inhibition of S392A is reduced ~50% compared to WT, consistent

261 with disruption of the observed hydrogen bond, while inhibition of K394A is not significantly different from  
262 WT, consistent with a backbone rather than a side-chain interaction (Koster et al., 2020; Ma et al., 2023).  
263 A third hydrogen bond – between K204 and the pyridine nitrogen of AK-42 – also contributes to AK-42's  
264 stability in the binding pocket. A pivotal role for the pyridine nitrogen was discovered during the  
265 development of AK-42, where it was found that inhibitor potency is increased by over two orders of  
266 magnitude by addition of a nitrogen at this position but not by addition of a nitrogen at any other position  
267 in the ring (Koster et al., 2020). The interaction of this pyridine nitrogen with K204 is supported by  
268 mutagenesis data, which shows that inhibition of K204M and K204R (K210M and K210R in rat CLC-2)  
269 is reduced ~3-fold compared to WT (Koster et al., 2020; Ma et al., 2023). The distance between the  
270 nitrogen atoms on K204 and AK-42 is 3.6 Å, within acceptable hydrogen bond distance, while the  
271 distances between K204 and any other atoms on AK-42 are too far to allow hydrogen bond formation.

272 Notably, density corresponding to the N-terminal hairpin structure is not seen in the AK-42 bound  
273 structure. After intensive 3D classification, only very minimal hairpin density was observed in a few  
274 classes. It thus appears that the majority of AK-42 bound CLC-2 particles have a flexible N-terminus that  
275 is not blocking the Cl<sup>-</sup> pathway. There is no obvious explanation for this difference compared to the apo  
276 structure. The orientation of the CTD in the AK-42 bound structure is the same as observed in the apo  
277 structure that shows N-terminal hairpin binding; the density for the J-K helix is weaker than in the apo  
278 dataset, but still sufficient to allow modeling of the helix. The TM regions also appear similar. To scrutinize  
279 for subtle conformational changes, we calculated a distance difference matrix (Nishikawa, 1972)  
280 comparing CLC2-TM and AK-42 bound CLC-2 (**Figure 7 – figure supplement 8**). The minor changes  
281 observed do not readily suggest a structure-based hypothesis for the observed difference in N-terminus.  
282 It could be that AK-42 inhibits dynamics that are essential for hairpin peptide binding.

## 283 **DISCUSSION**

284 Our CLC-2 channel structures display quintessential CLC characteristics, including a  
285 homodimeric arrangement of subunits, transmembrane domains composed of 18 helical segments, and  
286 conserved residues surrounding central anion-binding sites  $S_{\text{ext}}$  and  $S_{\text{cen}}$  (Jentsch and Pusch, 2018). At  
287 2.5 Å resolution, we observe clear density for critical features, including a  $\text{Cl}^-$  ion at  $S_{\text{ext}}$  and the  $E_{\text{gate}}$   
288 residue at  $S_{\text{cen}}$  (**Figure 2C**). In this position,  $E_{\text{gate}}$  blocks the pore, generating a closed conformational  
289 state – as expected for CLC-2 at 0 mV (**Figure 1**).

290

### 291 **AK-42 binding site and inhibition potency**

292 A distinctive feature of AK-42—unique amongst CLC inhibitors—is its high selectivity for CLC-2  
293 versus other channels, transporters, and receptors (Koster et al., 2020). The  $\text{IC}_{50}$  for inhibition of CLC-2  
294 by AK-42 (17 nM) is more than four orders of magnitude lower than the  $\text{IC}_{50}$  for inhibition of CLC-1, CLC-  
295 2's closest homolog. CLC-1 and CLC-2 are 50% identical overall, and within the AK-42 binding site only  
296 five residues are different (**Figure 7 – figure supplement 9**). Structural comparison of CLC-1 (PDB  
297 ID:6coy) with CLC2-AK42 reveals that these five residues (I112 (S139), S392 (M419), Q393 (P420),  
298 K394 (R421), and L397 (I424)) exhibit only relatively minor differences in backbone conformation. While  
299 the S392 side chain contributes to a hydrogen-bond interaction with AK-42 (**Figure 7B**), which M419 in  
300 CLC-1 cannot provide, this interaction alone cannot explain the four orders of magnitude difference in  
301 AK-42 potency. Indeed, the mutation S392A reduces inhibition by AK-42 (30 nM) only ~3-fold (Ma et al.,  
302 2023). Similarly, Q393P (Q399P in rat CLC-2) reduces inhibition by less than five-fold (Koster et al., 2020;  
303 Ma et al., 2023). A steric clash between F279 (F252 in CLC-2) and the benzyl substituent in AK-42 may  
304 also contribute to the lack of potency of AK-42 towards CLC-1 (**Figure 7 - figure supplement 9**). In CLC-  
305 2, this same residue (F252) is shifted away from the binding site, opening a sub-pocket that the benzyl  
306 group occupies. This difference is not simply induced by AK-42 binding, as F252 is also shifted away  
307 from the binding site in the CLC-2 apo structure. In the structure-activity relationship studies used to  
308 develop AK-42, the benzyl substituent increased selectivity approximately 5-fold (Koster et al., 2020),

309 thus supporting the significance of this interaction to selectivity. Unfortunately, this hypothesis cannot be  
310 tested through mutagenesis experiments due to the extremely low expression of F252 mutants (Ma,  
311 2023).

312 The pathway from the extracellular solution appears sufficiently wide for AK-42 to worm its way  
313 into the binding site (**Figure 7C**). It is not yet known whether this pathway becomes wider in the CLC-2  
314 open state nor whether inhibition by AK-42 is state-dependent. Studies to address this question would  
315 be valuable for understanding CLC-2 conformational change and gating dynamics.

316

### 317 **E<sub>gate</sub> conformation**

318 CLC-2 is the first CLC channel homolog to be seen in a closed conformational state. While it was  
319 expected that E<sub>gate</sub> would localize to the Cl<sup>-</sup>-permeation pathway in the closed conformational state, it  
320 was not certain whether the S<sub>ext</sub> or S<sub>cen</sub> site would be preferred. The structure of CLC-1 provides an  
321 argument that S<sub>ext</sub> might be preferred. In CLC-1, anion density is observed at S<sub>ext</sub> but not at S<sub>cen</sub> (Park  
322 and MacKinnon, 2018). It was hypothesized that the lack of density at S<sub>cen</sub> in CLC-1 may reflect a reduced  
323 anion-binding affinity that contributes to increased Cl<sup>-</sup> conduction (higher Cl<sup>-</sup> throughput) by the channels  
324 compared to the transporters (Park and MacKinnon, 2018), as all structures of WT CLC transporters  
325 show anion density (either Cl<sup>-</sup> or E<sub>gate</sub>) at both S<sub>ext</sub> and S<sub>cen</sub> (Dutzler et al., 2003; Chavan et al., 2020;  
326 Schrecker et al., 2020). If true for all channels, one might expect E<sub>gate</sub> in CLC-2 to occupy S<sub>ext</sub> rather than  
327 S<sub>cen</sub> in the closed state; however, we do not observe this, suggesting that decreased anion affinity at S<sub>cen</sub>  
328 is not the universal reason for increased Cl<sup>-</sup> conduction in CLC channels relative to the transporters. It is  
329 unlikely that E<sub>gate</sub> is protonated in our structures, as neutralization of E<sub>gate</sub> in CLC-2 leads to open-channel  
330 phenotypes (Niemeyer et al., 2003; de Santiago et al., 2005). Our CLC-2 structure is consistent with the  
331 predictions made by Arreola and colleagues, who used homology modeling in concert with detailed  
332 electrophysiological analyses to conclude that the CLC-2 gate is formed by the E<sub>gate</sub>-Tyr<sub>C</sub> pair at S<sub>cen</sub> (De  
333 Jesus-Perez et al., 2021). Additional experiments, to directly measure anion affinity and to determine  
334 structures of CLC-2 and CLC-1 in both open and closed conformations are needed to better understand

335 these channels' similarities and differences.

336

### 337 **CTD conformation**

338 CLC-2 is also the first CLC in which two conformations of the CTD are observed. While many  
339 previous studies indicate that conformational change of the CTDs plays a critical role in CLC gating  
340 (Jentsch and Pusch, 2018; Grieschat et al., 2020), the mechanistic details are currently fuzzy. Unlike  
341 other CLC variants, CLC-2 can still conduct Cl<sup>-</sup> when its CTD is removed; however, the modified gating  
342 kinetics of this mutant do suggest a role of the CTD in regulating channel function (Garcia-Olivares et al.,  
343 2008). The impact of mutations in various regions of the CLC-2 CTD further supports its role in gating  
344 (Yusef et al., 2006; Paul et al., 2007; Stolting et al., 2013; Giorgio et al., 2017), as do the effects of ATP  
345 binding on channel kinetics (Saint-Martin et al., 2009; Stolting et al., 2013). While we do not see ATP  
346 bound in our structure (none was added to the protein preparation), the binding-site region overlaps  
347 reasonably well with the structure of the ATP-bound CLC-5 CTD (**Figure 4 – figure supplement 5**). The  
348 physiological significance of an intact CTD is underscored by CTD mutations and truncations of CLC-2  
349 that occur in human leukoencephalopathy and retinal degeneration (Giorgio et al., 2017; Guo et al., 2019;  
350 Xu et al., 2023). It is likely that the structural rearrangement we observe strongly influences channel  
351 gating: the CTD upward hinge rotation restricts access to the hairpin-blocking site and substantially  
352 changes CTD interactions with the transmembrane domain.

353

### 354 **Ball and Chain Gating**

355 Steric block of the Cl<sup>-</sup> permeation pathway by the N-terminal hairpin peptide (**Figure 5**) rekindles  
356 the hypothesis of a “ball-and-chain”-type gating mechanism for CLC-2, first proposed over 20 years ago  
357 (Grunder et al., 1992). In those studies, residue Q19 in the N-terminal hairpin, which hydrogen bonds to  
358 Q153 in the TM domain (**Figure 5C**), was identified as a residue critical to the “ball” blocking mechanism  
359 (Grunder et al., 1992). In follow-up studies, it was concluded that the “receptor” site on the TM domain is  
360 formed by residues in a stretch from 342-351 (Jordt and Jentsch, 1997) on helix J, which also forms part



361 of the hairpin-docking site (**Figure 5C, Figure 5 – figure supplement 4A**). The hairpin-TM interface  
362 identified in our structure also exquisitely harmonizes with results from studying human mutations  
363 associated with primary aldosteronism. These gain-of-function mutations, which map squarely onto the  
364 peptide hairpin and surrounding TM region (**Figure 5 – figure supplement 4B**), cause increases in CLC-  
365 2 currents that depolarize the glomerulosal membrane potential thus leading to disease (Fernandes-Rosa  
366 et al., 2018; Scholl et al., 2018).

367 Our electrophysiology results also support a ball-and-chain gating mechanism. First, we  
368 demonstrate that the increase in current in hairpin-deleted channels reflects an increase in channel  
369 activity rather than an increase in surface expression (**Figure 6D,E**), consistent with loss of a channel-  
370 closing mechanism. Second, we show that WT but not Delta-N CLC-2 currents increase over time (**Figure**  
371 **6F,G**), consistent with relief of hairpin block. Importantly, our use of the selective inhibitor AK-42 (Koster  
372 et al., 2020) provides confidence that the current increase is specific to CLC-2 and not a result of leak or  
373 a run-up of other  $\text{Cl}^-$  currents, which notoriously lurk in all mammalian cells and can confound  
374 interpretation of experimental results. In the context of our structure and the mutagenesis studies  
375 discussed above, our electrophysiological results fortify a ball-and-chain model for CLC-2 gating.

376

### 377 **Revised framework for CLC-2 gating**

378 All CLC channel homologs are homodimers that have two gating mechanisms, one acting on  
379 individual pores within each subunit (“protopore” gating) and one that opens and closes both pores  
380 (“common” gating) (Zuniga et al., 2004; Chen, 2005; Zifarelli and Pusch, 2007; Miller, 2014; Stolting et  
381 al., 2014b, a; Accardi, 2015). Protopore gating is controlled by  $E_{\text{gate}}$  (**Figure 1**), with voltage-dependence  
382 arising from interactions between  $E_{\text{gate}}$  and ions in the pore (Pusch et al., 1999; Niemeyer et al., 2003;  
383 Niemeyer et al., 2009; Sanchez-Rodriguez et al., 2010; Sanchez-Rodriguez et al., 2012; De Jesus-Perez  
384 et al., 2016). Common gating is thought to involve structural rearrangements at the subunit interfaces  
385 and in the cytoplasmic domains (Chen, 1998; Pusch, 2002; Duffield et al., 2003; Bykova et al., 2006; Ma  
386 et al., 2011). In CLC-2, common and protopore gating are highly coupled (Zuniga et al., 2004; de Santiago

387 et al., 2005; De Jesus-Perez et al., 2021). Our structural data provides a new framework for  
388 understanding these gating mechanisms (**Figure 8**).

389

### 390 **Ball-and-chain gating as a potential mechanism for CLC-2 current variability**

391 How do we explain the ostensible discrepancy between our results, which support a ball-and-  
392 chain model, and the previously published results that were used to argue against a ball-and-chain type  
393 gating mechanism? We think the discrepancy is not as dire as it originally seemed. The previous  
394 discrepancy is as follows. In studies of an N-terminal CLC-2 deletion mutant in HEK 293 cells, Varela et  
395 al. observed currents that differed depending on whether whole-cell or nystatin-perforated patch clamp  
396 recording was used: with whole-cell recording, deletion-mutant currents displayed rectification similar to  
397 WT CLC-2 but with much faster kinetics; with perforated-patch recording, currents were voltage  
398 independent and non-rectifying (Varela et al., 2002). At the time, this difference was interpreted to mean  
399 that the open-channel phenotype (and therefore ball-and-chain gating) was artifactual, due to a diffusible  
400 intracellular factor binding to the N-terminal deletion channel, but not the WT channel, locking it open in  
401 the perforated-patch recording configuration (but diffusing away in whole-cell recording experiments).  
402 However, Varela et al. also aptly pointed out that mutagenesis experiments did support a role for the  
403 CLC-2 N-terminus in channel gating. Further, they noted that the different results between their two  
404 recording configurations could be due to differences of physiological relevance, such as osmotic forces  
405 and/or channel-cytoskeleton interactions (Grunder et al., 1992; Ahmed et al., 2000). Such factors could  
406 also explain the differences between our whole-cell recordings and those of Varela et al. We note that  
407 our Delta-N currents observed with whole-cell recording (**Figure 6 – figure supplement 1**) are similar to  
408 currents displayed by the aldosteronism peptide-hairpin mutant G24D in perforated-patch clamp  
409 recordings (Goppner et al., 2019), supporting that our use of whole-cell recording is not introducing an  
410 artifact.

411 We hypothesize that sensitivity of ball-and-chain gating to physiological variables may underlie  
412 the tremendous variation in kinetics and voltage-dependence observed amongst recordings of natively

413 expressed CLC-2 (Bosl et al., 2001; Jentsch and Pusch, 2018). Such variation could arise from  
414 differences in one or more of the factors known to modulate CLC-2 gating – osmotic forces,  
415 transmembrane voltage, ATP, phosphorylation, or interactions with the cytoskeleton or other cellular  
416 proteins (Nighot et al., 2017; Jentsch and Pusch, 2018; Okamoto et al., 2019) – and could be further  
417 modulated by the expression of N-terminal splice variants (Furukawa et al., 1995; Cid et al., 2000). We  
418 propose that mechanistic studies of the CLC-2 gating run-up we report here (**Figure 6F**) will be valuable  
419 to guide studies on the variability of CLC-2 currents in native systems and how it relates to ball-and-chain  
420 gating.

421

## 422 **Summary**

423 The structures and electrophysiological data presented here support a ball-and-chain mechanism for  
424 CLC-2 gating and offer a framework for understanding the tight coupling between common and protopore  
425 gating in CLC-2. In addition, the structures illuminate details for molecular recognition by the selective  
426 inhibitor AK-42, the first and currently only known small-molecule modulator that is both potent and  
427 selective for a CLC family member.

428

## 429 **MATERIALS AND METHODS**

### 430 **Molecular biology and AK-42 synthesis**

431 Full-length human CLC-2 (Uniprot ID: P51788) was fused to a C-terminal twin-strep tag with a  
432 linker of 5'- TCGAATTCTTTTGAAGTTTTGTTTCAAGGTCCAACTGCTGCCGCCGCT-3' containing a  
433 HRV 3C protease cleavage sequence (underlined). This human C-terminal twin-strep-tagged CLC-2  
434 fusion construct was cloned into a modified pFastBac vector that contains a CMV promoter for protein  
435 expression in mammalian cells (Goehring et al., 2014; Park et al., 2017). For electrophysiology and cell  
436 surface protein biotinylation/isolation experiments, the twin-strep tag was replaced by a EGFP tag. A C-  
437 terminal GFP tag was previously shown to have no significant effect on CLC-2 channel kinetics or voltage  
438 dependence (Park, Arreola 1998). In the N-terminal deletion CLC-2 (Delta-N), residues 14-27

439 (ALQYEQTLMYGRYT) were removed from full-length (WT) CLC-2.

440 AK-42 was synthesized and quantified as previously described (Koster et al., 2020)

441

#### 442 **Protein expression/ purification**

443 The full-length CLC-2 construct was transformed to DH10Bac competent cells (Invitrogen) to  
444 isolate baculovirus bacmid. The bacmid was transfected to sf9 cells using Cellfectin-II (Invitrogen) to  
445 produce baculovirus. The baculovirus were then further amplified twice in sf9 cells. The protein was  
446 expressed with HEK293 GnTI<sup>-</sup> cells with the amplified baculovirus. HEK293 GnTI<sup>-</sup> cells were cultured in  
447 Freestyle 293 medium (Invitrogen) supplemented with 2% FBS on a shaker at 37 °C in the presence of  
448 8% CO<sub>2</sub> to a density of 3 × 10<sup>6</sup> cells per ml, then infected with 5% v/v baculovirus. After culturing for  
449 another 8-16 hours, sodium butyrate was added at final concentration of 10 mM, then further expressed  
450 for 48 hours at 37 °C before harvest. Cells were pelleted and stored at -80 °C.

451 Frozen cell pellets were resuspended in resuspension buffer containing 50 mM Hepes, pH 7.5,  
452 300 mM NaCl, 1 mM dithiothreitol (DTT), 1 mM ethylenediaminetetraacetic acid (EDTA), and 1 protease  
453 inhibitor cocktail tablet (MedChem Express), then briefly lysis cells with dounce homogenizer for 10-15  
454 times. Cellular debris were collected by centrifugation at 18k rpm for 30 minutes at 4 °C, and then  
455 resuspended with resuspension buffer supplemented with 1% lauryl maltose neopentyl glycol (LMNG)  
456 and 0.1% cholesteryl semisuccinate (CHS). After extraction for 2 hours, the lysate was centrifuged at 18k  
457 rpm for 40 minutes at 4 °C. The clarified lysate was incubated with 1 mL of strep-Tacin XT high-capacity  
458 resin (IBA) for 2 hours at 4 °C. Resin was washed with wash buffer containing 50 mM Hepes, pH 7.5,  
459 300 mM NaCl, 1 mM DTT, 1 mM EDTA, 0.02% LMNG, and 0.002% CHS. Purified protein was released  
460 from resin with 50 µg HRV 3C protease and incubated at 4 °C for overnight. The retrieved protein was  
461 concentrated to 0.5 ml with Amicon Ultra (50 kDa cutoff, EMD Millipore) and followed by size-exclusion  
462 chromatography (SEC) using a superdex 200 Increased 10/300 chromatography column on an AKTA  
463 Purifier 10 FPLC system (GE Healthcare) with buffer containing 20 mM Hepes, 150 mM NaCl, 1 mM  
464 DTT, 0.5 mM EDTA, 0.002% LMNG, and 0.0002% CHS. Protein fractions were pooled, concentrated

465 with Amicon Ultra (50 kDa cutoff, EMD Millipore) to ~5 mg/ml, and immediately used for cryoEM grid  
466 preparation.

467 For CLC-2 and AK-42 complex, AK-42 was first dissolved in DMSO to 45 mM, then further diluted  
468 with CLC-2 SEC buffer to 2 mM and mixed with purified and concentrated CLC-2 protein (2.9 mg/mL) to  
469 make final solution with CLC-2/AK-42 at a molar ratio of 1:10 (20  $\mu$ M CLC-2 with 200  $\mu$ M AK-42). The  
470 mixture was incubated at 4 °C for 3 hours and then used for cryoEM grid preparation.

471

### 472 **CryoEM data collection and processing**

473 Three microliters of the purified CLC-2 or CLC-2/AK-42 mixture was applied to glow-discharged  
474 copper Quantifoil R1.2/1.3 or R2/1 holey carbon grids (Quantifoil). Grids were incubated for 15 s, then  
475 blotted for 4s or 6s at 100% humidity, then plunge-frozen in liquid-nitrogen-cooled liquid ethane using a  
476 Vitrobot Mark IV (Thermo Fisher Scientific) at 4 °C.

477 The grids were imaged on a Titan Krios electron microscope (Thermo Fisher) operated at 300 kV  
478 with a Falcon 4 direct electron detector (Thermo Fisher Scientific) and SelectrisX energy filter (Thermo  
479 Fisher Scientific). Micrographs were recorded at a magnification of 130,000  $\times$  (pixel size of 0.946 Å per  
480 pixel) with EPU software (Thermo Fisher Scientific) Each image was composed of 40 individual frames  
481 with total cumulative dose of 50 e<sup>-</sup> per Å<sup>2</sup>. For CLC-2 dataset, images were collected with an exposure  
482 time of 7.5 seconds and a dose rate of 6.7 e<sup>-</sup> per second per Å<sup>2</sup> (OR 6.0 e<sup>-</sup> per second per pixel). For  
483 CLC-2/AK-42 dataset, images were collected with an exposure time of 5.6 seconds and a dose rate of  
484 8.9 e<sup>-</sup> per second per Å<sup>2</sup> (OR 8.0 e<sup>-</sup> per second per pixel). Defocus values were set from -1.0  $\mu$ m to -2.0  
485  $\mu$ m.

486 CryoEM data processing was performed mainly using CryoSPARC 3.2 (Structura Biotechnology  
487 Inc), except those mentioned specifically. For CLC-2 sample, a total of 14,198 movie stacks were  
488 subjected to motion correction. The contrast-transfer function (CTF) parameters were estimated using  
489 patch CTF. Initially, a total of 56,091 particles were auto-picked and subjected to reference-free 2D  
490 classification. A total of 7 class averages were selected as templated for automated particle picking. A

491 total of 4,999,780 particles were auto-picked and extracted with a box size of 256 pixels. The extracted  
492 particles were then subjected to 2D classification to remove ice, contaminants, and aggregates. The  
493 following ab initio reconstruction and 3D refinement are all performed with C1 symmetry. The cleared-up  
494 classes were used for ab initio reconstruction with two classes. These models were used as reference  
495 for a heterogenous refinement with no symmetry imposed. The best class from heterogenous refinement  
496 which contained 2,415,222 particles were subjected to non-uniform 3D refinements, followed by local 3D  
497 refinements, yielding final CLC2-TM map at 2.46 Å, as determined by the gold-standard measure of  
498 Fourier shell correlation (FSC) using a cut-off of 0.143. Local resolution was estimated with relion 3.1. To  
499 further improve density map of CTD, the selected 2,415,222 particles were divided into 10 subsets for  
500 3D classification in relion 3.1. A reference map for 3D classification was generated by the 3D ab initio  
501 model in CryoSparc. Two of the classes, containing 56,580 and 39,272 particles respectively, showed  
502 distinct CTD features and were used for further non-uniform 3D refinement and local 3D refinements,  
503 separately. The resolution was determined by Fourier shell correlation (FSC) using a cut-off of 0.143 at  
504 2.75 Å and 2.76 Å, respectively.

505 Processing for CLC2-AK42 sample was executed similarly as described above. In brief, a total of  
506 14,300 movie stacks were motion corrected by CryoSPARC. After auto-picking, 5,214,695 particles were  
507 extracted and subjected to 2D classification. After 2D classification, 2,391,813 particles were used for  
508 non-uniform 3D and local refinement to generate the final 2.74 Å map. To further improve the CTD density  
509 map, 3D classification was performed. The best of the 10 classes, containing 66,251 particles, was used  
510 for further refinement. Local refinement with masking of the CTD allowed a resolution 4.03 Å to be  
511 reached.

512

### 513 **Model building and refinement**

514 The initial model of CLC-2 was generated by SWISS-MODEL using human CLC-1 (PDB:6qvc)  
515 as a homology model. It was fit to each map and manually rebuilt using Coot (Emsley and Cowtan, 2004)  
516 (v0.91). The models were further refined with ISOLDE (Croll, 2018) in ChimeraX (Pettersen et al., 2004)

517 (v.1.6) and Phenix (Liebschner et al., 2019) (v1.20) real space refinement. The two potential  
518 conformations for the AK-42 ligand were tested using the Quantum Mechanical Restraints (QMR) method  
519 (Liebschner et al., 2023). Q-scores were performed with the MapQ Chimera plugin v1.9.12.

520

## 521 **Cell surface protein biotinylation and isolation**

522 CHO K1 cells (ATCC CCL-61) were cultured at 37°C [95/5% O<sub>2</sub>/CO<sub>2</sub> ratio] in F12K media (ATCC,  
523 Catalog no. 30-2004) supplemented with 10% fetal bovine serum (Gibco) and 1% penicillin/streptomycin  
524 (Gibco). Cells were seeded at 5×10<sup>6</sup> in 15-cm dishes. After 48 hours, the confluency reached around  
525 60%, and cells were transfected with 6 µg of CLC-2 plasmid, either WT or Delta-N, using Lipofectamine  
526 LTX, opti-MEM, and PLUS reagent (Invitrogen). For the control sample, CHO cells were seeded at the  
527 same time as the transfected groups and kept culturing in parallel. 48-72 hours after transient  
528 transfection, two 15-cm dishes cells for each sample (WT, Delta-N, or control) were combined to create  
529 one sample for use in the biotinylation of surface proteins assay, which was performed using a Pierce  
530 cell surface protein biotinylation and isolation kit (Thermo Scientific, A44390). Briefly, cells were washed  
531 twice in PBS (0.1 M sodium phosphate, 0.15 M NaCl, pH 7.2) and then incubated with PBS containing  
532 0.25 mg/ml of sulfosuccinimidyl 2-(biotin-amido)-ethyl-1,3-dithiopropionate (EZ-link Sulfo-NHS-SS-biotin,  
533 Pierce) at room temperature for 10 minutes. Cells were incubated in ice-cold TBS (25 mM Tris, 0.15 M  
534 NaCl, pH 7.2) twice to quench the labeling. Cells were then scraped and lysed in lysis buffer from the Kit.  
535 Samples were incubated at 4°C for 30 minutes and then centrifugated at 15,000 × g for 5 minutes.  
536 Following centrifugation, the extracted membrane samples from the supernatant were incubated with 50  
537 µl NeutrAvidin™ Agarose (Pierce) at 4°C for 2 hours, then washed with wash buffer from the kit four  
538 times. Finally, the isolated proteins were eluted with 60 µl elution buffer (from the kit) containing 100 mM  
539 DTT. 40 µl of each sample was used for Western blotting detection with 1:2,500 anti-GFP antibody  
540 (Invitrogen A11122) and 1:10,000 anti-rabbit secondary antibody (Licor 926-68073). The relative  
541 expression level was calculated by quantifying the intensities of the 100-kD bands on the Western blot,  
542 using a Li-Cor Odyssey 9120 Infrared Imaging System. The samples from three independent experiments

543 (independent transfections on different days) were run on a single Western blot, shown in Figure 6C.

544

#### 545 **Cell Culture and patch-clamp recording**

546 CHO K1 cells (ATCC CCL-61) were cultured at 37°C [95/5% O<sub>2</sub>/CO<sub>2</sub> ratio] in F12K media  
547 (ATCC, Catalog no. 30-2004) supplemented with 10% fetal bovine serum (Gibco) and 1%  
548 penicillin/streptomycin (Gibco). At 60% confluency, cells were transfected with 120 ng CLC-2, either WT  
549 or Delta-N, using Lipofectamine LTX, opti-MEM, and PLUS reagent (Invitrogen). 105 ng of a soluble GFP  
550 construct was co-transfected with the CLC-2 construct to improve visualization of transfected cells.

551 Whole-cell patch-clamp experiments were performed using an Axopatch 200B amplifier attached  
552 to a Digidata 1440A. Data were acquired at 10 kHz with filtering at 5 kHz. Traces shown in figures were  
553 filtered offline in Clampfit at 1 kHz (8-pole Bessel). Borosilicate glass micropipettes (Sutter Instruments  
554 BF150-86-10) were pulled and fire-polished to a tip diameter with a resistance of 1.8 to 3.4 MΩ. For  
555 whole-cell patch-clamp recordings, the external solution was composed of 148 mM CsCl, 2 mM CaCl<sub>2</sub>  
556 (from a 1 M aqueous stock), 100 mM D-mannitol, and 10 mM HEPES, adjusted to pH 7.4 with 2 M CsOH.  
557 The internal solution was composed of 146 mM CsCl, 5 mM EGTA, 5 mM NaF, 60 mM D-mannitol, and  
558 10 mM HEPES, adjusted to pH 7.4 with 2 M CsOH. Bath perfusion of external solution (2 mL/min) was  
559 initiated after whole cell and series resistance compensation (70% or more) was established. For leak  
560 subtraction, 300 nM AK-42 was perfused at 2 mL/min. AK-42 was diluted from a 1 mM stock solution in  
561 DMSO (0.03% final [DMSO]).

562

#### 563 **MD simulations**

564 **System setup for MD simulations.** The apo dimer structure was used for simulations. For all  
565 simulations, hydrogen atoms were added, and protein chain termini were capped with neutral acetyl  
566 and methylamide groups. Titratable residues were kept in their dominant protonation state at pH 7.  
567 Histidine residues were modeled as neutral, with a hydrogen atom bound to epsilon nitrogen. The  
568 Dowser program was used to hydrate pockets within and around each structure (Morozenko and



569 Stuchebrukhov, 2016). Then the receptor was inserted into a pre-equilibrated palmitoyl-oleoyl-  
570 phosphatidylcholine (POPC) bilayer using Dabble (Betz, 2017). Sodium and chloride ions were added  
571 to neutralize each system at a concentration of 150 mM. Approximate system dimensions were 131 Å x  
572 95 Å x 125 Å.

573 **Simulation protocols.** All simulations were run on a single Graphical Processing Unit (GPU)  
574 using the Amber18 Compute Unified Device Architecture (CUDA) version of particle-mesh Ewald  
575 molecular dynamics (PMEMD) (Salomon-Ferrer et al., 2013). We used the CHARMM36m parameter  
576 set for protein molecules, lipids, and ions, and the CHARMM TIP3P water model for waters (Huang and  
577 MacKerell, 2013). Heating (to 310 K over 137.5 ps) and equilibration (28 ns with restraints on protein  
578 and ligand) steps were performed before production simulations as described previously (Suomivuori et  
579 al., 2020). Trajectory snapshots were saved every 200 ps. All simulations were at least 2 microseconds  
580 in length.

581 **Simulation analysis protocols.** The AmberTools18 CPPTRAJ package (Roe and Cheatham,  
582 2013) was used to reimage trajectories, while Visual Molecular Dynamics (VMD) (Humphrey et al.,  
583 1996), PyMol (Schrodinger), and Matplotlib Python package were used for visualization and analysis.  
584 For analysis, the N-terminus peptide backbone was defined as segment name P5, excluding residues  
585 14 15 27 28. For the CTD analysis, we used segment names P9 P3 P4 P8 excluding residue 419 to  
586 578. For bar plots, individual dots show the average value in each independent simulation. Bar values  
587 show the average value across the independent simulations. The error bars for simulation results show  
588 the 68% confidence intervals of the mean (appropriate for non-parametric distributions) calculated  
589 using bootstrapping with the Seaborn Python library.

590

## 591 **ACKNOWLEDGMENTS**

592 We thank Huawei Zhang for sharing pdb coordinates and cryo-EM density for CLC-2/AK-42 in advance  
593 of release. We thank Anna Koster, Bill Kobertz, Dan Collins, Jürgen Kreiter, Martin Prieto, Shwetha  
594 Srinivasan, and Chris Miller for comments on the manuscript. We also thank Nigel Moriarty (Phenix) for

595 performing Quantum Mechanical Restraints (QMR) analysis of the AK-42 ligand. This research was  
596 funded by NIH R21NS125767 (M.M. and W.C.) and NIH R01NS113611 (M.M., J.D.B., and R.O.D.).  
597 CryoEM was performed at the Stanford-SLAC Cryo-EM Center (S<sup>2</sup>C<sup>2</sup>), which is supported by  
598 the National Institutes of Health Common Fund Transformative High-Resolution Cryo-Electron  
599 Microscopy program (U24 GM129541). M.X. is supported by a Wu Tsai Neurosciences Institute  
600 Interdisciplinary Scholar Award. S.D.M. is supported by a Stanford Bio-X Bowes fellowship.

601

## 602 **DATA AVAILABILITY**

603 Cryo-EM Density maps and structure coordinates have been deposited in the Electron  
604 Microscopy Data Bank (EMDB) and the Protein Data Bank (PDB), with accession codes EMD-41127 and  
605 PDB 8TA3 for the CLC2-TM, EMD-41128 and PDB 8TA4 for the CLC2-CTDsym, EMD-41129 and PDB  
606 8TA5 for CLC2-CTDasym, EMD-41126 and PDB 8TA2 for CLC2-TM-AK42, and EMD-41130 and PDB  
607 8TA6 for CLC2-AK42-CTD-only.

## REFERENCES

- Accardi, A. 2015. Structure and gating of CLC channels and exchangers. *J. Physiol.* 593:4129-4138.
- Accardi, A., and C. Miller. 2004. Secondary active transport mediated by a prokaryotic homologue of CLC Cl<sup>-</sup> channels. *Nature.* 427:803-807.
- Ahmed, N., M. Ramjeesingh, S. Wong, A. Varga, E. Garami, and C.E. Bear. 2000. Chloride channel activity of CLC-2 is modified by the actin cytoskeleton. *Biochem. J.* 352 Pt 3:789-794.
- Alioth, S., S. Meyer, R. Dutzler, and K. Pervushin. 2007. The cytoplasmic domain of the chloride channel CLC-0: structural and dynamic characterization of flexible regions. *J. Mol. Biol.* 369:1163-1169.
- Altamura, C., J.F. Desaphy, D. Conte, A. De Luca, and P. Imbrici. 2020. Skeletal muscle CLC-1 chloride channels in health and diseases. *Pflugers Arch.* 472:961-975.
- Anashkin, V.A., A.A. Baykov, and R. Lahti. 2017. Enzymes Regulated via Cystathionine beta-Synthase Domains. *Biochemistry (Mosc.)*. 82:1079-1087.
- Arreola, J., T. Begenisich, and J.E. Melvin. 2002. Conformation-dependent regulation of inward rectifier chloride channel gating by extracellular protons. *J. Physiol.* 541:103-112.
- Arreola, J., J.A. De Santiago-Castillo, J.E. Sanchez, and P.G. Nieto. 2008. Gating and trafficking of CLC-2 chloride channel without cystathionine beta-synthase domains. *J. Physiol.* 586:5289.
- Betz, R.M. 2017. v2.6.3. *Zenodo*.
- Bosl, M.R., V. Stein, C. Hubner, A.A. Zdebik, S.E. Jordt, A.K. Mukhopadhyay, M.S. Davidoff, A.F. Holstein, and T.J. Jentsch. 2001. Male germ cells and photoreceptors, both dependent on close cell-cell interactions, degenerate upon CLC-2 Cl<sup>-</sup> channel disruption. *EMBO J.* 20:1289-1299.
- Bykova, E.A., X.D. Zhang, T.Y. Chen, and J. Zheng. 2006. Large movement in the C terminus of CLC-0 chloride channel during slow gating. *Nat. Struct. Mol. Biol.* 13:1115-1119.
- Cederholm, J.M., G.Y. Rychkov, C.J. Bagley, and A.H. Bretag. 2010. Inter-subunit communication and fast gate integrity are important for common gating in hCLC-1. *Int. J. Biochem. Cell Biol.* 42:1182-1188.
- Chavan, T.S., R.C. Cheng, T. Jiang, Mathews, II, R.A. Stein, A. Koehl, H.S. McHaourab, E. Tajkhorshid, and M. Maduke. 2020. A CLC-ec1 mutant reveals global conformational change and suggests a unifying mechanism for the CLC Cl<sup>-</sup>/H<sup>+</sup> transport cycle. *Elife.* 9.
- Chen, T.Y. 1998. Extracellular zinc ion inhibits CLC-0 chloride channels by facilitating slow gating. *J. Gen. Physiol.* 112:715-726.
- Chen, T.Y. 2005. Structure and function of clc channels. *Annu. Rev. Physiol.* 67:809-839.
- Chovancova, E., A. Pavelka, P. Benes, O. Strnad, J. Brezovsky, B. Kozlikova, A. Gora, V. Sustr, M. Klvana, P. Medek, L. Biedermannova, J. Sochor, and J. Damborsky. 2012. CAVER 3.0: a tool for the analysis of transport pathways in dynamic protein structures. *PLoS Comput. Biol.* 8:e1002708.
- Cid, L.P., M.I. Niemeyer, A. Ramirez, and F.V. Sepulveda. 2000. Splice variants of a CLC-2 chloride channel with differing functional characteristics. *Am. J. Physiol. Cell Physiol.* 279:C1198-1210.
- Croll, T.I. 2018. ISOLDE: a physically realistic environment for model building into low-resolution electron-density maps. *Acta Crystallogr D Struct Biol.* 74:519-530.
- De Jesus-Perez, J.J., A. Castro-Chong, R.C. Shieh, C.Y. Hernandez-Carballo, J.A. De Santiago-Castillo, and J. Arreola. 2016. Gating the glutamate gate of CLC-2 chloride channel by pore occupancy. *J. Gen. Physiol.* 147:25-37.
- De Jesus-Perez, J.J., G.A. Mendez-Maldonado, A.E. Lopez-Romero, D. Esparza-Jasso, I.L. Gonzalez-Hernandez, V. De la Rosa, R. Gastelum-Garibaldi, J.E. Sanchez-Rodriguez, and J. Arreola. 2021. Electro-steric opening of the CLC-2 chloride channel gate. *Sci Rep.* 11:13127.
- de Santiago, J.A., K. Nehrke, and J. Arreola. 2005. Quantitative analysis of the voltage-dependent gating

- of mouse parotid CLC-2 chloride channel. *J. Gen. Physiol.* 126:591-603.
- Duan, D.D. 2013. Phenomics of cardiac chloride channels. *Compr Physiol.* 3:667-692.
- Duffield, M., G. Rychkov, A. Bretag, and M. Roberts. 2003. Involvement of Helices at the Dimer Interface in CLC-1 Common Gating. *J. Gen. Physiol.* 121:149-161.
- Duncan, A.R., M.M. Polovitskaya, H. Gaitan-Penas, S. Bertelli, G.E. VanNoy, P.E. Grant, A. O'Donnell-Luria, Z. Valivullah, A.K. Lovgren, E.M. England, E. Agolini, J.A. Madden, K. Schmitz-Abe, A. Kritzer, P. Hawley, A. Novelli, P. Alfieri, G.S. Colafati, D. Wieczorek, K. Platzer, J. Luppe, M. Koch-Hogrebe, R. Abou Jamra, J. Neira-Fresneda, A. Lehman, C.F. Boerkoel, K. Seath, L. Clarke, C. Study, Y. van lerland, E. Argilli, E.H. Sherr, A. Maiorana, T. Diel, M. Hempel, T. Bierhals, R. Estevez, T.J. Jentsch, M. Pusch, and P.B. Agrawal. 2021. Unique variants in CLCN3, encoding an endosomal anion/proton exchanger, underlie a spectrum of neurodevelopmental disorders. *Am. J. Hum. Genet.* 108:1450-1465.
- Dutzler, R., E.B. Campbell, M. Cadene, B.T. Chait, and R. MacKinnon. 2002. X-ray structure of a CLC chloride channel at 3.0 Å reveals the molecular basis of anion selectivity. *Nature.* 415:287-294.
- Dutzler, R., E.B. Campbell, and R. MacKinnon. 2003. Gating the selectivity filter in CLC chloride channels. *Science.* 300:108-112.
- Emsley, P., and K. Cowtan. 2004. Coot: model-building tools for molecular graphics. *Acta Crystallogr. D Biol. Crystallogr.* 60:2126-2132.
- Ereno-Orbea, J., I. Oyenarte, and L.A. Martinez-Cruz. 2013. CBS domains: Ligand binding sites and conformational variability. *Arch. Biochem. Biophys.* 540:70-81.
- Estevez, R., M. Pusch, C. Ferrer-Costa, M. Orozco, and T.J. Jentsch. 2004. Functional and structural conservation of CBS domains from CLC chloride channels. *J. Physiol.* 557:363-378.
- Feng, L., E.B. Campbell, Y. Hsiung, and R. MacKinnon. 2010. Structure of a eukaryotic CLC transporter defines an intermediate state in the transport cycle. *Science.* 330:635-641.
- Feng, L., E.B. Campbell, and R. MacKinnon. 2012. Molecular mechanism of proton transport in CLC Cl<sup>-</sup>/H<sup>+</sup> exchange transporters. *Proc. Natl. Acad. Sci. U. S. A.* 109:11699-11704.
- Fernandes-Rosa, F.L., G. Daniil, I.J. Orozco, C. Goppner, R. El Zein, V. Jain, S. Boulkroun, X. Jeunemaitre, L. Amar, H. Lefebvre, T. Schwarzmayr, T.M. Strom, T.J. Jentsch, and M.C. Zennaro. 2018. A gain-of-function mutation in the CLCN2 chloride channel gene causes primary aldosteronism. *Nat. Genet.* 50:355-361.
- Furukawa, T., S. Horikawa, T. Terai, T. Ogura, Y. Katayama, and M. Hiraoka. 1995. Molecular cloning and characterization of a novel truncated from (CLC-2 beta) of CLC-2 alpha (CLC-2G) in rabbit heart. *FEBS. Lett.* 375:56-62.
- Gaitan-Penas, H., P.M. Apaja, T. Arnedo, A. Castellanos, X. Elorza-Vidal, D. Soto, X. Gasull, G.L. Lukacs, and R. Estevez. 2017. Leukoencephalopathy-causing CLCN2 mutations are associated with impaired Cl<sup>-</sup> channel function and trafficking. *J. Physiol.* 595:6993-7008.
- Garcia-Olivares, J., A. Alekov, M.R. Boroumand, B. Begemann, P. Hidalgo, and C. Fahlke. 2008. Gating of human CLC-2 chloride channels and regulation by carboxy-terminal domains. *J. Physiol.* 586:5325-5336.
- Gianesello, L., D. Del Prete, M. Ceol, G. Priante, L.A. Calo, and F. Anglani. 2020. From protein uptake to Dent disease: An overview of the CLCN5 gene. *Gene.* 747:144662.
- Giorgio, E., G. Vaula, P. Benna, N. Lo Buono, C.M. Eandi, D. Dino, C. Mancini, S. Cavalieri, E. Di Gregorio, E. Pozzi, M. Ferrero, M.T. Giordana, C. Depienne, and A. Brusco. 2017. A novel homozygous change of CLCN2 (p.His590Pro) is associated with a subclinical form of leukoencephalopathy with ataxia (LKPAT). *J. Neurol. Neurosurg. Psychiatry.* 88:894-896.

- Goehring, A., C.H. Lee, K.H. Wang, J.C. Michel, D.P. Claxton, I. Bacongus, T. Althoff, S. Fischer, K.C. Garcia, and E. Gouaux. 2014. Screening and large-scale expression of membrane proteins in mammalian cells for structural studies. *Nat. Protoc.* 9:2574-2585.
- Goppner, C., I.J. Orozco, M.B. Hoegg-Beiler, A.H. Soria, C.A. Hubner, F.L. Fernandes-Rosa, S. Boulkroun, M.C. Zennaro, and T.J. Jentsch. 2019. Pathogenesis of hypertension in a mouse model for human CLCN2 related hyperaldosteronism. *Nat. Commun.* 10:4678.
- Grieschat, M., R.E. Guzman, K. Langschwager, C. Fahlke, and A.K. Alekov. 2020. Metabolic energy sensing by mammalian CLC anion/proton exchangers. *EMBO Rep.* 21:e47872.
- Grunder, S., A. Thiemann, M. Pusch, and T.J. Jentsch. 1992. Regions involved in the opening of ClC-2 chloride channel by voltage and cell volume. *Nature.* 360:759-762.
- Guo, Z., T. Lu, L. Peng, H. Cheng, F. Peng, J. Li, Z. Lu, S. Chen, and W. Qiu. 2019. CLCN2-related leukoencephalopathy: a case report and review of the literature. *BMC Neurol.* 19:156.
- Hansen, T.H., Y. Yan, G. Ahlberg, O.B. Vad, L. Refsgaard, J.L. Dos Santos, N. Mutsaers, J.H. Svendsen, M.S. Olesen, B.H. Bentzen, and N. Schmitt. 2020. A Novel Loss-of-Function Variant in the Chloride Ion Channel Gene *Clcn2* Associates with Atrial Fibrillation. *Sci Rep.* 10:1453.
- Huang, J., and A.D. MacKerell, Jr. 2013. CHARMM36 all-atom additive protein force field: validation based on comparison to NMR data. *J Comput Chem.* 34:2135-2145.
- Humphrey, W., A. Dalke, and K. Schulten. 1996. VMD: visual molecular dynamics. *J. Mol. Graph.* 14:33-38, 27-38.
- Jardetzky, O. 1966. Simple allosteric model for membrane pumps. *Nature.* 211:969-970.
- Jentsch, T.J., and M. Pusch. 2018. CLC Chloride Channels and Transporters: Structure, Function, Physiology, and Disease. *Physiol. Rev.* 98:1493-1590.
- Jeworutzki, E., T. Lopez-Hernandez, X. Capdevila-Nortes, S. Sirisi, L. Bengtsson, M. Montolio, G. Zifarelli, T. Arnedo, C.S. Muller, U. Schulte, V. Nunes, A. Martinez, T.J. Jentsch, X. Gasull, M. Pusch, and R. Estevez. 2012. GlialCAM, a Protein Defective in a Leukodystrophy, Serves as a ClC-2 Cl(-) Channel Auxiliary Subunit. *Neuron.* 73:951-961.
- Jordt, S.E., and T.J. Jentsch. 1997. Molecular dissection of gating in the ClC-2 chloride channel. *EMBO J.* 16:1582-1592.
- Kieferle, S., P. Fong, M. Bens, A. Vandewalle, and T.J. Jentsch. 1994. Two highly homologous members of the ClC chloride channel family in both rat and human kidney. *Proc. Natl. Acad. Sci. U.S.A.* 91:6943-6947.
- Koster, A.K., A.L. Reese, Y. Kuryshev, X. Wen, K.A. McKiernan, E.E. Gray, C. Wu, J.R. Huguenard, M. Maduke, and J. Du Bois. 2020. Development and validation of a potent and specific inhibitor for the CLC-2 chloride channel. *Proc. Natl. Acad. Sci. U. S. A.*
- Lein, E.S., M.J. Hawrylycz, N. Ao, M. Ayres, A. Bensinger, A. Bernard, A.F. Boe, M.S. Boguski, K.S. Brockway, E.J. Byrnes, L. Chen, L. Chen, T.M. Chen, M.C. Chin, J. Chong, B.E. Crook, A. Czaplinska, C.N. Dang, S. Datta, N.R. Dee, A.L. Desaki, T. Desta, E. Diep, T.A. Dolbeare, M.J. Donelan, H.W. Dong, J.G. Dougherty, B.J. Duncan, A.J. Ebbert, G. Eichele, L.K. Estin, C. Faber, B.A. Facer, R. Fields, S.R. Fischer, T.P. Fliss, C. Frensley, S.N. Gates, K.J. Glattfelder, K.R. Halverson, M.R. Hart, J.G. Hohmann, M.P. Howell, D.P. Jeung, R.A. Johnson, P.T. Karr, R. Kawal, J.M. Kidney, R.H. Knapik, C.L. Kuan, J.H. Lake, A.R. Laramée, K.D. Larsen, C. Lau, T.A. Lemon, A.J. Liang, Y. Liu, L.T. Luong, J. Michaels, J.J. Morgan, R.J. Morgan, M.T. Mortrud, N.F. Mosqueda, L.L. Ng, R. Ng, G.J. Orta, C.C. Overly, T.H. Pak, S.E. Parry, S.D. Pathak, O.C. Pearson, R.B. Puchalski, Z.L. Riley, H.R. Rockett, S.A. Rowland, J.J. Royall, M.J. Ruiz, N.R. Sarno, K. Schaffnit, N.V. Shapovalova, T. Sivasay, C.R. Slaughterbeck, S.C. Smith, K.A. Smith, B.I. Smith, A.J. Sodt, N.N. Stewart, K.R. Stumpf, S.M. Sunkin,

- M. Sutram, A. Tam, C.D. Teemer, C. Thaller, C.L. Thompson, L.R. Varnam, A. Visel, R.M. Whitlock, P.E. Wohnoutka, C.K. Wolkey, V.Y. Wong, M. Wood, M.B. Yaylaoglu, R.C. Young, B.L. Youngstrom, X.F. Yuan, B. Zhang, T.A. Zwingman, and A.R. Jones. 2007. Genome-wide atlas of gene expression in the adult mouse brain. *Nature*. 445:168-176.
- Leisle, L., Y. Xu, E. Fortea, S. Lee, J.D. Galpin, M. Vien, C.A. Ahern, A. Accardi, and S. Berneche. 2020. Divergent Cl(-) and H(+) pathways underlie transport coupling and gating in CLC exchangers and channels. *Elife*. 9.
- Liebschner, D., P.V. Afonine, M.L. Baker, G. Bunkoczi, V.B. Chen, T.I. Croll, B. Hintze, L.W. Hung, S. Jain, A.J. McCoy, N.W. Moriarty, R.D. Oeffner, B.K. Poon, M.G. Prisant, R.J. Read, J.S. Richardson, D.C. Richardson, M.D. Sammito, O.V. Sobolev, D.H. Stockwell, T.C. Terwilliger, A.G. Urzhumtsev, L.L. Videau, C.J. Williams, and P.D. Adams. 2019. Macromolecular structure determination using X-rays, neutrons and electrons: recent developments in Phenix. *Acta Crystallogr D Struct Biol*. 75:861-877.
- Liebschner, D., N.W. Moriarty, B.K. Poon, and P.D. Adams. 2023. In situ ligand restraints from quantum-mechanical methods. *Acta Crystallogr D Struct Biol*. 79:100-110.
- Lisal, J., and M. Maduke. 2008. The ClC-0 chloride channel is a 'broken' Cl-/H+ antiporter. *Nat. Struct. Mol. Biol*. 15:805-810.
- Ma, L., G.Y. Rychkov, E.A. Bykova, J. Zheng, and A.H. Bretag. 2011. Movement of hClC-1 C-termini during common gating and limits on their cytoplasmic location. *Biochem. J*. 436:415-428.
- Ma, T., L. Wang, A. Chai, C. Liu, W. Cui, S. Yuan, S. Wing Ngor Au, L. Sun, X. Zhang, Z. Zhang, J. Lu, Y. Gao, P. Wang, Z. Li, Y. Liang, H. Vogel, Y.T. Wang, D. Wang, K. Yan, and H. Zhang. 2023. Cryo-EM structures of ClC-2 chloride channel reveal the blocking mechanism of its specific inhibitor AK-42. *Nat. Commun*. 14:3424.
- Maduke, M.C., and R.J. Reimer. 2012. Biochemistry to the rescue: a ClC-2 auxiliary subunit provides a tangible link to leukodystrophy. *Neuron*. 73:855-857.
- Miller, C. 2006. ClC chloride channels viewed through a transporter lens. *Nature*. 440:484-489.
- Miller, C. 2014. In the beginning: A personal reminiscence on the origin and legacy of ClC-0, the "Torpedo Cl- channel". *J. Physiol*.
- Miller, C. 2021. Q-cubed mutant cues clues to CLC antiport mechanism. *J. Gen. Physiol*. 153.
- Morozenko, A., and A.A. Stuchebukhov. 2016. Dowser++, a new method of hydrating protein structures. *Proteins*. 84:1347-1357.
- Nicoli, E.R., M.R. Weston, M. Hackbarth, A. Becerril, A. Larson, W.M. Zein, P.R. Baker, 2nd, J.D. Burke, H. Dorward, M. Davids, Y. Huang, D.R. Adams, P.M. Zerfas, D. Chen, T.C. Markello, C. Toro, T. Wood, G. Elliott, M. Vu, N. Undiagnosed Diseases, W. Zheng, L.J. Garrett, C.J. Tifft, W.A. Gahl, D.L. Day-Salvatore, J.A. Mindell, and M.C.V. Malicdan. 2019. Lysosomal Storage and Albinism Due to Effects of a De Novo CLCN7 Variant on Lysosomal Acidification. *Am. J. Hum. Genet*. 104:1127-1138.
- Niemeyer, M.I., L.P. Cid, Y.R. Yusef, R. Briones, and F.V. Sepulveda. 2009. Voltage-dependent and -independent titration of specific residues accounts for complex gating of a ClC chloride channel by extracellular protons. *J. Physiol*. 587:1387-1400.
- Niemeyer, M.I., L.P. Cid, L. Zuniga, M. Catalan, and F.V. Sepulveda. 2003. A conserved pore-lining glutamate as a voltage- and chloride-dependent gate in the ClC-2 chloride channel. *J. Physiol*. 553:873-879.
- Nighot, P.K., L. Leung, and T.Y. Ma. 2017. Chloride channel ClC- 2 enhances intestinal epithelial tight junction barrier function via regulation of caveolin-1 and caveolar trafficking of occludin. *Exp. Cell*

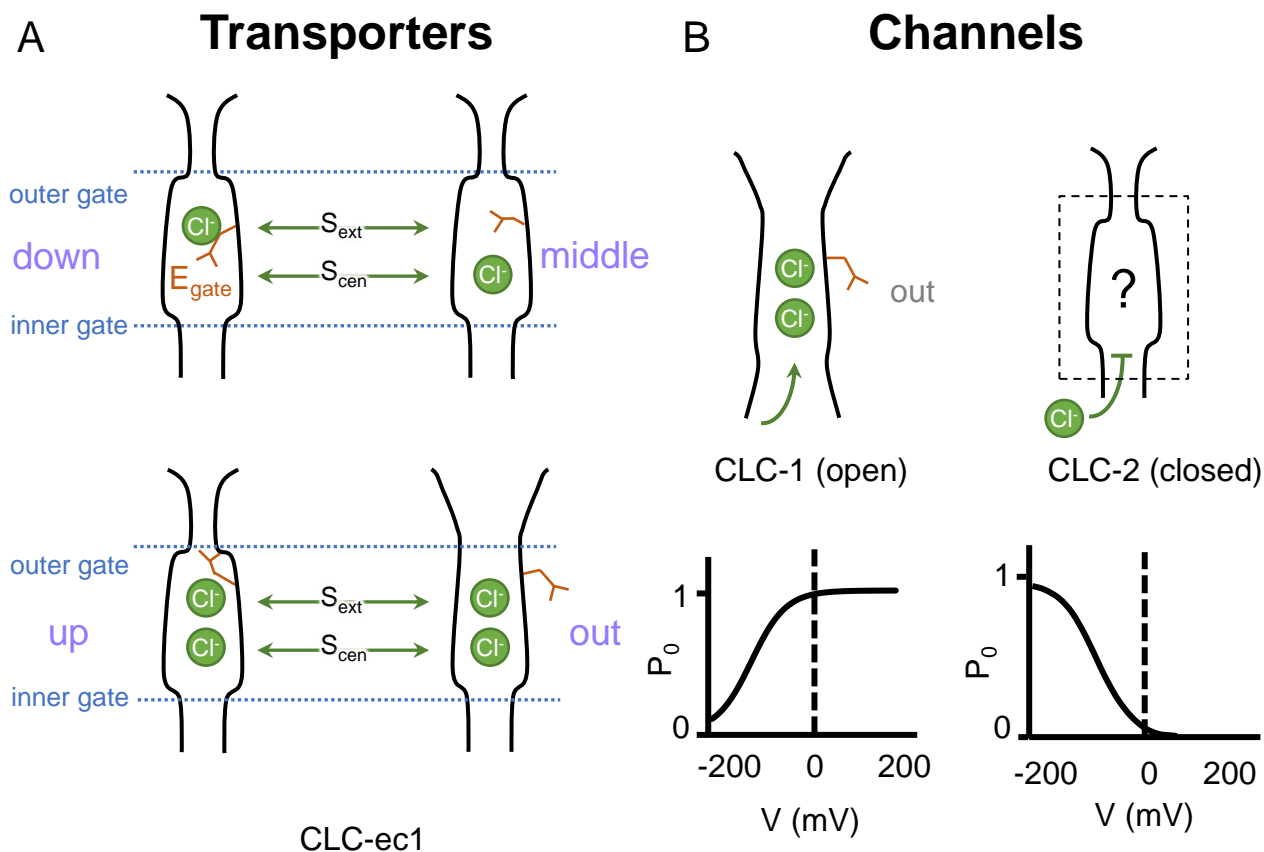
Res. 352:113-122.

- Nishikawa, K.O., T.; Isogai, Y.; Saitô, N. 1972. Tertiary Structure of Proteins. I. Representation and Computation of the Conformations. *Journal of the physical society of Japan*. 32.
- Okamoto, Y., Y. Nagasawa, Y. Obara, K. Ishii, D. Takagi, and K. Ono. 2019. Molecular identification of HSPA8 as an accessory protein of a hyperpolarization-activated chloride channel from rat pulmonary vein cardiomyocytes. *J. Biol. Chem.* 294:16049-16061.
- Palmer, E.E., M. Pusch, A. Picollo, C. Forwood, M.H. Nguyen, V. Suckow, J. Gibbons, A. Hoff, L. Sigfrid, A. Megarbane, M. Nizon, B. Cogne, C. Beneteau, F.S. Alkuraya, A. Chedrawi, M.O. Hashem, H. Stamberger, S. Weckhuysen, A. Vanlander, B. Ceulemans, S. Rajagopalan, K. Nunn, S. Arpin, M. Raynaud, C.S. Motter, C. Ward-Melver, K. Janssens, M. Meuwissen, D. Beysen, N. Dikow, M. Grimm, T.B. Haack, E. Clement, A. McTague, D. Hunt, S. Townshend, M. Ward, L.J. Richards, C. Simons, G. Costain, L. Dupuis, R. Mendoza-Londono, T. Dudding-Byth, J. Boyle, C. Saunders, E. Fleming, S. El Chehadeh, M.A. Spitz, A. Piton, B. Gerard, M.T. Abi Warde, G. Rea, C. McKenna, S. Douzgou, S. Banka, C. Akman, J.M. Bain, T.T. Sands, G.N. Wilson, E.J. Silvertooth, L. Miller, D. Lederer, R. Sachdev, R. Macintosh, O. Monestier, D. Karadurmus, F. Collins, M. Carter, L. Rohena, M.H. Willemsen, C.W. Ockeloen, R. Pfundt, S.D. Kroft, M. Field, F.E.R. Laranjeira, A.M. Fortuna, A.R. Soares, V. Michaud, S. Naudion, S. Golla, D.D. Weaver, L.M. Bird, J. Friedman, V. Clowes, S. Joss, L. Polsler, P.M. Campeau, M. Blazo, E.K. Bijlsma, J.A. Rosenfeld, C. Beetz, Z. Powis, K. McWalter, T. Brandt, E. Torti, M. Mathot, S.S. Mohammad, R. Armstrong, and V.M. Kalscheuer. 2023. Functional and clinical studies reveal pathophysiological complexity of CLCN4-related neurodevelopmental condition. *Mol. Psychiatry*. 28:668-697.
- Park, E., E.B. Campbell, and R. MacKinnon. 2017. Structure of a CLC chloride ion channel by cryo-electron microscopy. *Nature*. 541:500-505.
- Park, E., and R. MacKinnon. 2018. Structure of the CLC-1 chloride channel from Homo sapiens. *Elife*. 7.
- Park, K., J. Arreola, T. Begenisich, and J.E. Melvin. 1998. Comparison of voltage-activated Cl<sup>-</sup> channels in rat parotid acinar cells with ClC-2 in a mammalian expression system. *J. Membr. Biol.* 163:87-95.
- Paul, J., S. Jeyaraj, S.M. Huber, G. Seebohm, C. Bohmer, F. Lang, P.G. Kreamsner, and J.F. Kun. 2007. Alterations in the cytoplasmic domain of CLCN2 result in altered gating kinetics. *Cell. Physiol. Biochem.* 20:441-454.
- Pettersen, E.F., T.D. Goddard, C.C. Huang, G.S. Couch, D.M. Greenblatt, E.C. Meng, and T.E. Ferrin. 2004. UCSF Chimera--a visualization system for exploratory research and analysis. *J Comput Chem.* 25:1605-1612.
- Pintilie, G., K. Zhang, Z. Su, S. Li, M.F. Schmid, and W. Chiu. 2020. Measurement of atom resolvability in cryo-EM maps with Q-scores. *Nat. Methods*. 17:328-334.
- Pusch, M. 2002. Myotonia caused by mutations in the muscle chloride channel gene CLCN1. *Hum. Mutat.* 19:423-434.
- Pusch, M., S. Jordt, V. Stein, and T.J. Jentsch. 1999. Chloride dependence of hyperpolarization-activated chloride channel gates. *J. Physiol.* 515:341-353.
- Roe, D.R., and T.E. Cheatham, 3rd. 2013. PTRAJ and CPPTRAJ: Software for Processing and Analysis of Molecular Dynamics Trajectory Data. *Journal of chemical theory and computation*. 9:3084-3095.
- Saint-Martin, C., G. Gouvain, G. Teodorescu, I. Gourfinkel-An, E. Fedirko, Y.G. Weber, S. Maljevic, J.P. Ernst, J. Garcia-Olivares, C. Fahlke, R. Nabbout, E. LeGuern, H. Lerche, J.C. Poncer, and C. Depienne. 2009. Two novel CLCN2 mutations accelerating chloride channel deactivation are associated with idiopathic generalized epilepsy. *Hum. Mutat.* 30:397-405.
- Salomon-Ferrer, R., A.W. Gotz, D. Poole, S. Le Grand, and R.C. Walker. 2013. Routine Microsecond

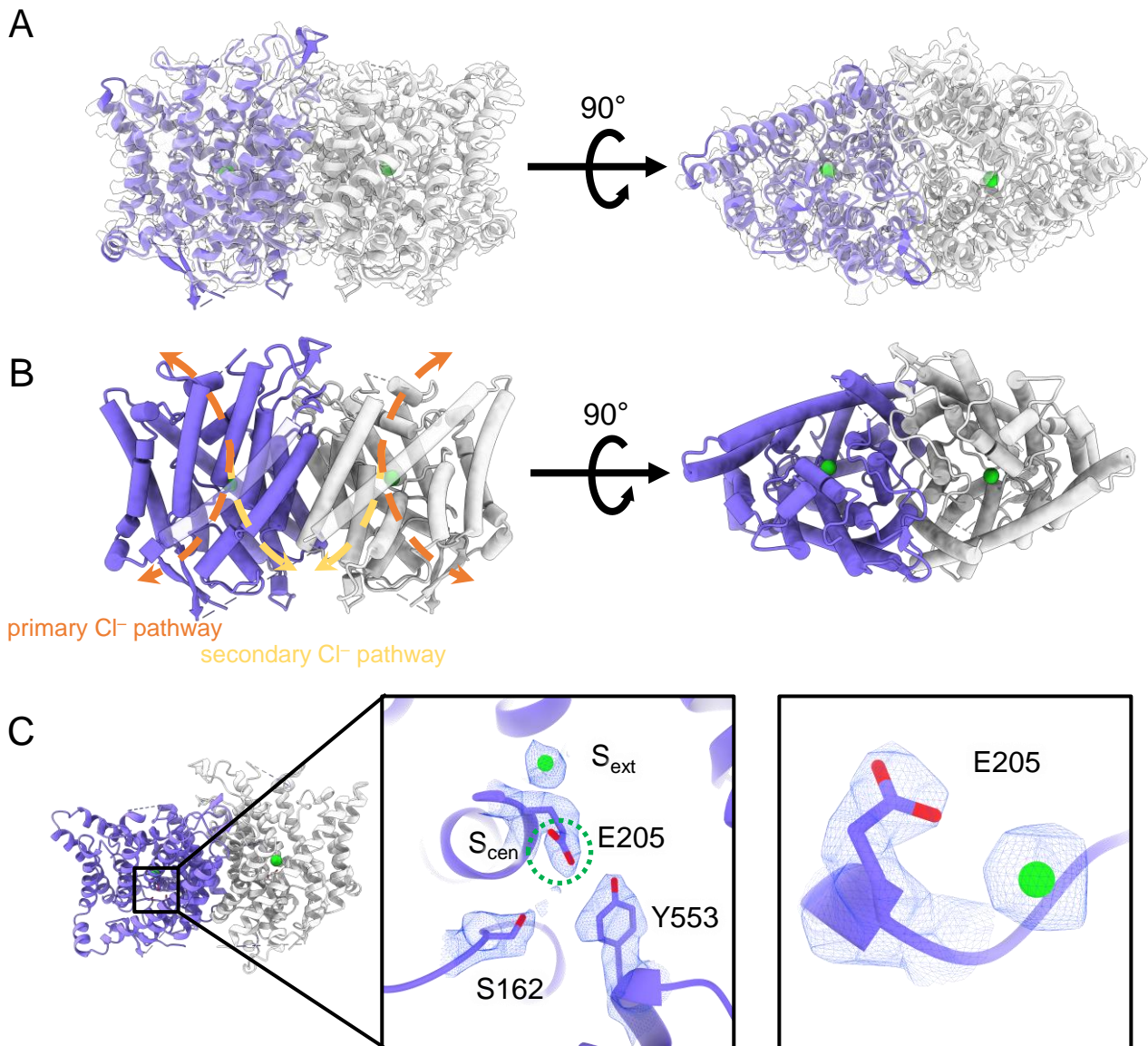
- Molecular Dynamics Simulations with AMBER on GPUs. 2. Explicit Solvent Particle Mesh Ewald. *Journal of chemical theory and computation*. 9:3878-3888.
- Sanchez-Rodriguez, J.E., J.A. De Santiago-Castillo, and J. Arreola. 2010. Permeant anions contribute to voltage dependence of CLC-2 chloride channel by interacting with the protopore gate. *J. Physiol.* 588:2545-2556.
- Sanchez-Rodriguez, J.E., J.A. De Santiago-Castillo, J.A. Contreras-Vite, P.G. Nieto-Delgado, A. Castro-Chong, and J. Arreola. 2012. Sequential interaction of chloride and proton ions with the fast gate steer the voltage-dependent gating in CLC-2 chloride channels. *J. Physiol.* 590:4239-4253.
- Scholl, U.I., G. Stolting, J. Schewe, A. Thiel, H. Tan, C. Nelson-Williams, A.A. Vichot, S.C. Jin, E. Loring, V. Untiet, T. Yoo, J. Choi, S. Xu, A. Wu, M. Kirchner, P. Mertins, L.C. Rump, A.M. Onder, C. Gamble, D. McKenney, R.W. Lash, D.P. Jones, G. Chune, P. Gagliardi, M. Choi, R. Gordon, M. Stowasser, C. Fahlke, and R.P. Lifton. 2018. CLCN2 chloride channel mutations in familial hyperaldosteronism type II. *Nat. Genet.* 50:349-354.
- Schrecker, M., J. Korobenko, and R.K. Hite. 2020. Cryo-EM structure of the lysosomal chloride-proton exchanger CLC-7 in complex with OSTM1. *Elife*. 9.
- Sepela, R.J., and J.T. Sack. 2018. Taming unruly chloride channel inhibitors with rational design. *Proc. Natl. Acad. Sci. U. S. A.* 115:5311-5313.
- Steinmeyer, K., C. Ortland, and T.J. Jentsch. 1991. Primary structure and functional expression of a developmentally regulated skeletal muscle chloride channel. *Nature*. 354:301-304.
- Stolting, G., M. Fischer, and C. Fahlke. 2014a. CLC-1 and CLC-2 form hetero-dimeric channels with novel protopore functions. *Pflugers Arch.* 466:2191-2204.
- Stolting, G., M. Fischer, and C. Fahlke. 2014b. CLC channel function and dysfunction in health and disease. *Front Physiol.* 5:378.
- Stolting, G., G. Teodorescu, B. Begemann, J. Schubert, R. Nabbout, M.R. Toliat, T. Sander, P. Nurnberg, H. Lerche, and C. Fahlke. 2013. Regulation of CLC-2 gating by intracellular ATP. *Pflugers Arch.* 465:1423-1437.
- Suomivuori, C.M., N.R. Latorraca, L.M. Wingler, S. Eismann, M.C. King, A.L.W. Kleinhenz, M.A. Skiba, D.P. Staus, A.C. Kruse, R.J. Lefkowitz, and R.O. Dror. 2020. Molecular mechanism of biased signaling in a prototypical G protein-coupled receptor. *Science*. 367:881-887.
- Thiemann, A., S. Grunder, M. Pusch, and T.J. Jentsch. 1992. A chloride channel widely expressed in epithelial and non-epithelial cells. *Nature*. 356:57-60.
- Varela, D., M.I. Niemeyer, L.P. Cid, and F.V. Sepulveda. 2002. Effect of an N-terminus deletion on voltage-dependent gating of the CLC-2 chloride channel. *J. Physiol.* 544:363-372.
- Wang, H., M. Xu, Q. Kong, P. Sun, F. Yan, W. Tian, and X. Wang. 2017. Research and progress on CLC2 (Review). *Mol Med Rep.* 16:11-22.
- Wang, K., S.S. Preisler, L. Zhang, Y. Cui, J.W. Missel, C. Gronberg, K. Gotfryd, E. Lindahl, M. Andersson, K. Calloe, P.F. Egea, D.A. Klaerke, M. Pusch, P.A. Pedersen, Z.H. Zhou, and P. Gourdon. 2019. Structure of the human CLC-1 chloride channel. *PLoS Biol.* 17:e3000218.
- Xu, P., Z. Chen, J. Ma, Y. Shan, Y. Wang, B. Xie, D. Zheng, F. Guo, X. Song, G. Gao, K. Ye, Y. Liu, G. Pan, B. Jiang, F. Peng, and X. Zhong. 2023. Biallelic CLCN2 mutations cause retinal degeneration by impairing retinal pigment epithelium phagocytosis and chloride channel function. *Hum. Genet.* 142:577-593.
- Yamada, T., M. Krzeminski, Z. Bozoky, J.D. Forman-Kay, and K. Strange. 2016. Role of CBS and Bateman Domains in Phosphorylation-Dependent Regulation of a CLC Anion Channel. *Biophys. J.* 111:1876-1886.



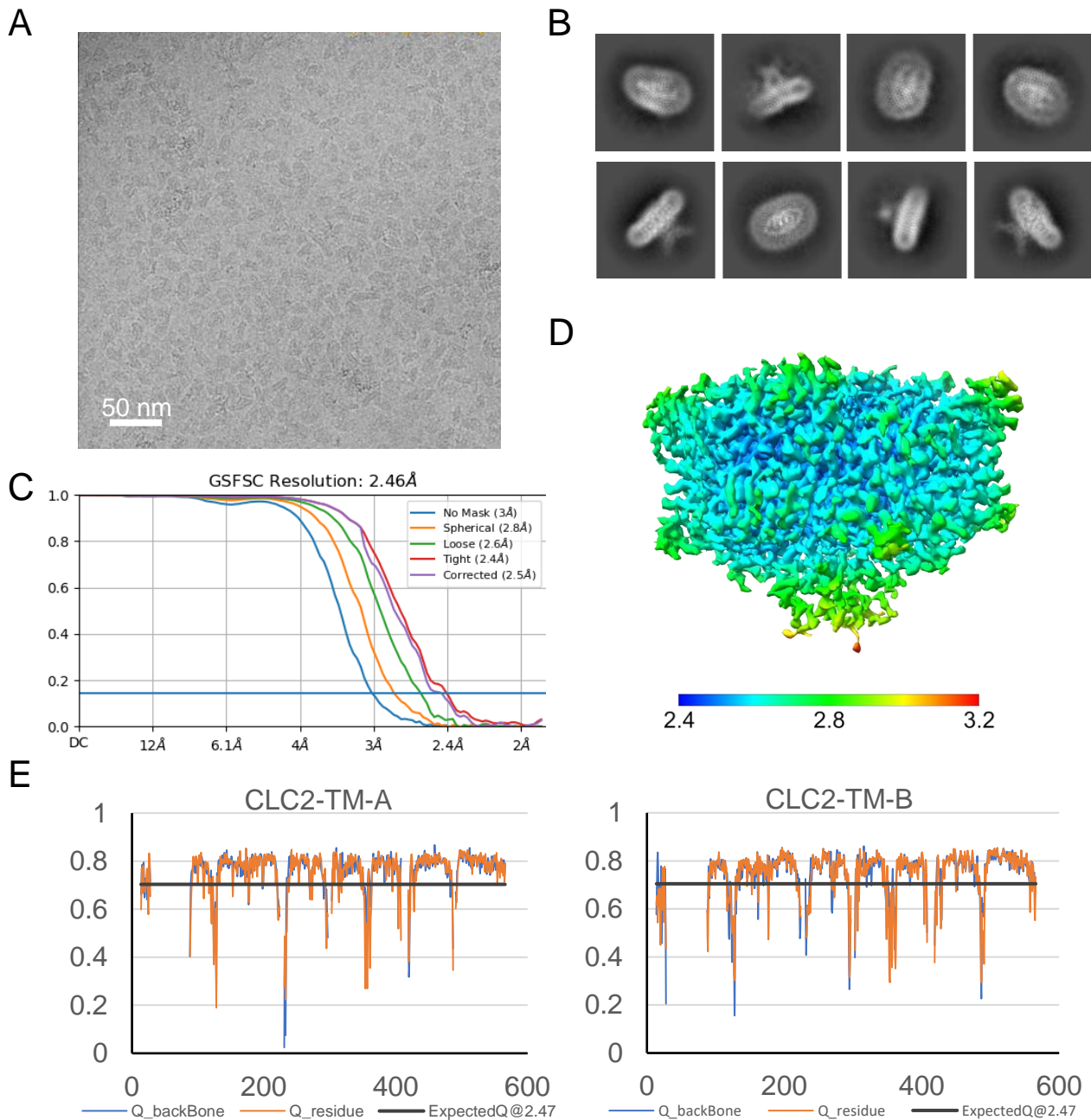
- Yusef, Y.R., L. Zuniga, M. Catalan, M.I. Niemeyer, L.P. Cid, and F.V. Sepulveda. 2006. Removal of gating in voltage-dependent CLC-2 chloride channel by point mutations affecting the pore and C-terminus CBS-2 domain. *J. Physiol.* 572:173-181.
- Zagotta, W.N., T. Hoshi, and R.W. Aldrich. 1990. Restoration of inactivation in mutants of Shaker potassium channels by a peptide derived from ShB [see comments]. *Science.* 250:568-571.
- Zifarelli, G. 2022. The Role of the Lysosomal Cl(-)/H(+) Antiporter CLC-7 in Osteopetrosis and Neurodegeneration. *Cells.* 11.
- Zifarelli, G., and M. Pusch. 2007. CLC chloride channels and transporters: a biophysical and physiological perspective. *Rev. Physiol. Biochem. Pharmacol.* 158:23-76.
- Zuniga, L., M.I. Niemeyer, D. Varela, M. Catalan, L.P. Cid, and F.V. Sepulveda. 2004. The voltage-dependent CLC-2 chloride channel has a dual gating mechanism. *J. Physiol.* 555:671-682.



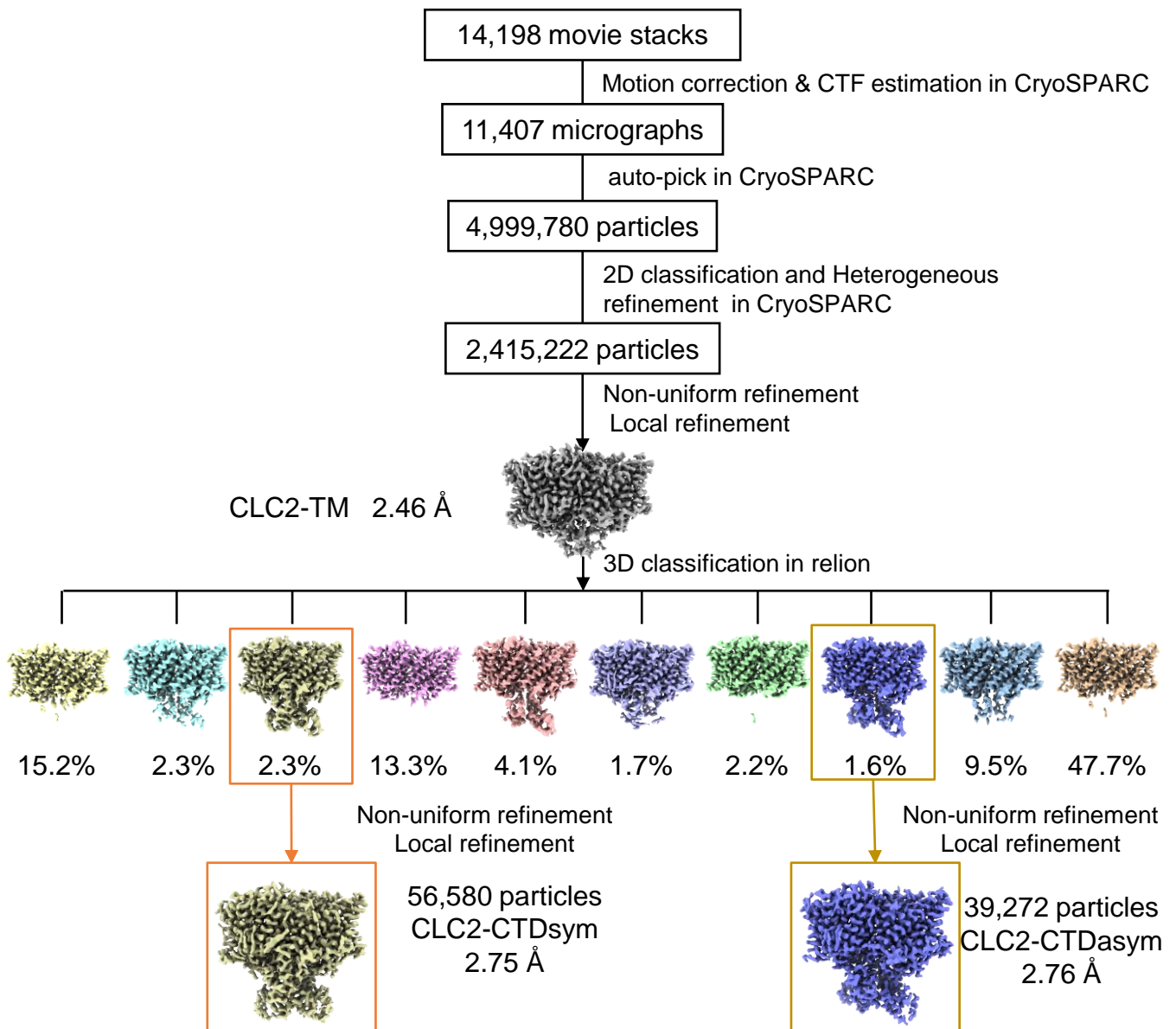
**Figure 1. Gating conformations in CLC transporters and channels.** (A) Cartoon depictions of the CLC anion-permeation pathway. The “gating glutamate” ( $E_{gate}$ ) can occupy anion binding sites within the permeation pathway (“down” and “middle” conformations, occupying the central ( $S_{cen}$ ) and external ( $S_{ext}$ ) anion-binding sites respectively) or away from these sites (“up” and “out” conformations). Coupling of  $E_{gate}$  movement to  $Cl^-/H^+$  binding/unbinding and global conformational change generates 2:1  $Cl^-/H^+$  exchange. (B)  $E_{gate}$  is required for voltage-dependent gating in CLC channels but has been observed structurally only in CLC-1 (PDB ID: 6coy), in the “out” position. In contrast to CLC-1, which is predominantly open at zero mV, CLC-2 is predominantly closed. The open probability ( $P_o$ ) versus voltage ( $V$ ) traces are based on published data reported for CLC-1 (Lisal and Maduke, 2008) and CLC-2 (Stolting et al., 2013).



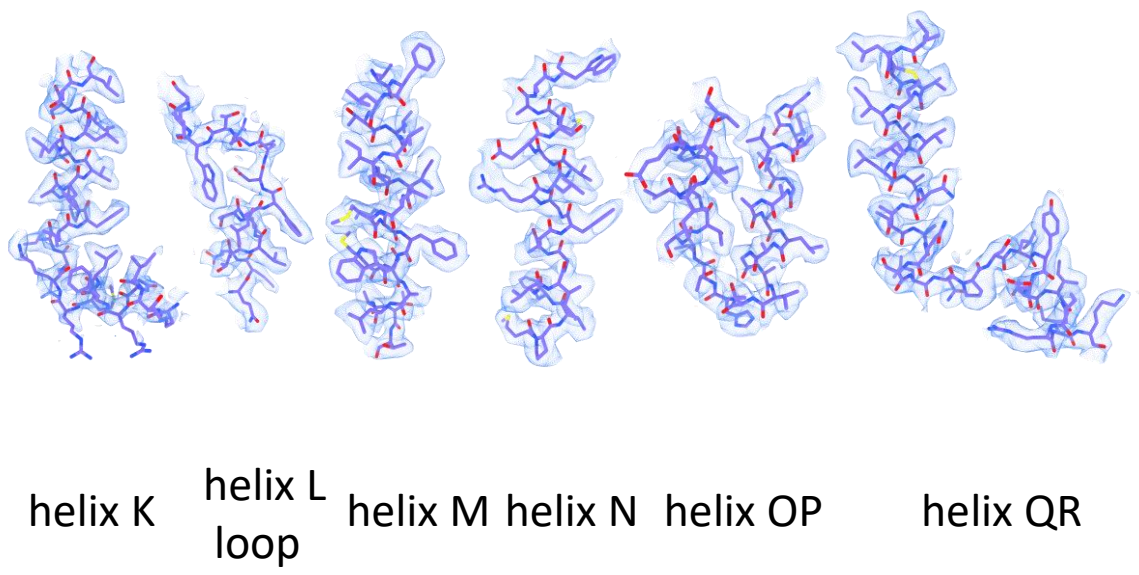
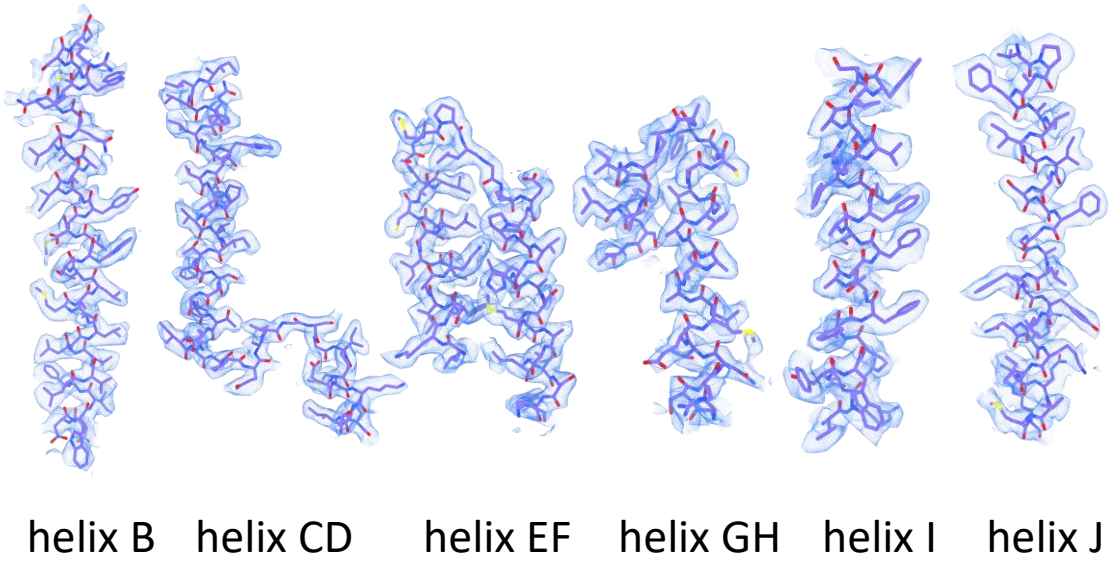
**Figure 2. CryoEM structure of the human CLC-2 channel.** Overall structure of the transmembrane domain (“CLC2-TM”) at 2.46 Å. The identical subunits of the homodimer are shown in purple and gray, Cl<sup>-</sup> ions are shown as green balls. **(A)** cryoEM density map with model overlay and **(B)** model only with dashed arrows indicating the locations of pathways detected by Cover: orange, primary Cl<sup>-</sup> pathway common to all CLCs; yellow, secondary Cl<sup>-</sup> pathway detected in CLC-2 and CLC-1. Details of the pathways are presented in Figure 3. The secondary pathway, whose function is not yet known, was so named when first observed in the CLC-1 structure (Park and MacKinnon, 2018). **(C)** Zoomed-in views showing cryoEM density overlay of bound Cl<sup>-</sup> and key residues – E<sub>gate</sub> (E205) and inner-gate residues Ser<sub>C</sub> (S162) and Tyr<sub>C</sub> (Y553). S<sub>cen</sub> is indicated with a green dashed circle.



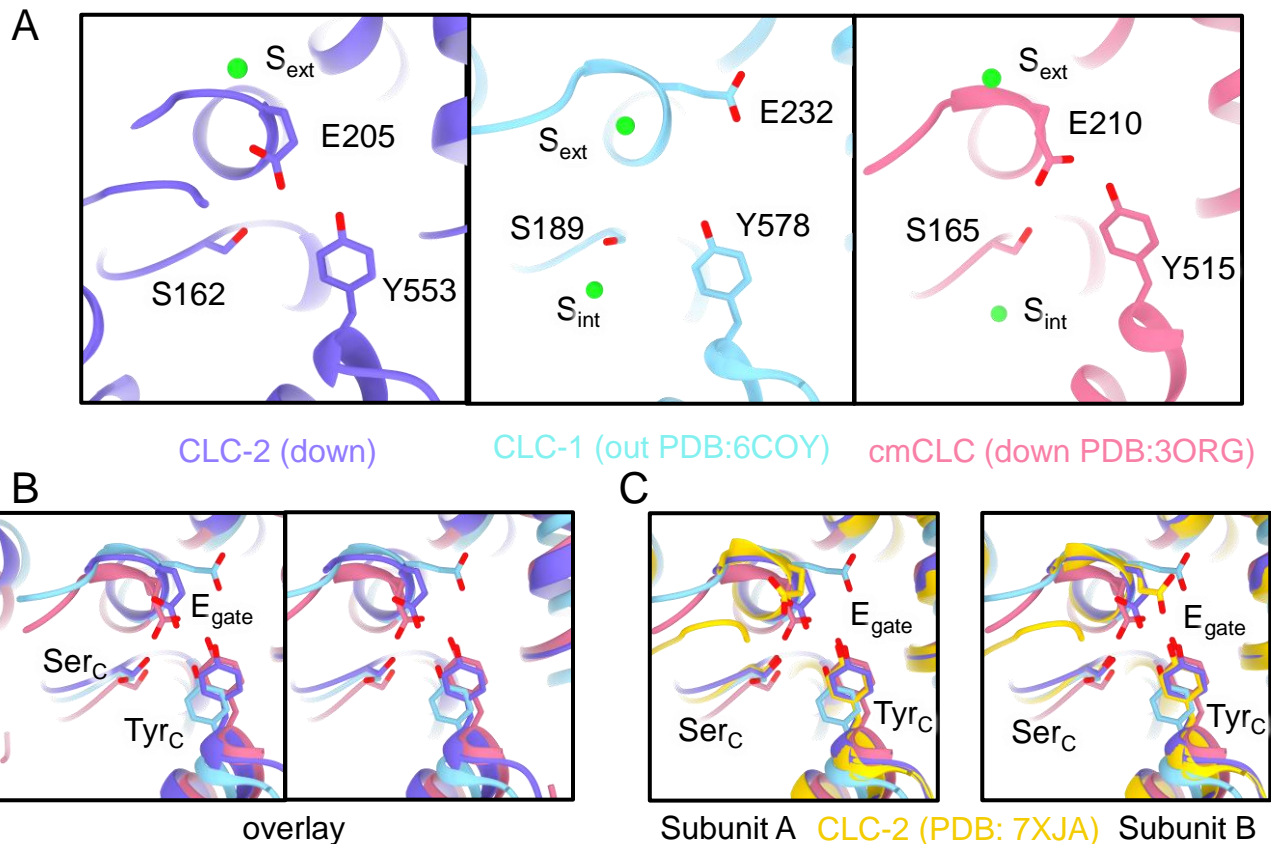
**Figure 2 - figure supplement 1. Micrograph and 2D classes and structure validation of CLC2-TM.** (A) Representative motion-corrected cryo-EM micrograph. (B) 2D class averages. (C) Gold standard FSC plots calculated in cryoSPARC. (D) Local resolution of the cryo-EM map of the CLC2-TM. (E) Model validation using Q-scores (Pintilie et al., 2020) of subunit A (left) and subunit B (right). The black line represents the expected Q-score at respective resolution based on the correlation between Q-scores and map resolution.



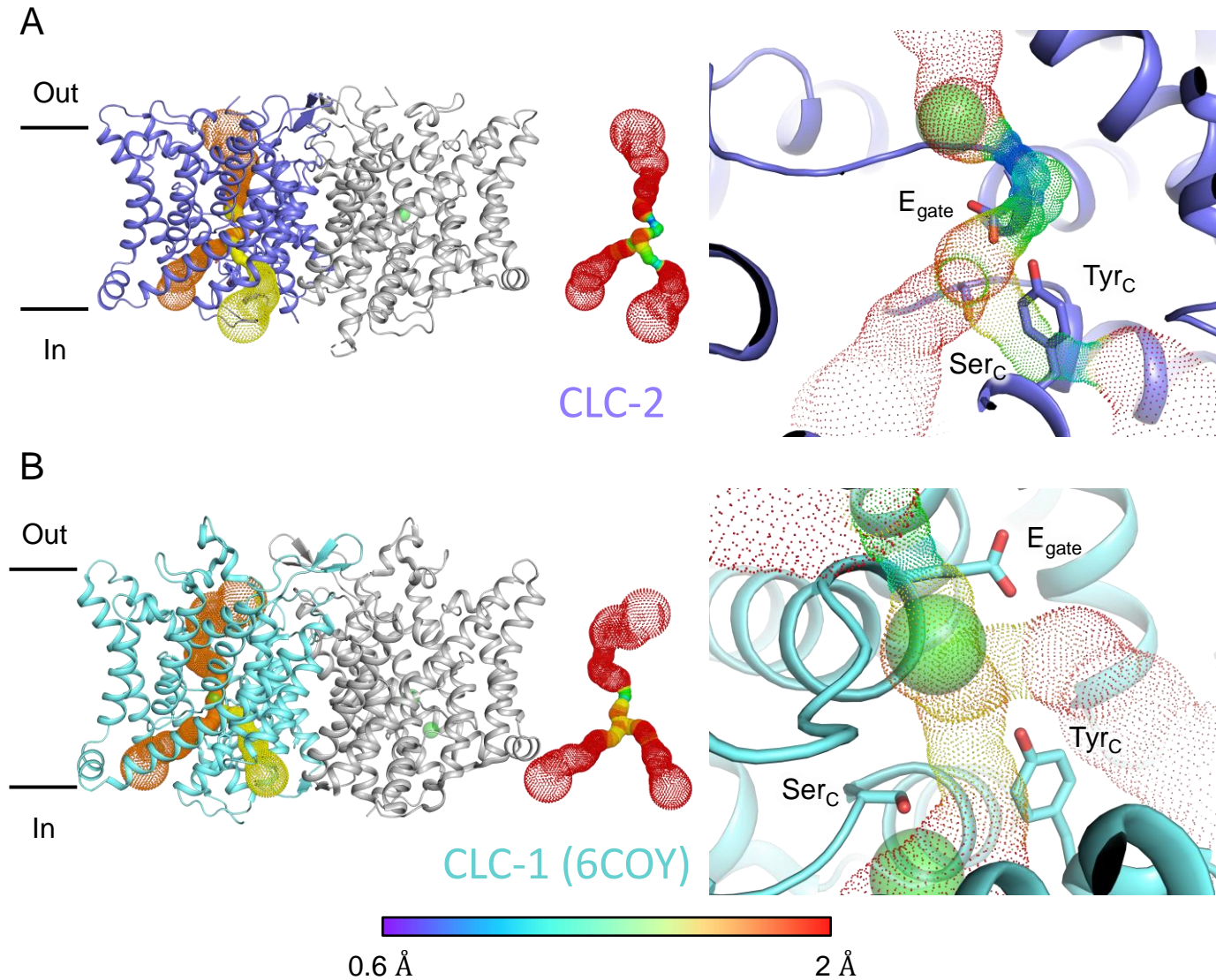
**Figure 2 - figure supplement 2. CryoEM workflow of the CLC2 single-particle cryoEM data processing.** A total of 14,198 movie stacks were collected on a 300 kV Titan Krios cryo-electron microscope. cryoSPARC was used for 2D classification, and the CLC2-TM density map was obtained after 2D classification. Relion was used for 3D classification and yielded two conformations differing in the CTD: CLC2-CTD<sub>sym</sub> and CLC2-CTD<sub>asym</sub>. Resolutions shown refer to the whole protein molecule.



**Figure 2 - figure supplement 3. Helix map of CLC2-TM.** cryo-EM densities and model of CLC-2 transmembrane helices.

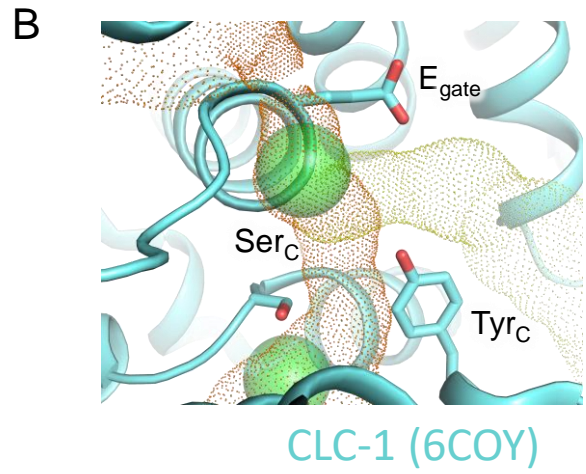
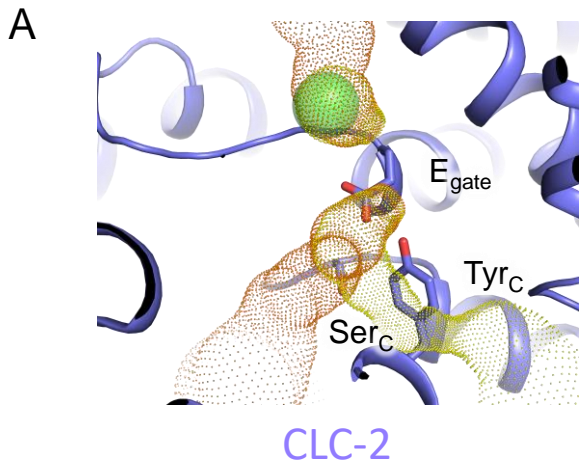


**Figure 2 - figure supplement 4.  $E_{\text{gate}}$  position and  $\text{Cl}^-$  binding sites ( $S_{\text{ext}}$  and  $S_{\text{cen}}$ ).** (A) Comparison between CLC-2 (purple), CLC-1 (light blue), and cmCLC (salmon pink).  $E_{\text{gate}}$  (E205 in CLC-2, E232 in CLC-1, and E210 in cmCLC),  $\text{Ser}_C$  (S162 in CLC2, S189 in CLC-1, and S165 in cmCLC) and  $\text{Tyr}_C$  (Y553 in CLC-2, Y578 in CLC-1, and Y515 in cmCLC) are shown as sticks. In CLC-2 and cmCLC,  $S_{\text{ext}}$  is occupied by  $\text{Cl}^-$ , and  $S_{\text{cen}}$  is occupied by  $E_{\text{gate}}$ .  $E_{\text{gate}}$  is in the “down” position. In CLC-1,  $S_{\text{ext}}$  is occupied by  $\text{Cl}^-$ , and  $S_{\text{cen}}$  lacks anion density.  $E_{\text{gate}}$  is in the “out” position, away from the  $\text{Cl}^-$ -permeation pathway. (B) Overlay view (stereo) of panel A. (C) Overlay with the CLC-2  $E_{\text{gate}}$  conformations modeled in PDB ID: 7XJA (Ma et al., 2023).

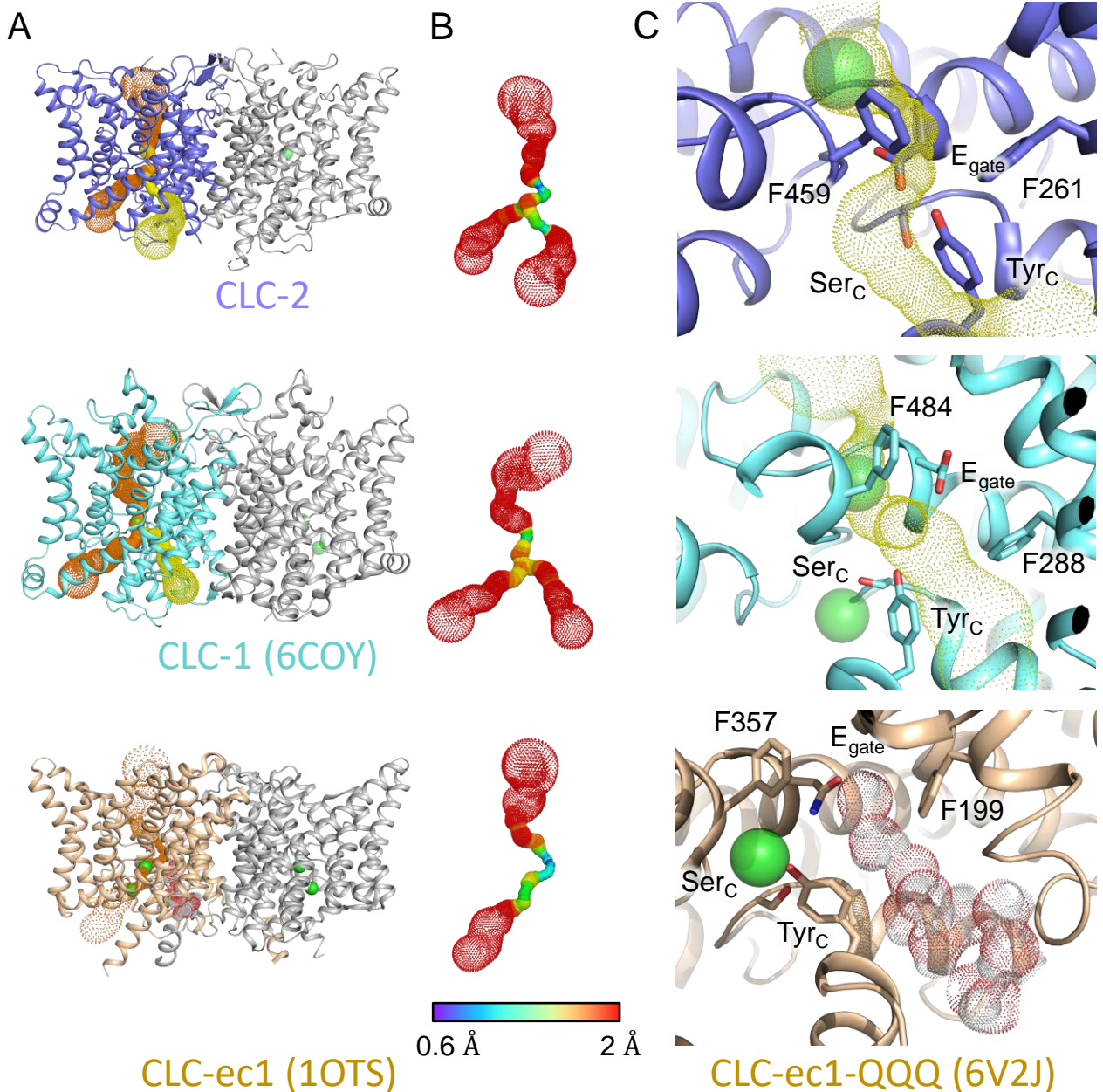


**Figure 3** Pore profile detected in CLC-2. **(A)** Left: The primary (orange) and secondary (yellow) pore detected in CLC-2 using Caver. Middle: The detected pore radii are displayed in dots as a color map. Right: Zoomed-in view of the restricted (narrowest) site of the pore profile, using the same coloring as in the middle panel.  $E_{gate}$ ,  $Ser_C$  and  $Tyr_C$  are shown as sticks. **(B)** Pore profile for CLC-1 (PDB ID:6coy), with display as in panel **A**.

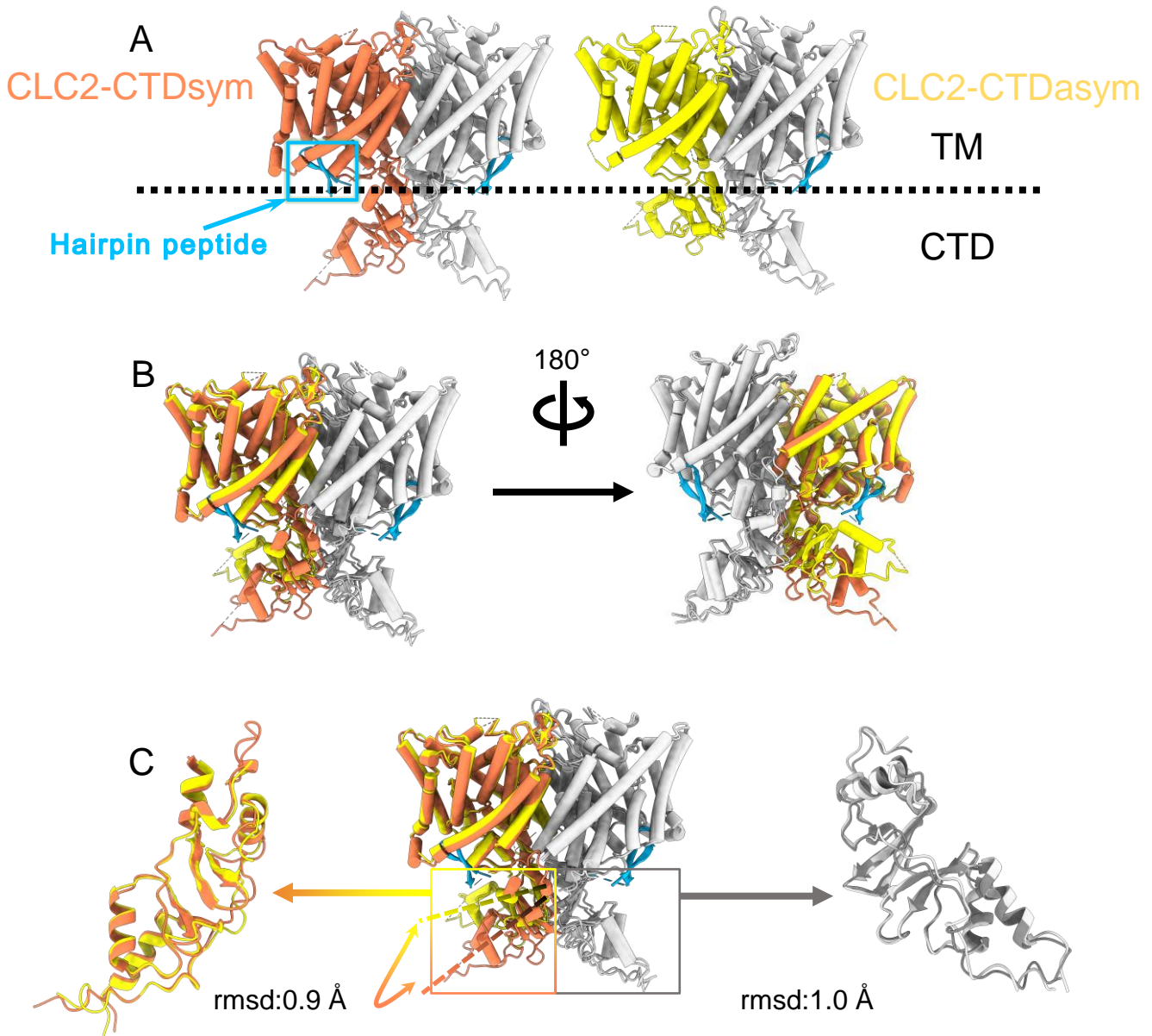




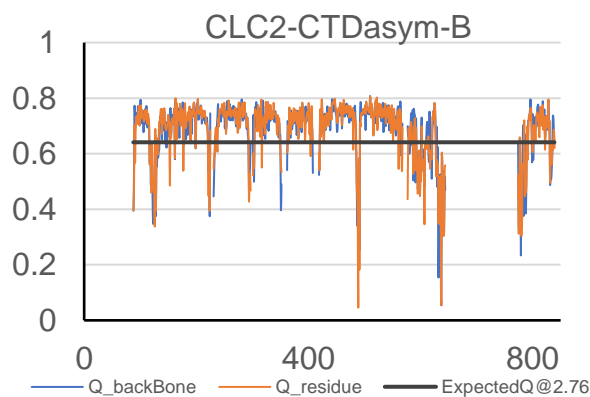
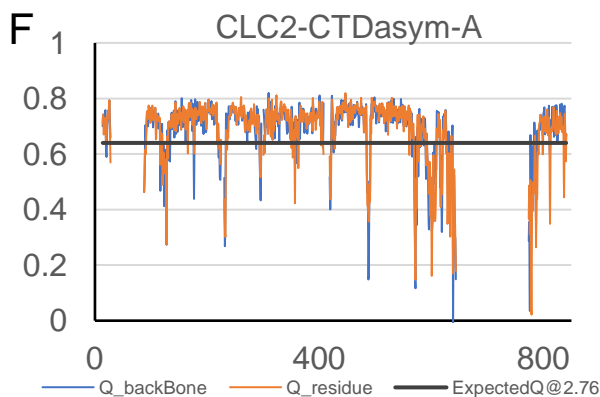
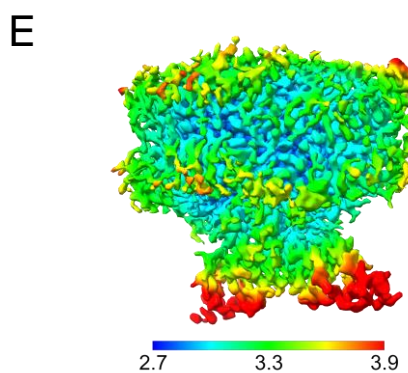
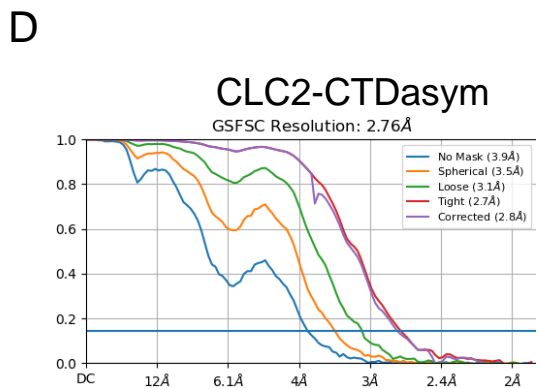
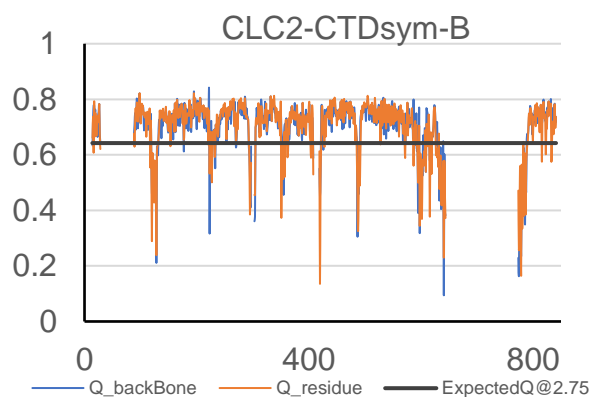
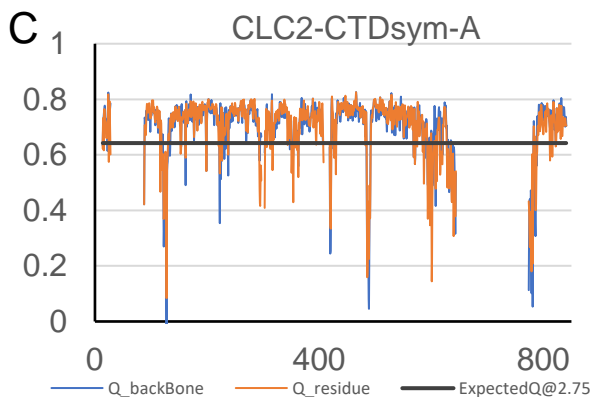
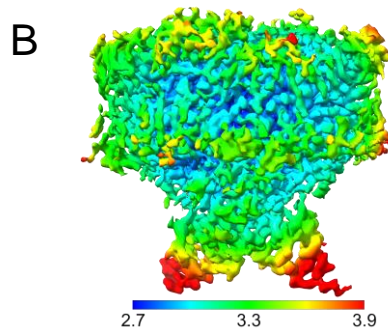
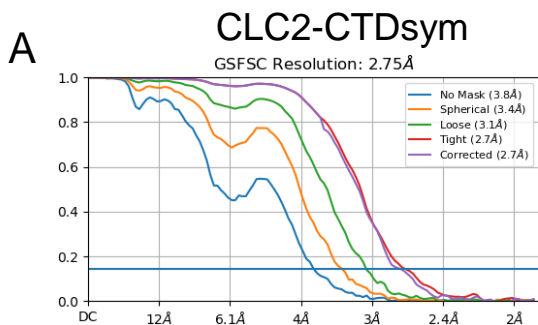
**Figure 3 - figure supplement 1. Cl<sup>-</sup> pathway in CLC-2 and CLC-1.** (A) CLC-2 Cl<sup>-</sup> pathway as shown in Figure 3 but omitting sections with pore radius less than 1Å. E<sub>gate</sub>, occupying the S<sub>cen</sub> site, blocks the canonical Cl<sup>-</sup> pathway. (B) same as panel A, for CLC-1 (PDB ID:6coy).



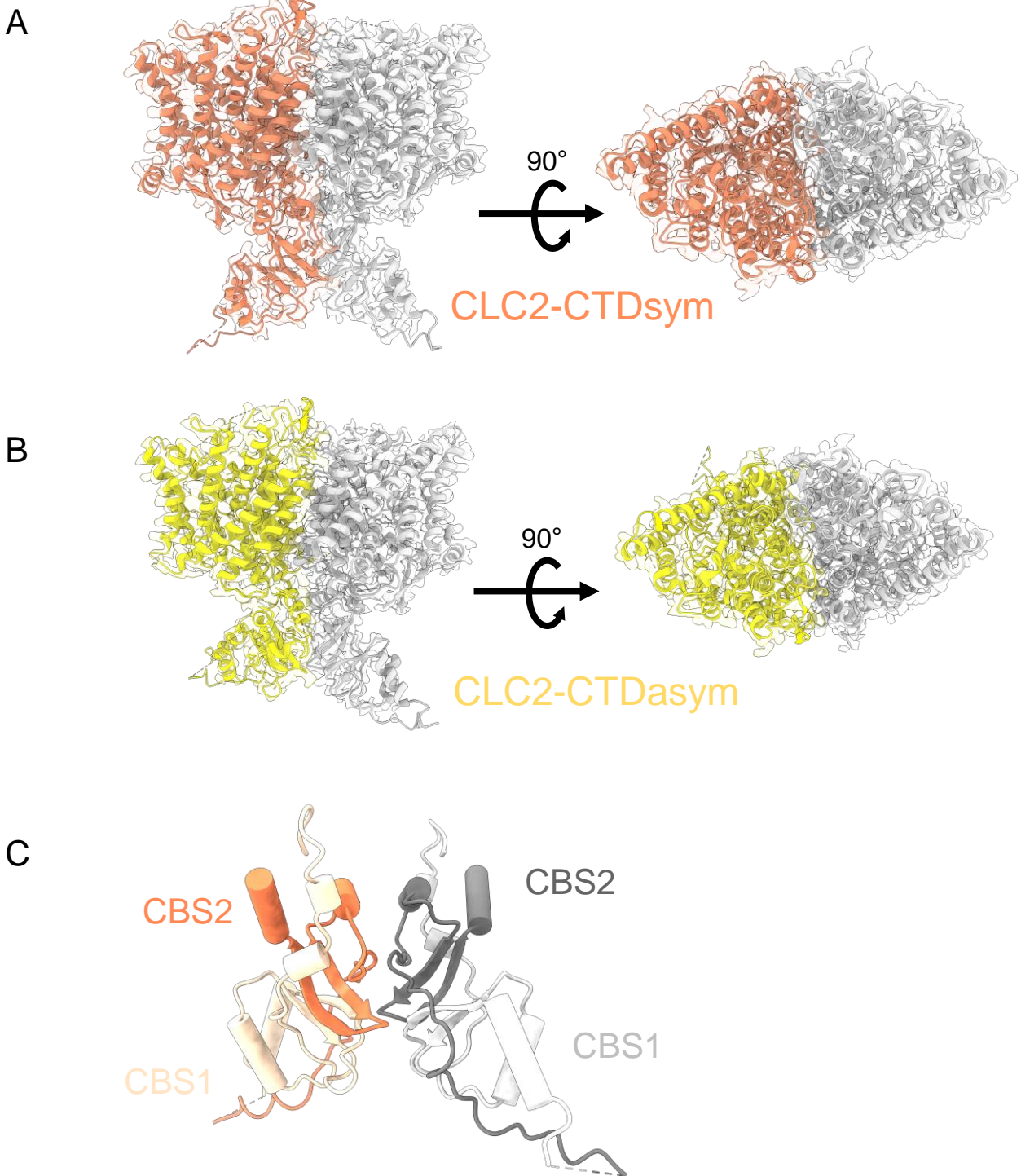
**Figure 3 - figure supplement 2. Comparison of primary and secondary Cl<sup>-</sup> pathways with transporter Cl<sup>-</sup> and H<sup>+</sup> pathways.** (A) The top two panels are repeated from Figure 3A, indicating the primary (orange) and secondary (yellow) cover-detected pores in CLC-1 and CLC-2. The lower panel shows CLC-ec1 (PDB ID: 1OTS), a representative for the CLC transporters, where cover detects only the primary pore (orange dots as for CLC-1 and CLC-2). (B) Detected pore radii show a longer constriction in the CLC-ec1 transporter compared to the CLC-1 and CLC-2 channels. (C) Zoomed-in view of the secondary-pore region for CLC-2 (top), CLC-1 (middle) and CLC-ec1 (bottom). The CLC-ec1 panel shows water wires detected in simulations of the QQQ mutant structure (PDB ID: 6V2J) (Chavan et al., 2020), with oxygen in red dots and hydrogen in white dots.



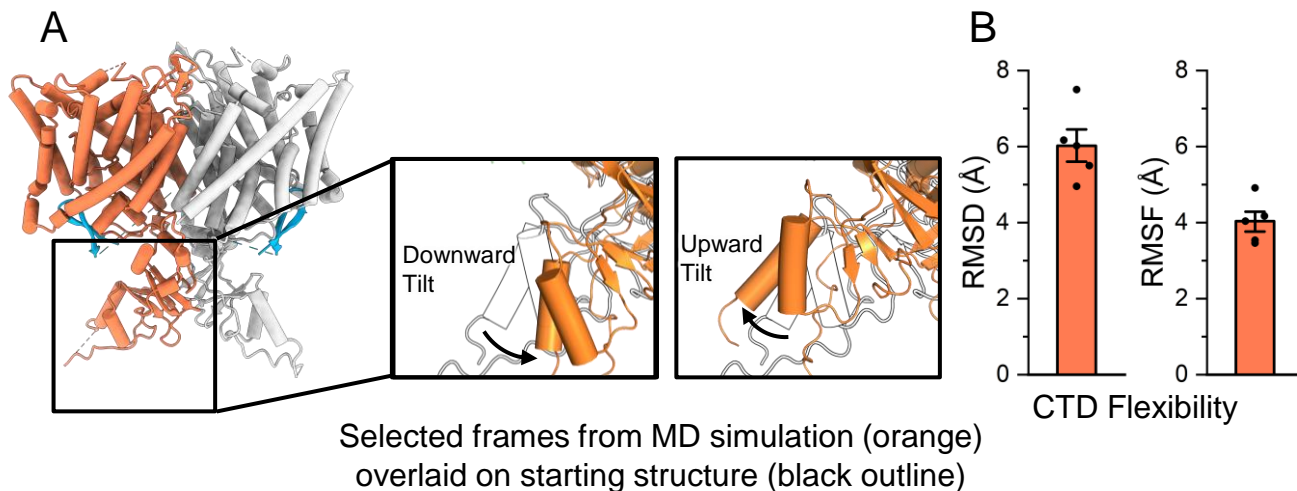
**Figure 4. Different conformations of the CTD.** (A). Overall structure of the two CLC-2 conformations. Left: CLC2-CTD<sub>sym</sub> at 2.75 Å. Right: CLC2-CTD<sub>asym</sub> at 2.76 Å. The subunits of the homodimer are shown in orange (CLC2-CTD<sub>sym</sub>) or yellow (CLC2-CTD<sub>asym</sub>) and gray (for both). The subunits adopting different CTD conformations are shown in orange and yellow, while the subunits sharing the same CTD conformation are shown in gray. The dashed line demarcates the transmembrane (TM) and cytoplasmic (CTD) domains. A hairpin structure detected at the intracellular pore is shown in blue. (B) Overlay of two conformations. (C) Hinge movement of the CTD between two conformations. The middle panel shows an overlay of CLC2-CTD<sub>sym</sub> (orange and gray) and CLC1-CTD<sub>asym</sub> (yellow and gray), with the CTDs highlighted in boxes. For the subunits that adopt different conformations (orange and yellow), the double-headed arrow indicates the change between the two conformations. The RMSD between the subunits shown in orange/yellow is 6.9 Å, while the RMSD for the subunits shown in gray is only 1.3 Å. Alignments of only the CTDs are shown at left and right; in these alignments, the low RMSD values (0.9 Å and 1.0 Å, respectively) indicate that the CTDs undergo a hinge movement.



**Figure 4 - figure supplement 1. Structure validation of CLC2-CTDsym and CLC2-CTDasym.** (A) Gold standard FSC plots calculated in cryoSPARC for CLC2-CTDsym. (B) Local resolution of the cryo-EM map of the CLC2-CTDsym. (C) Model validation using Q-scores of subunit A (left) and subunit B (right) of CLC2-CTDsym. The black line represents the expected Q-score at respective resolution based on the correlation between Q-scores and map resolution. (D-F) the same as (A-C) for CLC2-CTDasym.

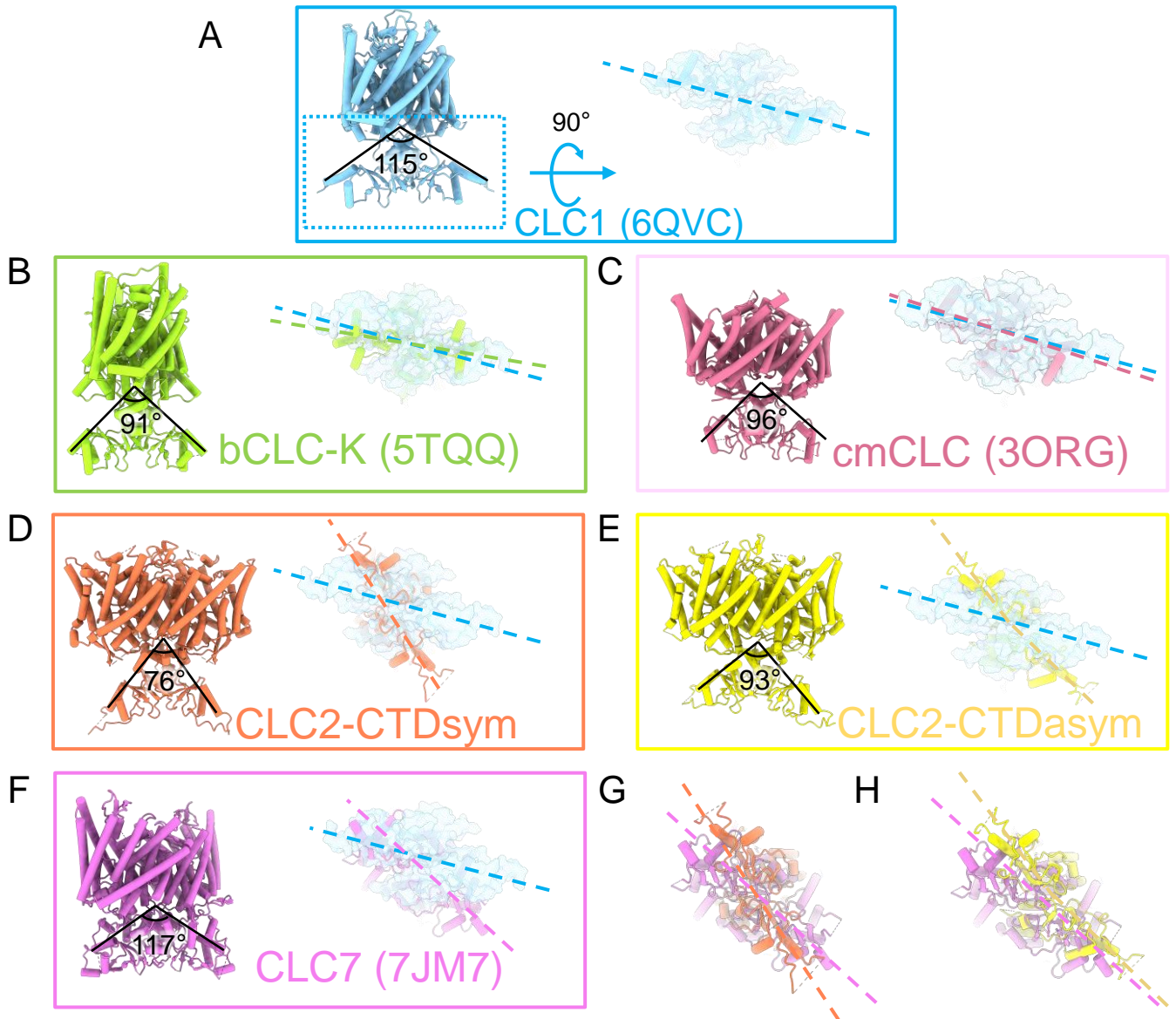


**Figure 4 – figure supplement 2. CryoEM density maps for the two CTD-containing CLC-2 conformations, overlaid with structural models. (A) CLC2-CTD<sub>sym</sub>. (B) CLC2-CTD<sub>asym</sub>. Side view (left) and top view (right) are shown. (C) CTD of CLC2-CTD<sub>sym</sub> shows two CBS domains on each subunit (orange and light orange for subunit A; gray and light gray for subunit B).**

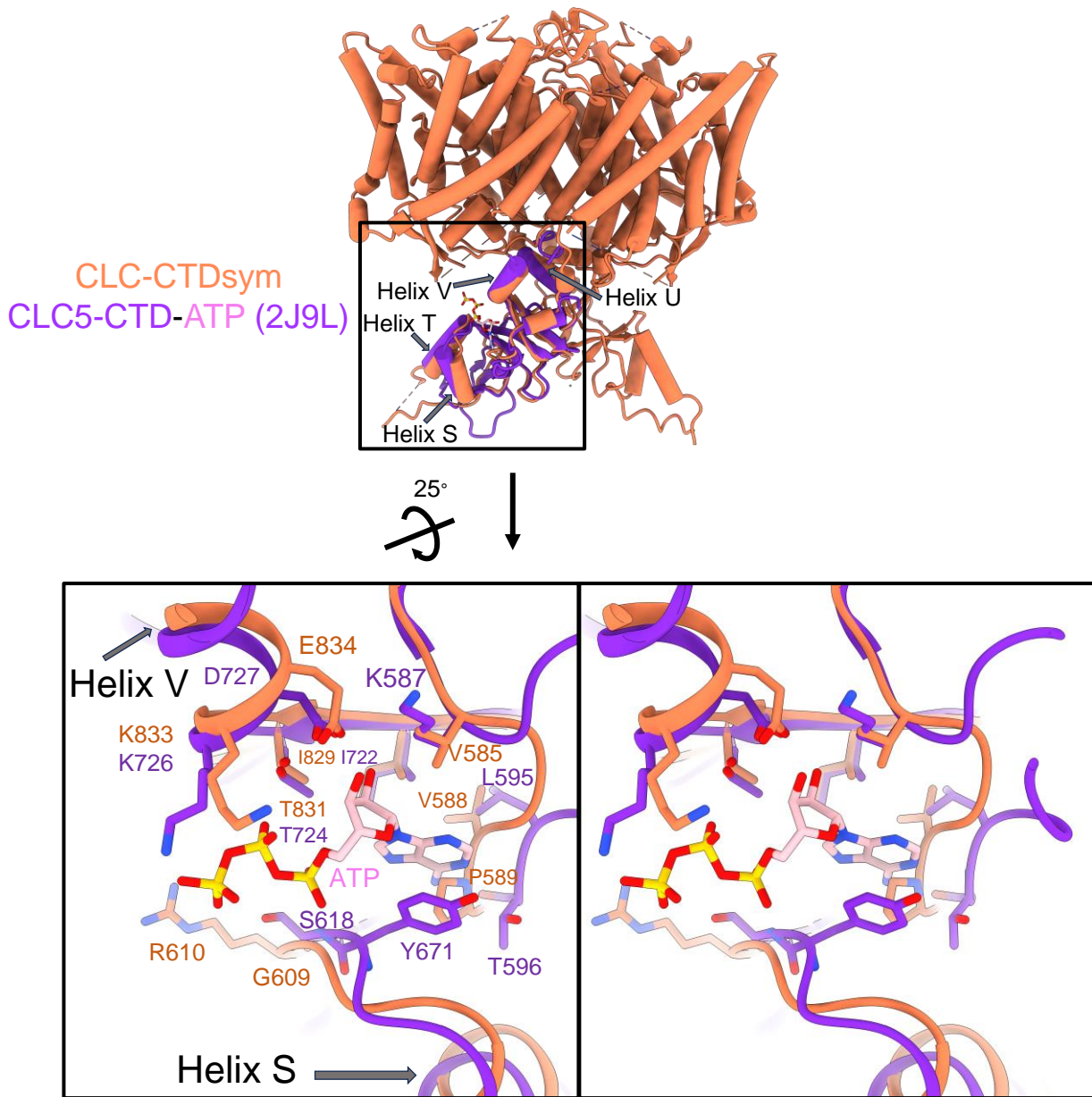


**Figure 4 - figure supplement 3. MD analysis indicates conformational flexibility of the CTD.**

(A) The CTD is highly mobile relative to the transmembrane domain, and often tilts upward or downward relative to its initial location. In the inset images, two representative frames from simulation are shown (orange) overlaid on the starting structure (black outline). (B) The RMSD (root mean square deviation) and RMSF (root mean square fluctuation) of the cytoplasmic domain backbone were calculated after aligning frames on the transmembrane domains. Bars show the mean of five independent simulations, each 2.0  $\mu$ s in length. Error bars are 68% confidence intervals of the mean.

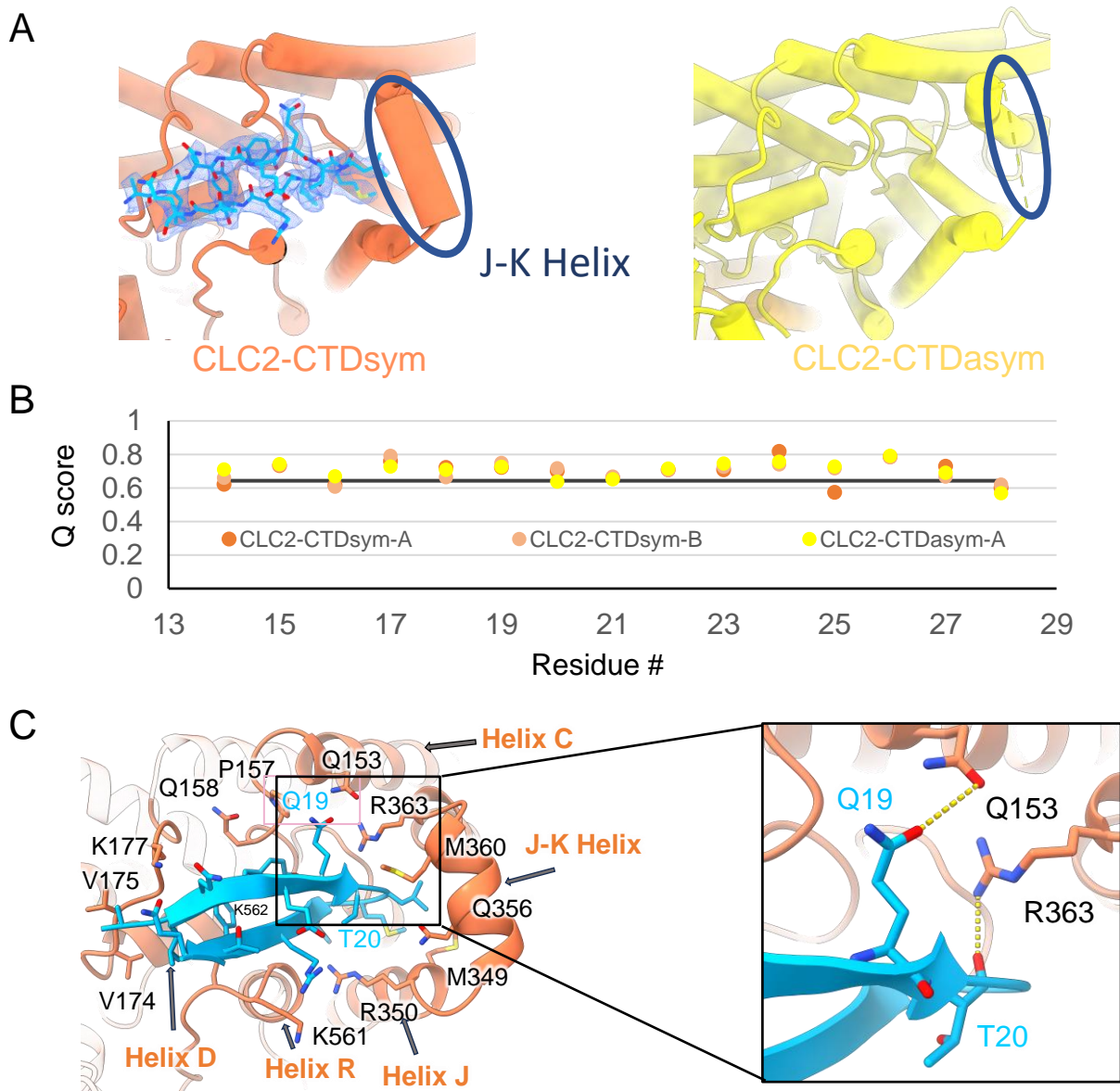


**Figure 4 - figure supplement 4. Comparison of CTD orientation with respect to the TM domain.** (A) The CLC-1 structure is shown in light blue. The angle of orientation for the CTDs was calculated using the far end residue of helix T (the second helix of first CBS domain) as the end point of rays and the center of the TM-CTD connecting plane as the vertex of the angle. On the right the CTD is shown in surface representation following rotation as indicated. Panels (B) – (F) show the CLC homolog indicated, with angles calculated as for CLC-1, and the rotated view of the CTD shown to compare the positioning of the CTDs relative to the membrane domains. The dashed lines indicate the long axes of the CTDs. In each panel, CLC-1 is shown in light blue as a reference for comparison. (G) and (H) overlays compare the CTD orientations in the CLC-2 structures to that in CLC-7. PDB IDs are shown in the parentheses. PDB IDs for CLC2-CTD<sub>sym</sub> and CLC2-CTD<sub>asym</sub> are 8TA4 and 8TA5.



**Figure 4 – figure supplement 5. ATP binding site comparison between CLC-2 and CLC-5.** Top: Structural overlay of CLC2-CTD<sub>sym</sub> (in orange) and CLC5-CTD (in dark purple) with ATP (pink carbon atoms; CPK coloring on non-carbon atoms. PDB ID: 2J9L). Bottom: Zoomed in stereo view of ATP binding site in CLC5-CTD (dark purple) overlaid with the same region in CLC2-CTD<sub>sym</sub> (orange). Residue numbers are labeled in dark purple for CLC-5 and orange for CLC-2.





**Figure 5. The blocking hairpin structure corresponds to an N-terminal sequence of CLC-2.** (A) *Left:* The hairpin structure seen in the cryoEM density (blue mesh) fits N-terminal residues 14-28 (blue). *Right:* The subunit in CLC2-CTDasym structure that contains a CTD with rotated orientation lacks density for the hairpin structure. In this structure, the residues linking TM helices J and K are not resolved. The dark blue circles indicate this unresolved region (right panel) and the corresponding resolved J-K helix that occurs in the other subunits. (B) Model validation using Q-scores for the N-terminal hairpin: orange and light orange for subunits A & B of CLC2-CTDsym subunit; yellow for subunit A (the hairpin-containing subunit) of CLC2-CTDasym. The black line represents the expected Q-score at 2.75 Å based on the correlation between Q-scores and map resolution. (C) Residues on the transmembrane domain interact with the N-terminal hairpin. The J-K helical linker and TM Helices C, D, R, and J are labeled with arrows. Inset: Zoomed-in view of two hydrogen bonds formed between the hairpin structure and the TM domain: Q19-Q153 and T20-R363. Mutation of these two residues (Q25 and T26 in rat CLC-2) generated an open-channel phenotype for CLC-2 expressed in *Xenopus* oocytes (Grunder et al., 1992).

A

	20	30	40	50
CLC2_HUMAN	EPRALQYEQTLMYGRYTQDLGAFAKEEARIRLGGPEPWKGPSPSRAA			
CLC2_RAT	EPRALQYEQTLMYGRYTQELGAFAKEEARIRLGGPEPWKGSPSARAT			
CLC2_MOUSE	EPRALQYEQTLMYGRYTQELGAFAKEEARIRLGGPEPWKGSPSARAT			
CLC2_RABBIT	EPRALQYEQTLMYGRYTQDLGAFAKEEARIRLGGPEPWRSPPSPRTP			
CLC2_CAVPO	EPRALQYEQTLMYGRYTQELGAFAKEEARIRLGGPEPWKGPSPRPVP			
CLC2_BOVIN	EPRALQYEQTLMYGRYTQDLGAFAKEEARIRLGGPEPWKGPSPRAP			
CLC2_DROME	DDDPICYIDTLMYGRYTKDLGELFAKDEARKLKI LEKRRK. QEDKQRN			

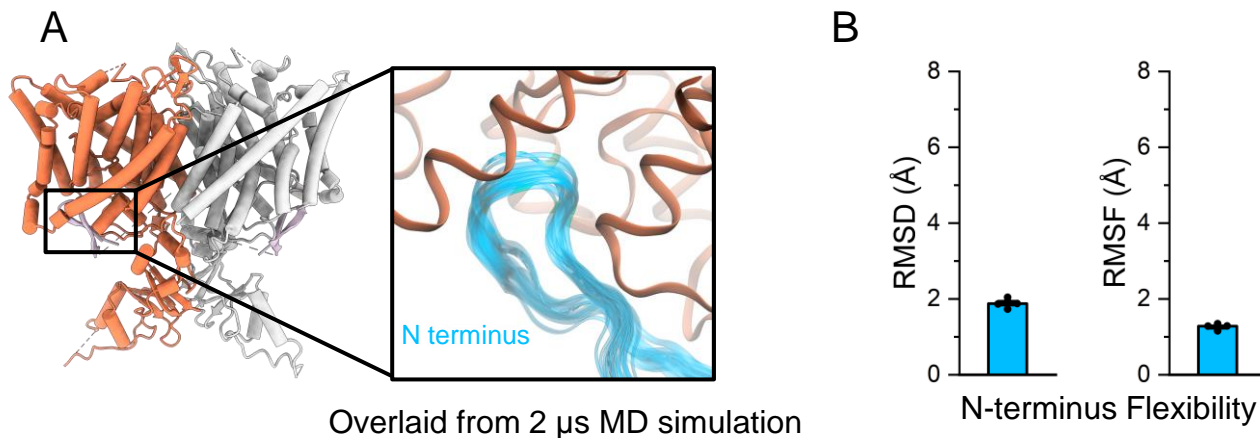
B

	10	20	30
CLC2_HUMAN	AAEEGMEPF	A.....LQYEQTLMYGRYTQD.....	L.....GAFAKE
CLC1_HUMAN	SENGGLQHR	LRKDGAPRHN	VHPTQIYGHKEQ.....FSDR
CLCKA_HUMAN	.....	.....	.....ME
CLCKB_HUMAN	.....	.....	.....ME
CLC0_TORPEDO	.....	.....MSHEKNE.....	.....
CLC3_HUMAN	FQTSEDDNLLD	GDGTAVGTHY..	TMINGGSINS.....
CLC4_HUMAN	.....	.....MVNAGAMSG.....	.....
CLC5_HUMAN	FSMRDDVPPLD	REVGEDK.....	SYNGGGIGS.....
CLC6_HUMAN	.....	.....MAGC.....	.....RGS LCCCCRWCC
CLC7_HUMAN	RDDEEAAPLLRR	TARPGGT..	PLLNAGAPGAARQSPRSALFRVGHMSSV

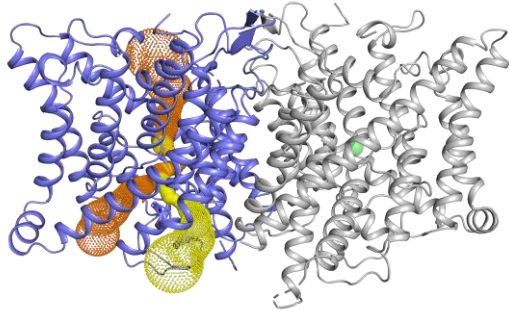
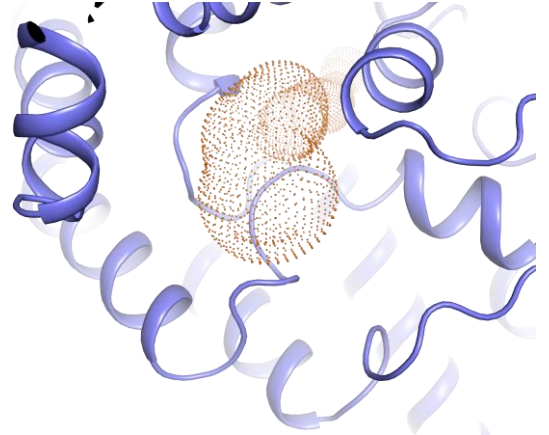
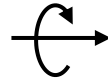
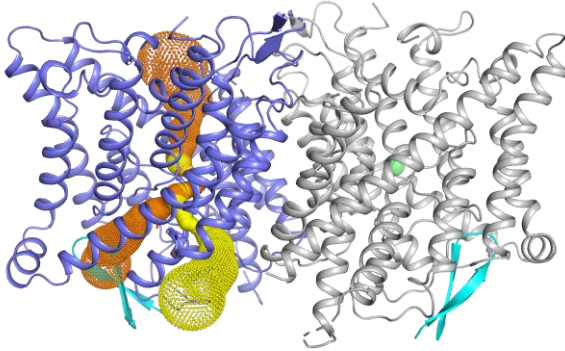
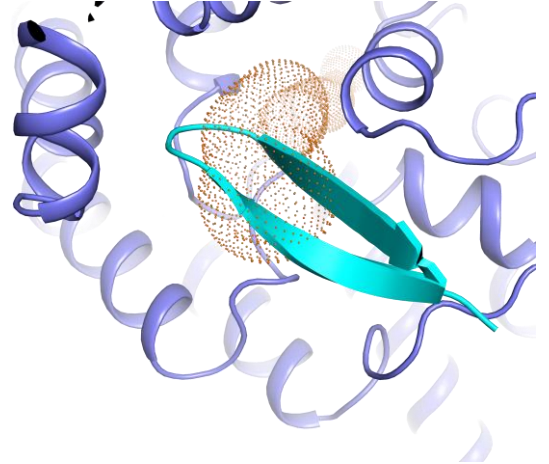
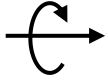
  

	40	50	60	70
CLC2_HUMAN	EAARIRLGGP..EPW..KGPPSSRAAPELLEYGRSRCARCRVC.....			
CLC1_HUMAN	E...QDI GMPKKTGS.....SST...V.DSKDEDHYSKCQDC.....			
CLCKA_HUMAN	E...LVGLR..EGF..SGDPVT.....L...QELWGPCPHIRR.....			
CLCKB_HUMAN	E...FVGLR..EGS..SGNPVT.....L...QELWGPCPRI RR.....			
CLC0_TORPEDO	...ASGNPEAQSW..KAQEAM...LGVKTEVSRWRVAVKNC.....			
CLC3_HUMAN	..STHLLDL.LDEPIPGVG.....TYDDFH TIDWVREKCKDR.ERHR			
CLC4_HUMAN	..SGNLMDF.LDEPFDPVG.....TYEDFH TIDWVREKSRDT.DRHR			
CLC5_HUMAN	..SNRIMDF.LEEPIPGVG.....TYDDFN TIDWVREKSRDR.DRHR			
CLC6_HUMAN	CGERETRTPEEL.TILGETQEEDEILPRKDYESLDYDRCINDPYLEVLE			
CLC7_HUMAN	ELDDEL LDPDMDP HPPFKEIPHNEKLLSLKYE SLDYDNSENQLFLEER			

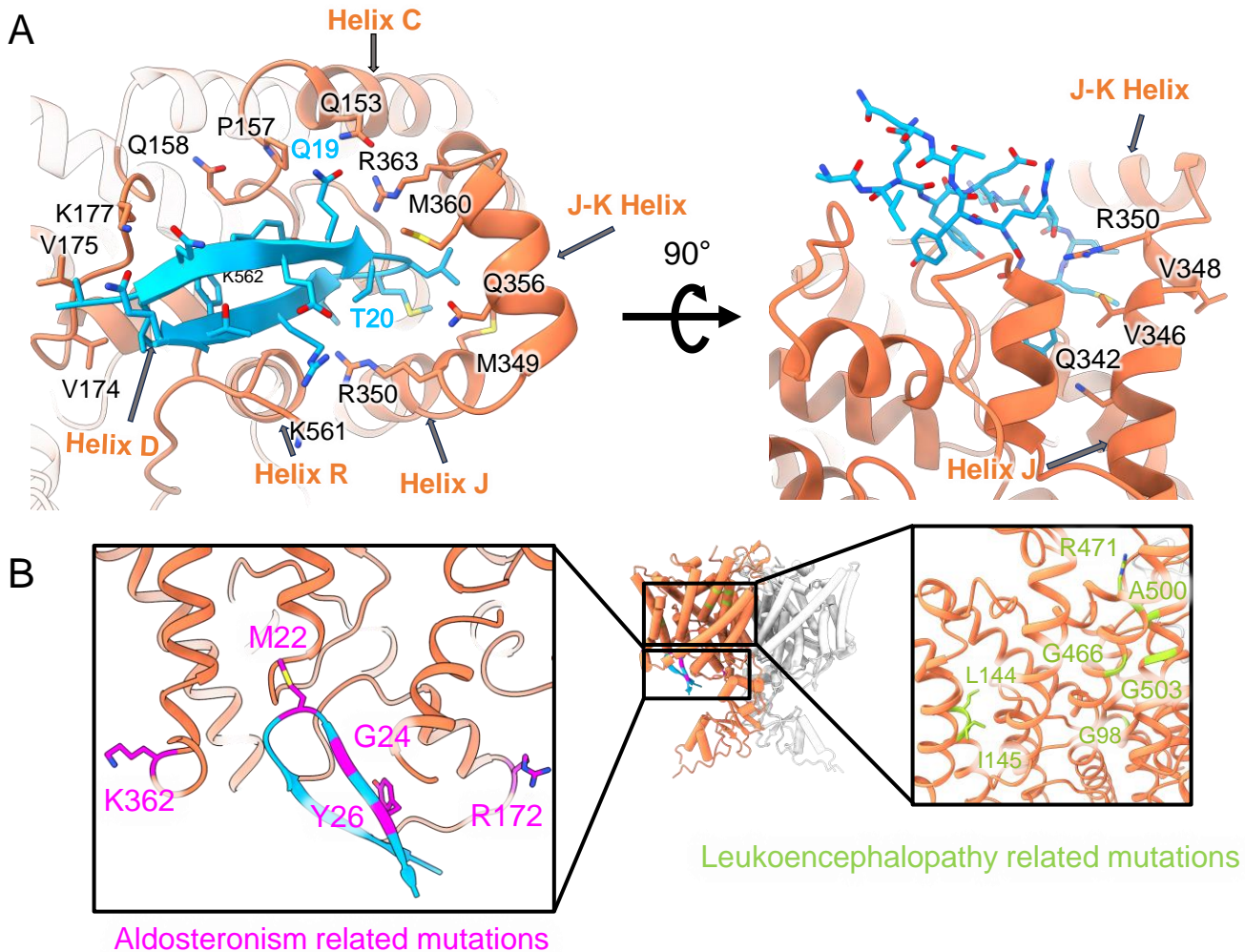
**Figure 5 supplement 1. N-terminal hairpin sequence is conserved in CLC-2, but not other CLCs. (A)** Alignment of the N-terminal hairpin sequence (blue boxed) amongst different species. **(B)** Alignment of N-terminal hairpin sequence (blue boxed) amongst other human CLCs.



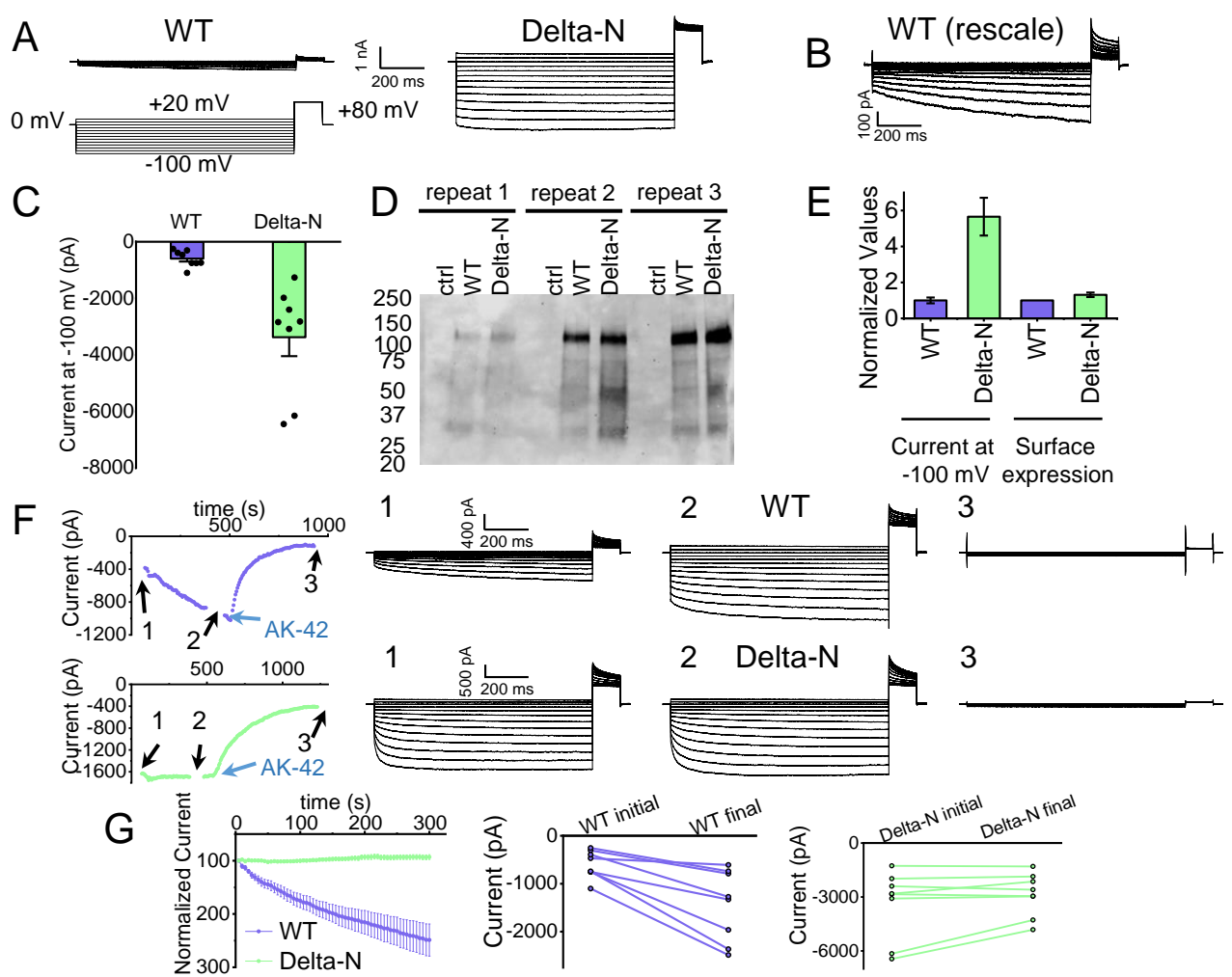
**Figure 5 - figure supplement 2. MD simulations confirm the N-terminal hairpin structure is stable (A)** In simulations, the N-terminus (blue) remains stably bound to the intracellular side of the transmembrane domain (orange). In the inset image, frames of the N-terminus taken every 200 ns from a representative simulation are overlaid. **(B)** The root-mean-square deviation (RMSD) and root-mean-square fluctuation (RMSF) of the N-terminus backbone were calculated after aligning frames on the transmembrane domains. Bars show the mean of five independent simulations, each 2.0  $\mu$ s in length. Error bars are 68% CI (confidence interval of the mean).

**A**90°  
**B**90°  


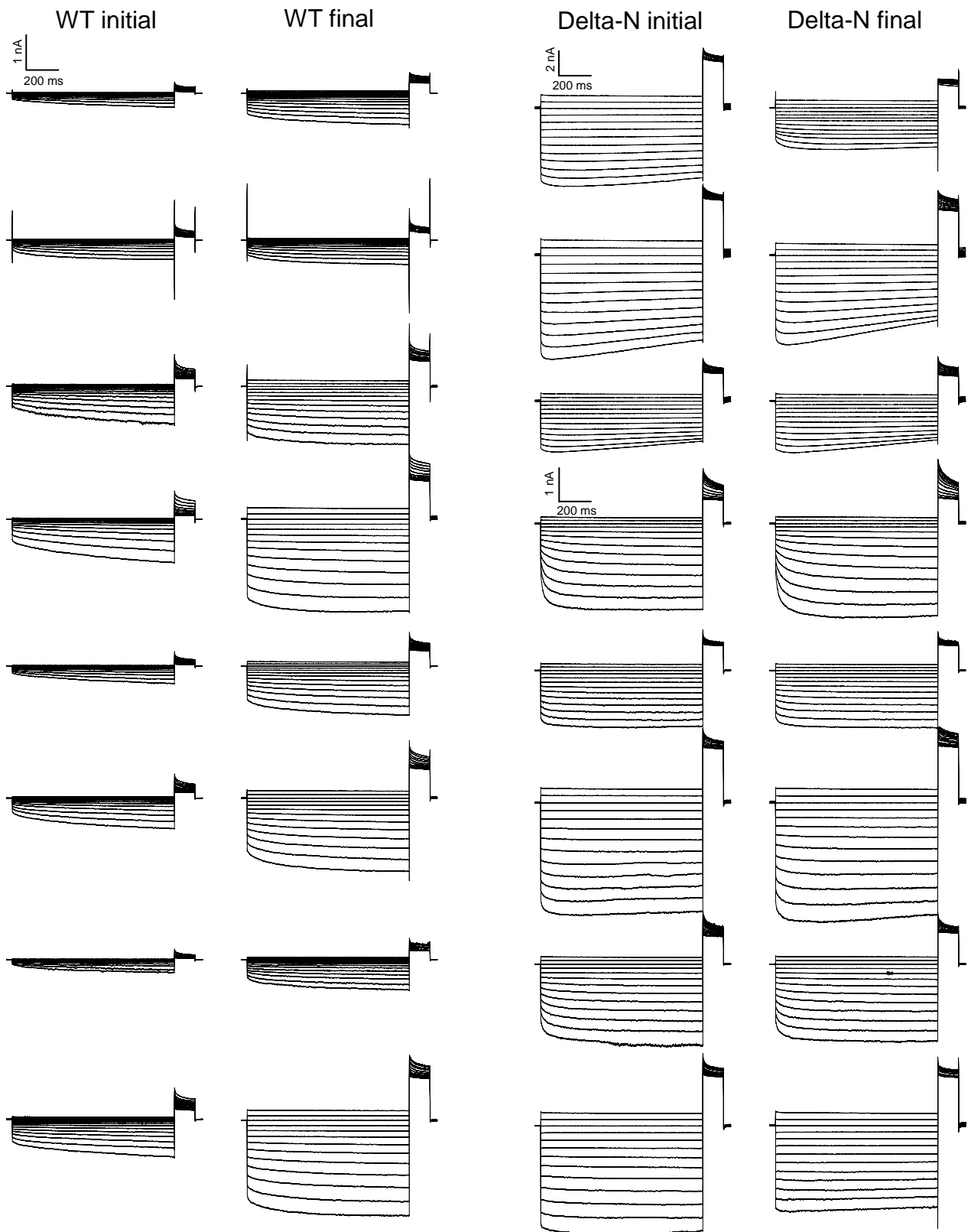
**Figure 5 - figure supplement 3.** The N-terminal hairpin blocks the primary Cl<sup>-</sup> pore in CLC-2. **(A)** *Left:* Side view of CLC2-TM showing the caver-detected pore (primary in orange and secondary in yellow). *Right:* View of the primary pore from the intracellular side. **(B)** The N-terminal hairpin (blue) overlaid with CLC2-TM as shown in panel **A**.



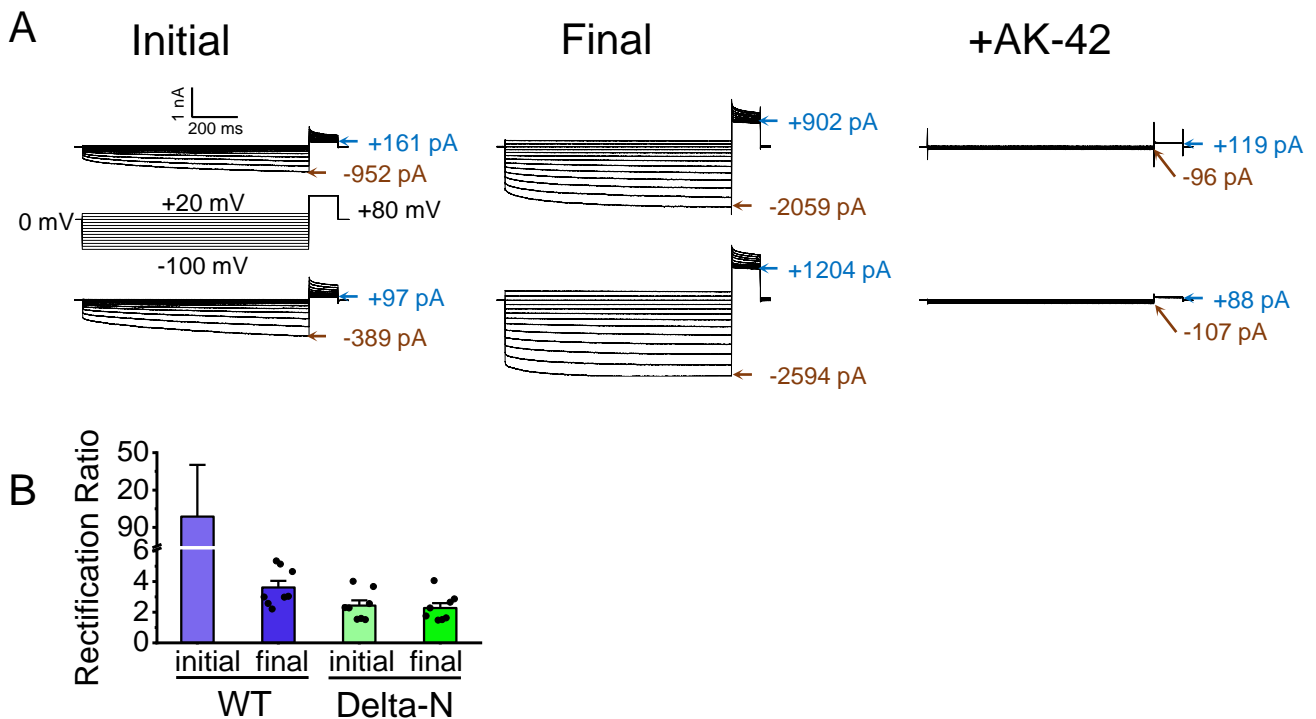
**Figure 5 – figure supplement 4. Mapping mutant data onto the cryoEM structure. (A)** Left: same as Figure 5C, showing hairpin interactions. Right: Rotated view highlighting ball “receptor” residues identified by Jordt and Jentsch, 1997. **(B)** Residues mutated in human Aldosteronism (Fernandes-Rosa et al., 2018, Scholl et al., 2018) and Leukoencephalopathy (Hector Gaitan-Penas., 2017) are shown on CLC2-CTDsym in magenta and green, respectively.



**Figure 6 Patch-clamp experiments support CLC-2 channel block by the N-terminal hairpin structure.** (A) Representative currents from WT and Delta-N CLC-2, recorded using the whole-cell patch clamp configuration in response to the voltage protocol shown. (B) WT CLC-2 recording from panel A, shown on an expanded scale. (C) Summary of current levels measured for WT and Delta-N CLC-2 at the end of the 1-s voltage pulse to -100 mV. Data are from six independent transfection samples, in each case with WT and Delta-N recorded on the same day following transfection. WT:  $-600 \pm 102$  pA (SEM, n=8); Delta-N:  $-3300 \pm 630$  pA (SEM, n=8). (D) Western blot detection of biotinylated surface-expressed CLC-2 from three independent experiments. (E) Summary data for electrophysiology and surface-biotinylation experiments. (F) Representative examples of experiments to evaluate current run-up in WT and Delta-N CLC-2. *Left panels:* Time course data. Following an initial voltage-family measurement (I-V protocol as in panel A, taken at point “1”), currents were monitored by 1-s pulses to -100 mV every 5 s for five minutes, after which a second voltage-family measurement was made (point 2), followed by application of AK-42 to facilitate leak subtraction, and a final voltage-family measurement at point 3. I-V traces are shown at right. (G) Summary data for “run-up” experiments. *Left panel:* Normalized time-dependent currents for WT and Delta-N. Currents were first leak-subtracted (using the steady-state current after AK-42 application) and then normalized to the amplitude of the current measured in the first step of the 5-minute sequence. *Right panels:* Leak-subtracted current levels at -100 mV from “initial” and “final” IV traces measured at points “1” and “2” in the time course (panel F). Average initial and final currents (pA  $\pm$  SEM, n=8) are WT:  $-600 \pm 102$  and  $-1400 \pm 260$ ; Delta-N:  $-3300 \pm 630$  and  $-2900 \pm 420$ .

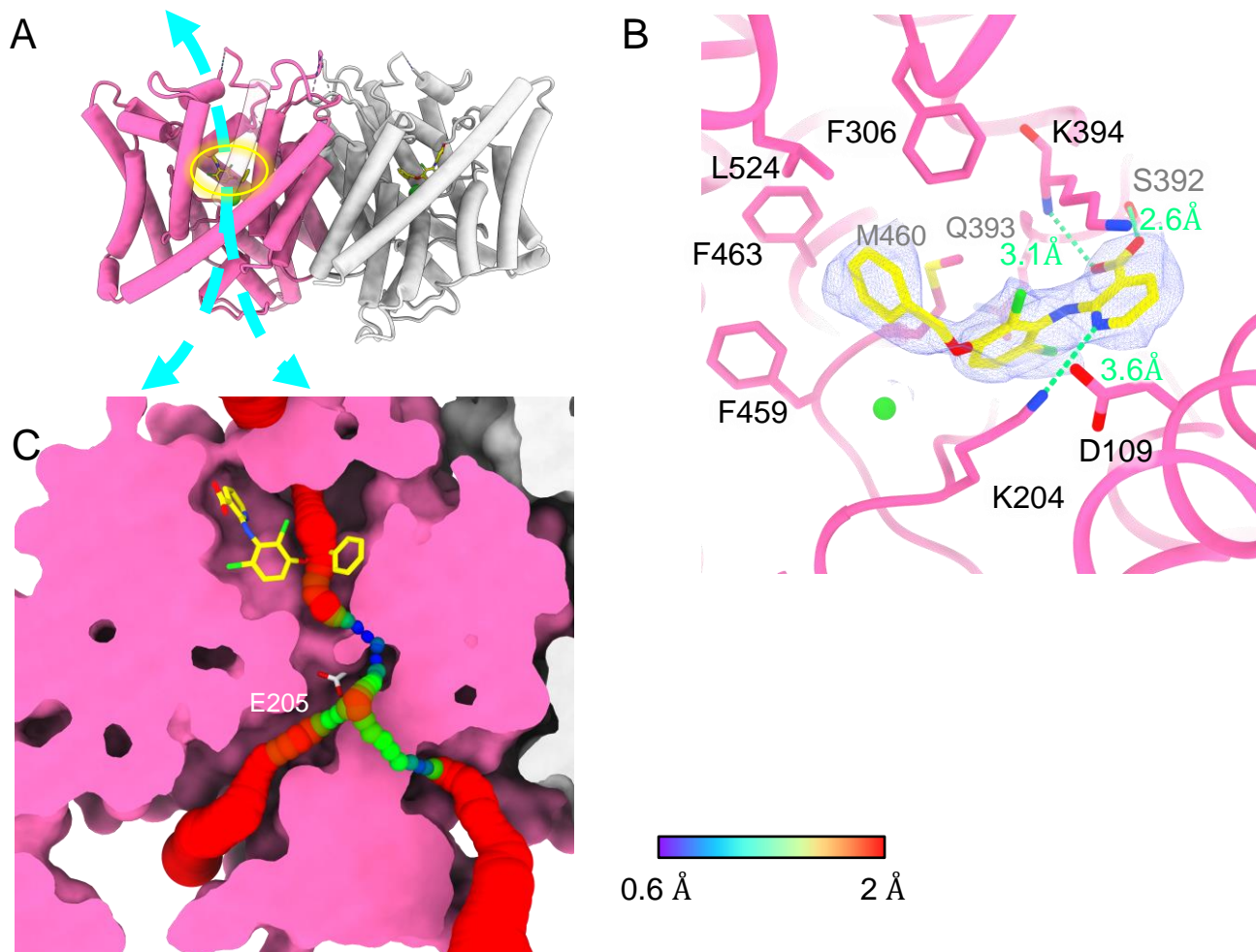


**Figure 6 – figure supplement 1.** Data traces from the CLC-2 run-up experiments summarized in Figure 6G. For Delta-N, separate scale bars indicate the <sup>55</sup>currents for the top six and bottom 10 traces. AK-42 leak currents, not subtracted in these raw data traces, are summarized in Figure 6 – source data 1.

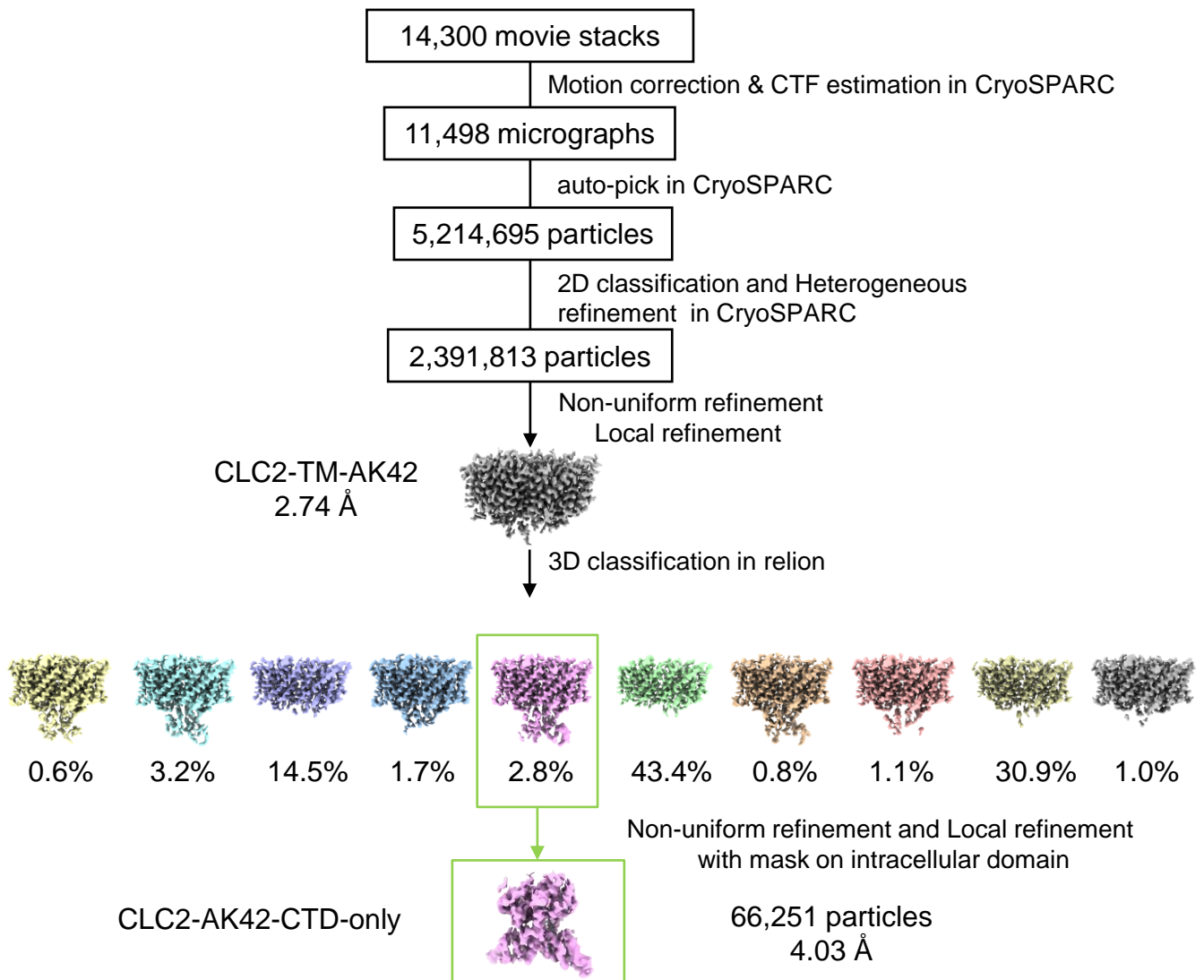


**Figure 6 – figure supplement 2. CLC-2 current rectification.** (A) Example traces from two experiments on WT CLC-2. Current values at end of the -100-mV test pulses and in the steady-state portion of the +80-mV tail pulse (following the +20-mV test pulse) are indicated. Robust AK-42 inhibition of the current at +80 mV indicates that CLC-2 is passing current at positive voltages. (B) Rectification ratios. Rectification was quantified by taking the ratio (absolute value) of the leak-subtracted currents at -100 mV and +80 mV. For WT initial currents, the low currents at +80 mV make this quantification challenging: for 5 out of 8 experiments on WT CLC-2, the AK-42 current at +80 mV was greater than the initial WT current at +80 mV, likely due to an increase in leak over the course of the experiment (~15 minutes of voltage pulsing). Therefore, the rectification calculated for the WT initial currents ( $99 \pm 34$ , SEM  $n=3$ ) has substantial uncertainty. That said, such high rectification is consistent with reports of CLC-2 rectification throughout the literature (Park et al., 1998; Arreola et al., 2002; Jentsch and Pusch, 2018). On the other hand, Delta-N currents display only mild rectification, which is straightforward to quantify given the high signal:noise (high AK-42-sensitive current relative to background), and which does not change in response to voltage pulsing. For “WT-final”, the rectification ratio similarly can be accurately quantified. Thus, while the high uncertainty and variance in estimating WT initial rectification precludes quantitative statistical comparisons, these data strongly suggest that WT CLC-2 current rectification decreases in parallel to current run-up. Data for all experiments are summarized in **Figure 6 – source data 1**.

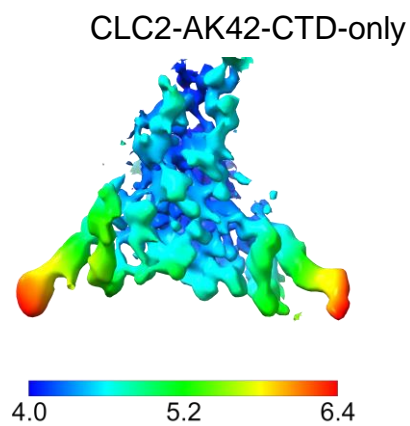
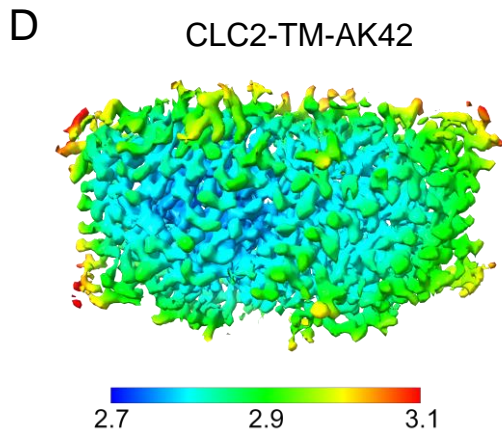
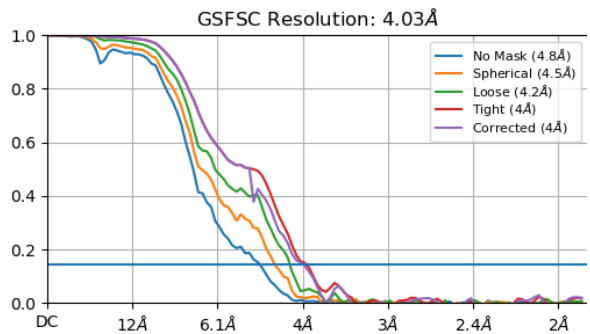
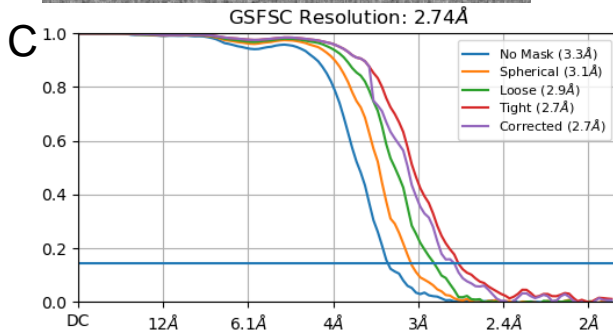
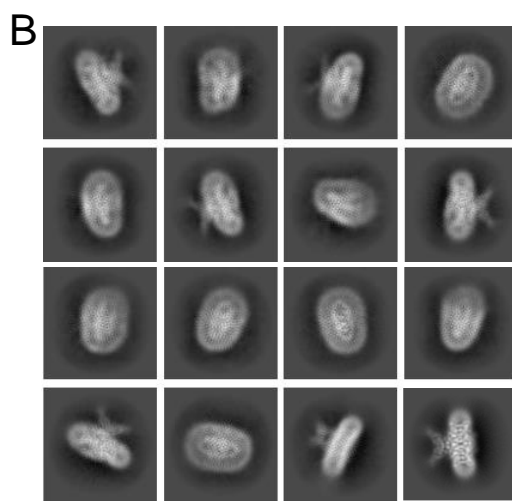
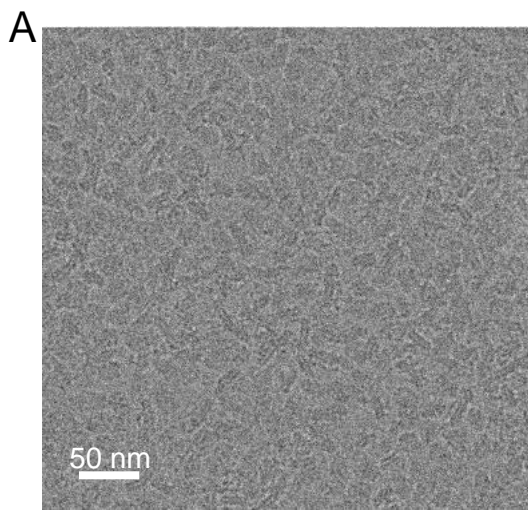




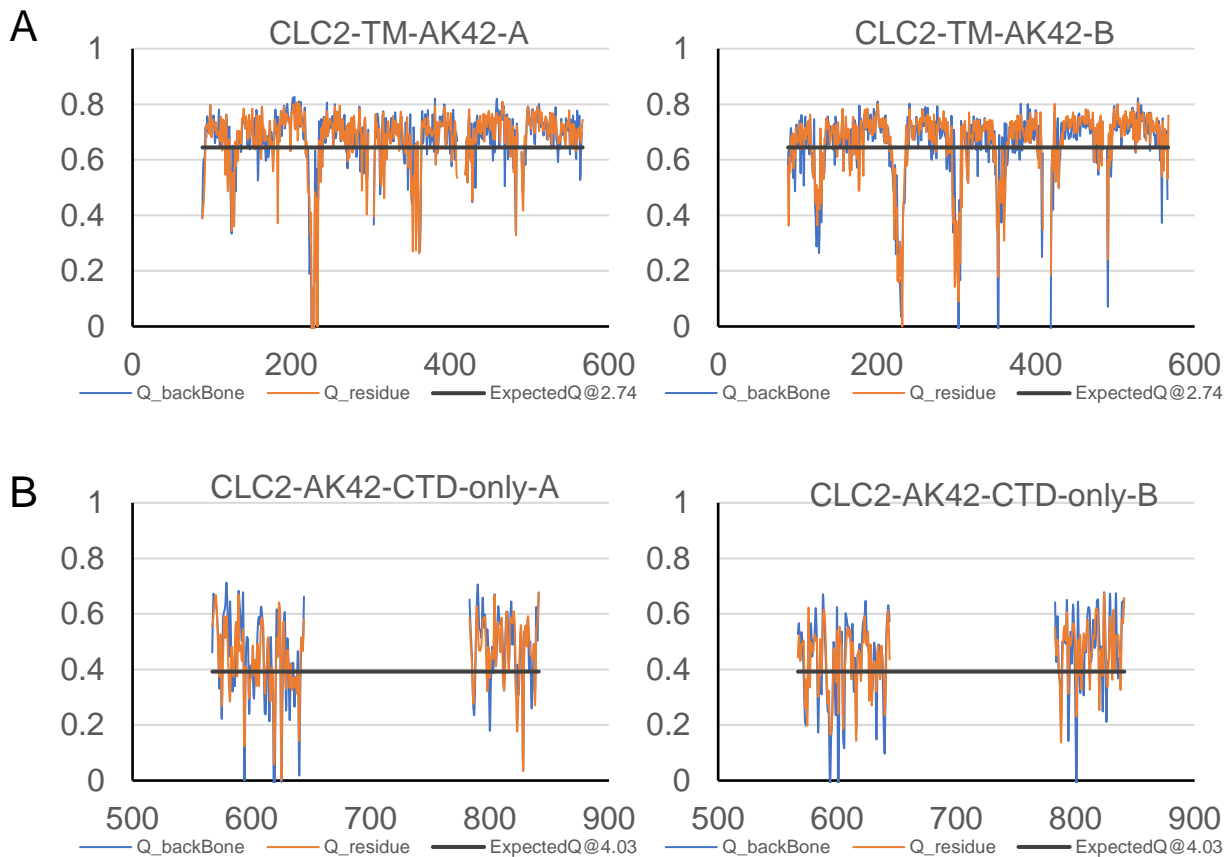
**Figure 7 Bound AK-42 blocks the Cl<sup>-</sup> pathway in CLC-2.** (A) TM-domain structure of the CLC-2 structure in complex with AK-42 (CLC2-TM-AK42) at 2.74 Å. The identical subunits of the homodimer are shown in hot pink and gray; Cl<sup>-</sup> ions are shown as green balls. Bound AK-42 is highlighted with a yellow circle on the pink subunit. The cyan arrow indicates the Cl<sup>-</sup> pathway. (B) Zoomed-in view of the AK-42 binding site. (C) A sliced view of CLC-2 showing AK-42 (yellow carbon atoms; CPK coloring on non-carbon atoms) and E<sub>gate</sub> (CPK sticks). Both AK-42 and E<sub>gate</sub> obstruct the Cl<sup>-</sup> pathway, displayed as a color map.



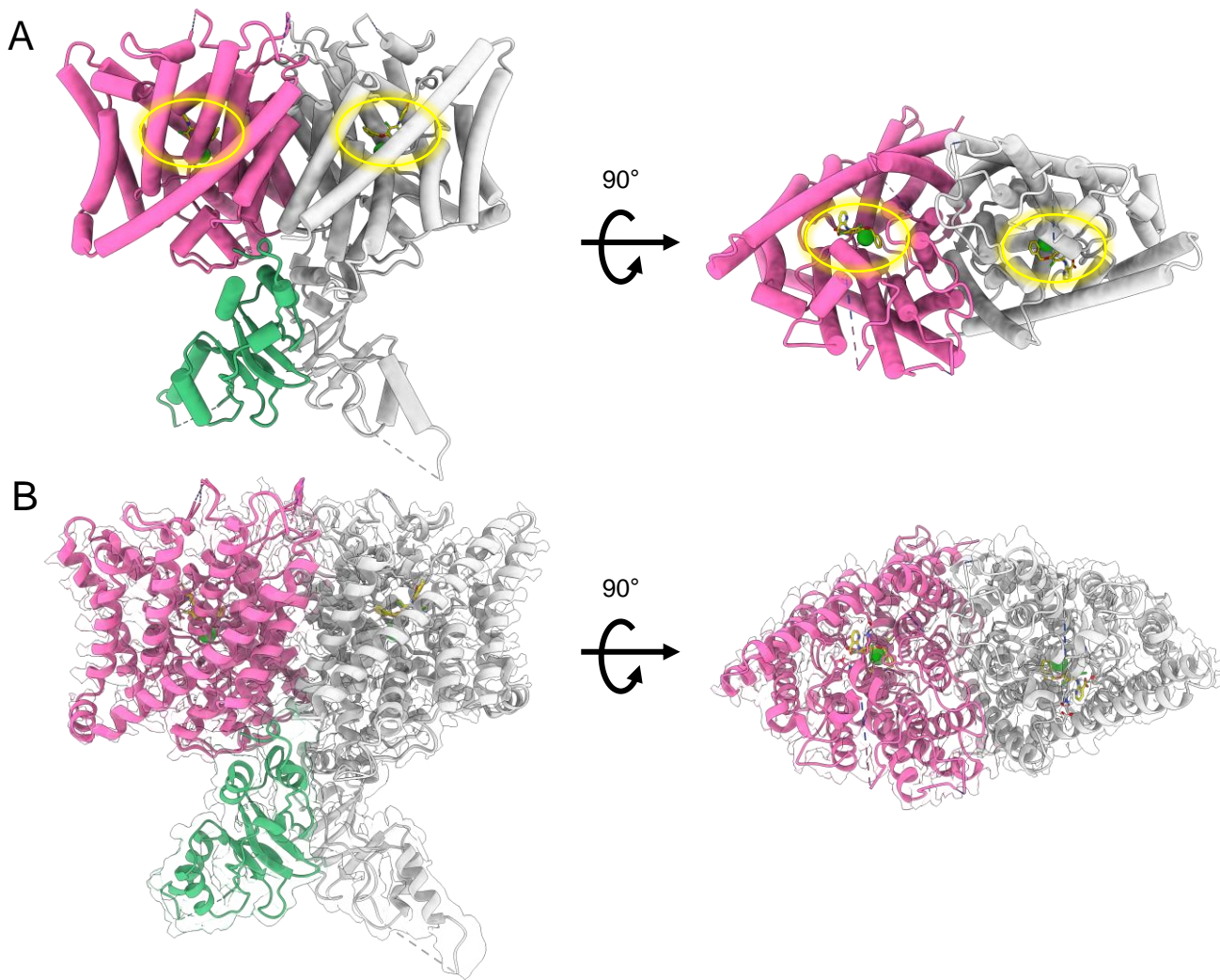
**Figure 7 - figure supplement 1. cryoEM workflow of the CLC2-TM-AK42 single-particle cryo-EM data processing.** A total of 14,300 movie stacks were collected on a 300 kV Titan Krios cryo-electron microscope. cryoSPARC was used for 2D classification and CLC2-TM-AK42 density map was obtained after 2D classification. Relion was used for 3D classification.



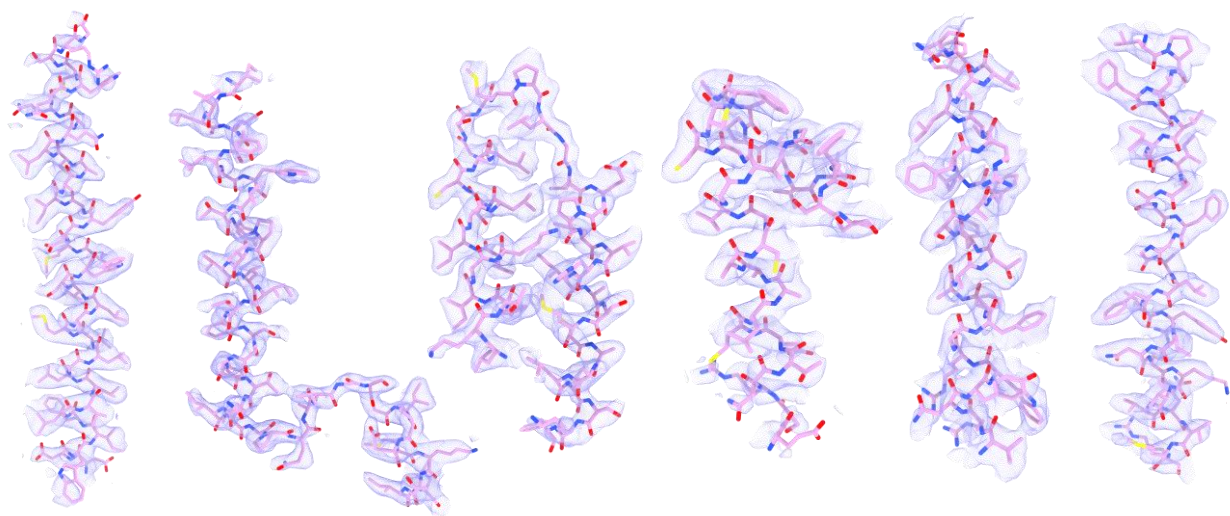
**Figure 7 - figure supplement 2.** Micrograph and 2D classes and structure validation of CLC2-AK42. (A) Representative motion-corrected cryo-EM micrograph. (B) 2D class averages. (C) Gold standard FSC plots calculated in cryoSPARC for CLC2-TM-AK42 (left) and CLC2-AK42-CTD-only (right). (D) Local resolution of the cryo-EM map for CLC2-TM-AK42 (left) and CLC2-AK42-CTD-only (right)



**Figure 7 - figure supplement 3. Model validation using Q-scores. (A)** Q-scores of CLC2-TM-AK42 for subunit A (left) and subunit B (right). **(B)** Q-scores of CLC2-AK42-CTD-only for subunit A (left) and subunit B (right). The black line represents the expected Q-score at respective resolution based on the correlation between Q-scores and map resolution.



**Figure 7 - figure supplement 4. cryoEM map and structure of CLC2-AK42. (A)** cryoEM model of CLC2-TM-AK42 with docked CTD. The transmembrane region is shown in hot pink and gray. The CTD is shown in green and gray. AK-42 is shown in yellow and highlighted by yellow circles. Chloride ions are shown in green. **(B)** cryoEM model overlay with density map of CLC2-AK42.



helix B

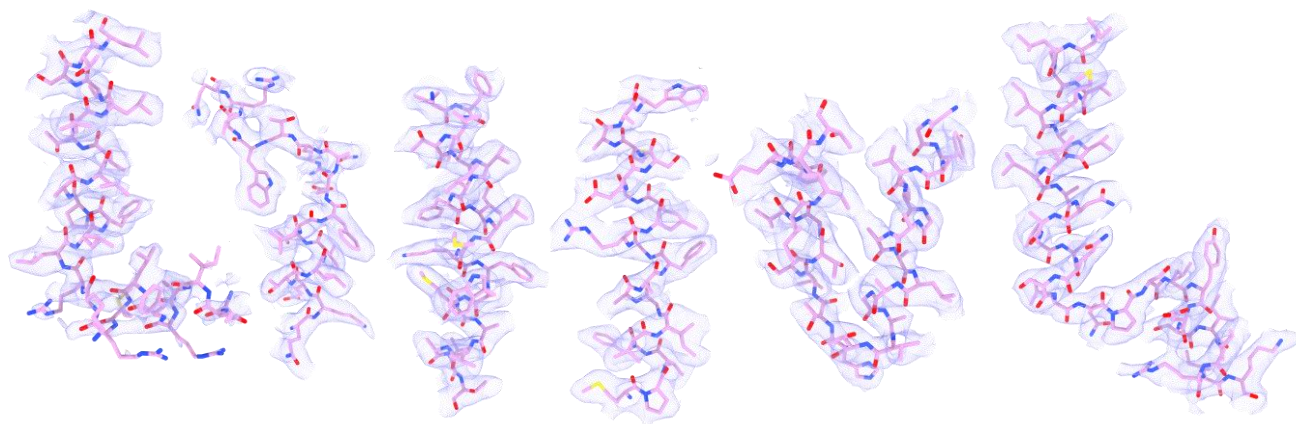
helix CD

helix EF

helix GH

helix I

helix J



helix K

helix L  
loop

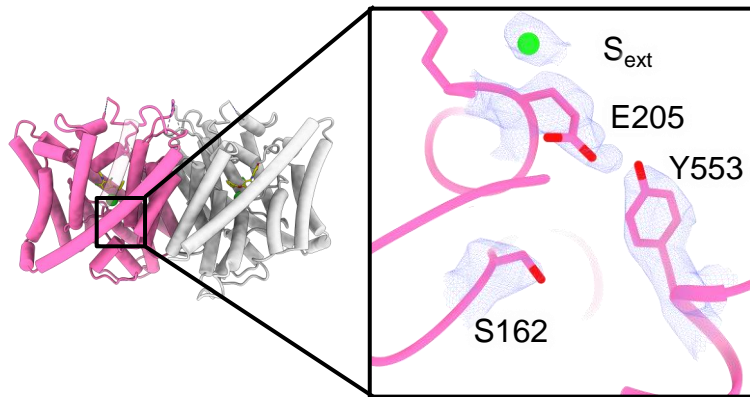
helix M

helix N

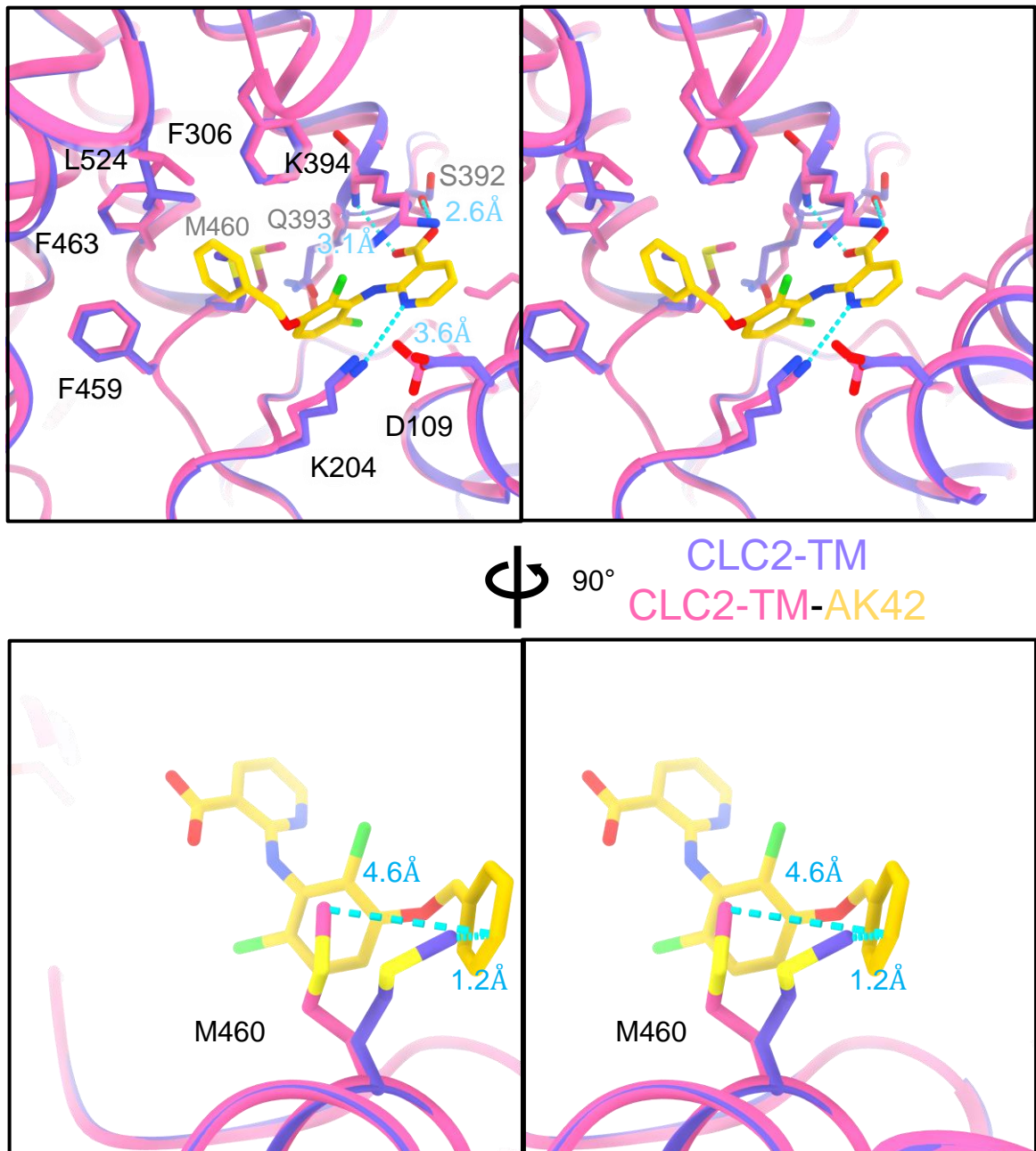
helix OP

helix QR

**Figure 7 - figure supplement 5. Helix map of CLC2-TM-AK42.** cryo-EM densities and model of CLC2-AK42 transmembrane helices.

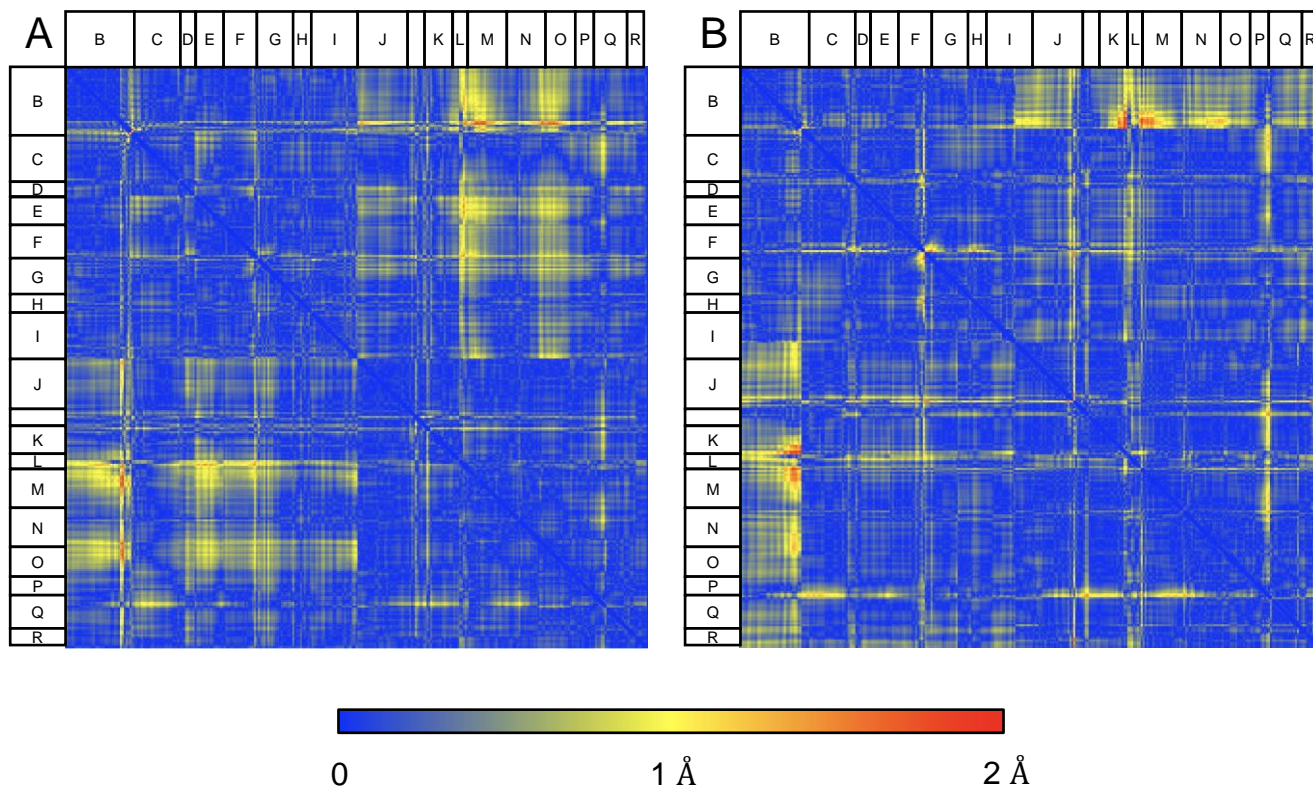


**Figure 7 – figure supplement 6. Density overlay at key Cl<sup>-</sup>-pathway residues.** Zoomed-in view highlighting residues S162, E205, Y553, and the bound chloride ion, with cryoEM density overlay.



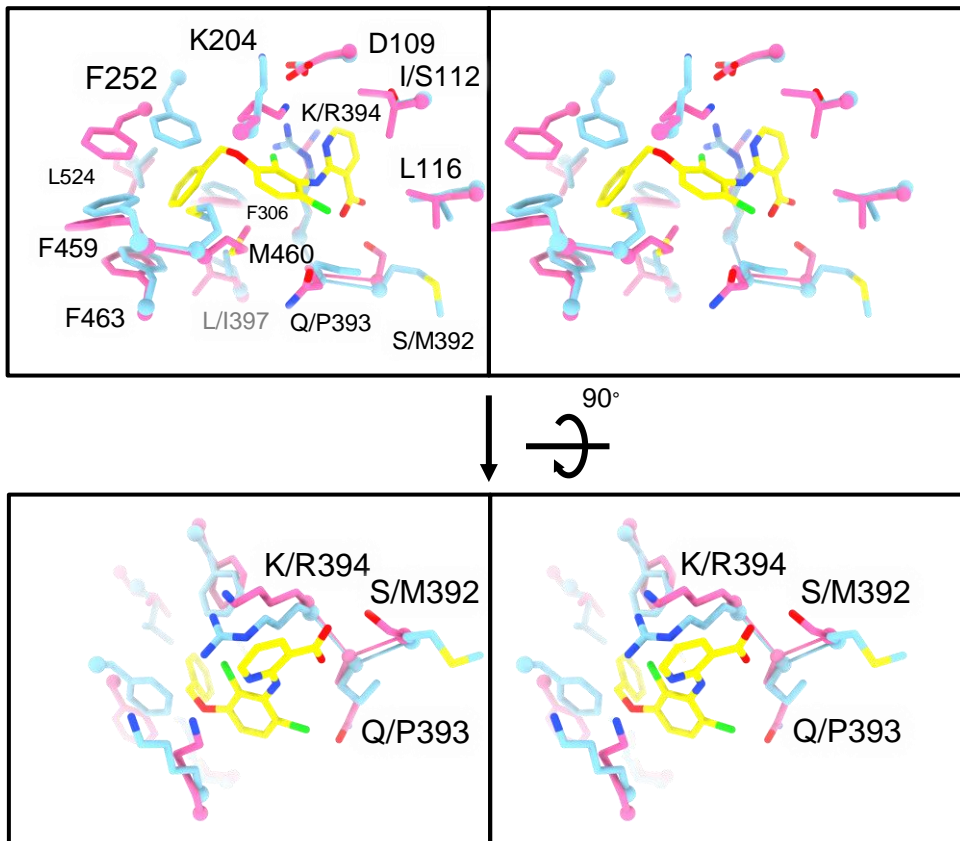
**Figure 7 - figure supplement 7. AK-42 binding site comparison between CLC2-TM and CLC2-TM-AK42.** Top: Stereo view of structural overlay at the AK-42 binding site. Hydrogen bonds between AK-42 and residues K204, S392, K394 are indicated by blue dashed lines. Bottom: A view highlighting the movement of residue M460 to make space for AK-42.



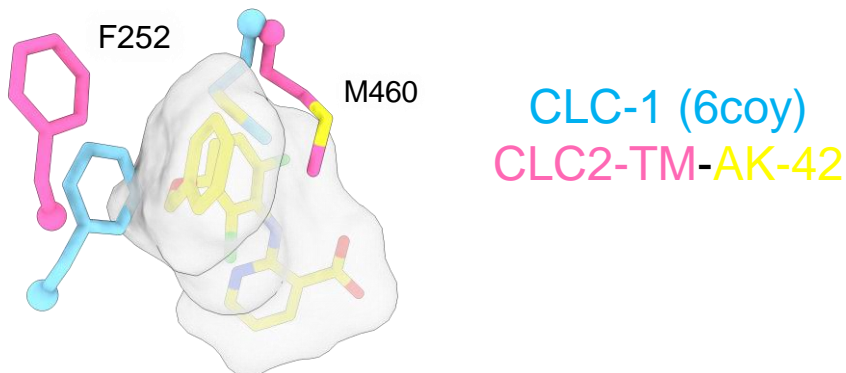


**Figure 7 - figure supplement 8. Structural comparison of CLC2-TM and CLC2-TM-AK42.** Difference distance matrices comparing Ca residues on TM helices between CLC2-TM and CLC2-TM-AK42 in subunits A (**A**) or B (**B**). Residues in loops connecting helices, where there is low confidence in the model building (Q score lower than the expected Q score of 0.65), were omitted from the matrices.

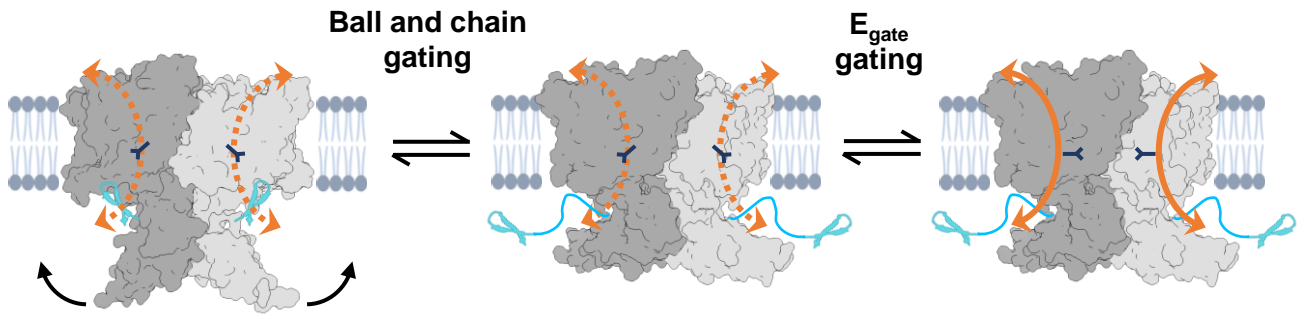
A



B



**Figure 7 - figure supplement 9 AK-42 binding site comparison between CLC-2 and CLC-1.** (A) Top: Stereo view of the AK-42 binding site in CLC2-TM-AK42 (hot pink) overlaid with the same region in CLC-1 (blue, PDB:6coy). Residue numbers correspond to those of CLC-2. The five residues that differ between CLC-2 and CLC-1 are: I112 (S139), S392 (M419), Q393 (P420), K394 (R421), and L397 (I424). Bottom: Rotated (stereo) view of AK-42 binding site to compare residues S392, Q393 and K394 in CLC-2 versus M419, P420 and R421 in CLC-1. These three were calculated to contribute most significantly to the AK-42 binding energy (Ma, 2023). (B) Residues in CLC-1 predicted to clash with AK-42. AK-42 is shown in yellow sticks and white surface. F252 and M460 in CLC-2 correspond to F279 and M485 in CLC-1.



**Figure 8. Structural framework for CLC-2 gating.** CLC-2's gating is illustrated based on our new structural data. Ball and chain gating is coupled to conformational change of the CTD, with CTD rotation precluding pore block by the N-terminal hairpin. Electrophysiological studies showing that removal of the CTD speeds CLC-2 activation and deactivation kinetics (Arreola et al., 2008; Garcia-Olivares et al., 2008) are consistent with this structural model. Localized  $E_{\text{gate}}$  motions control protopore gating within each subunit. Coupling between  $E_{\text{gate}}$  and the hairpin/CTD may underlie coupling between protopore and common gating observed in electrophysiological studies (Zuniga et al., 2004; de Santiago et al., 2005; De Jesus-Perez et al., 2021).